

IntechOpen

# Wind Turbine Icing

Recent Advances in Icing Characteristics  
and Protection Technology

*Edited by Yan Li*





---

Wind Turbine Icing  
- Recent Advances in  
Icing Characteristics and  
Protection Technology

*Edited by Yan Li*

Published in London, United Kingdom

---

Wind Turbine Icing - Recent Advances in Icing Characteristics and Protection Technology

<http://dx.doi.org/10.5772/intechopen.110924>

Edited by Yan Li

#### Contributors

Zhi Xu, Oluwagbenga Apata, Tadiwa Mavende, Lidong Zhang, Yimin, Xu, Yuze Zhao, Wenfeng Guo, He Shen, Jianlong Ma, Yingwei Zhang, Yuxin Xu, Yan Li

© The Editor(s) and the Author(s) 2023

The rights of the editor(s) and the author(s) have been asserted in accordance with the Copyright, Designs and Patents Act 1988. All rights to the book as a whole are reserved by INTECHOPEN LIMITED. The book as a whole (compilation) cannot be reproduced, distributed or used for commercial or non-commercial purposes without INTECHOPEN LIMITED's written permission. Enquiries concerning the use of the book should be directed to INTECHOPEN LIMITED rights and permissions department ([permissions@intechopen.com](mailto:permissions@intechopen.com)).

Violations are liable to prosecution under the governing Copyright Law.



Individual chapters of this publication are distributed under the terms of the Creative Commons Attribution 3.0 Unported License which permits commercial use, distribution and reproduction of the individual chapters, provided the original author(s) and source publication are appropriately acknowledged. If so indicated, certain images may not be included under the Creative Commons license. In such cases users will need to obtain permission from the license holder to reproduce the material. More details and guidelines concerning content reuse and adaptation can be found at <http://www.intechopen.com/copyright-policy.html>.

#### Notice

Statements and opinions expressed in the chapters are those of the individual contributors and not necessarily those of the editors or publisher. No responsibility is accepted for the accuracy of information contained in the published chapters. The publisher assumes no responsibility for any damage or injury to persons or property arising out of the use of any materials, instructions, methods or ideas contained in the book.

First published in London, United Kingdom, 2023 by IntechOpen

IntechOpen is the global imprint of INTECHOPEN LIMITED, registered in England and Wales, registration number: 11086078, 5 Princes Gate Court, London, SW7 2QJ, United Kingdom

British Library Cataloguing-in-Publication Data

A catalogue record for this book is available from the British Library

Additional hard and PDF copies can be obtained from [orders@intechopen.com](mailto:orders@intechopen.com)

Wind Turbine Icing - Recent Advances in Icing Characteristics and Protection Technology

Edited by Yan Li

p. cm.

Print ISBN 978-1-83769-014-5

Online ISBN 978-1-83769-015-2

eBook (PDF) ISBN 978-1-83769-016-9

# We are IntechOpen, the world's leading publisher of Open Access books Built by scientists, for scientists

6,700+

Open access books available

180,000+

International authors and editors

195M+

Downloads

156

Countries delivered to

Our authors are among the  
Top 1%

most cited scientists

12.2%

Contributors from top 500 universities



WEB OF SCIENCE™

Selection of our books indexed in the Book Citation Index  
in Web of Science™ Core Collection (BKCI)

Interested in publishing with us?  
Contact [book.department@intechopen.com](mailto:book.department@intechopen.com)

Numbers displayed above are based on latest data collected.  
For more information visit [www.intechopen.com](http://www.intechopen.com)





# Meet the editor



Dr. Yan Li is a professor at the Engineering College, Northeast Agricultural University, China. He has more than 15 years of experience in research and teaching. His main research fields include energy engineering, agricultural engineering, and mechanical engineering. He teaches courses in introduction to new energy, fluid dynamics, and wind energy engineering for both undergraduate and graduate students. His current research focuses on renewable energy, especially wind energy. He has more than fifty publications on wind turbines, wind turbine icing, and anti-icing technology to his credit. He is a member of the Chinese Aerodynamics Research Society, Chinese Society of Engineering Thermophysics, and Chinese Wind Energy Association.





# Contents

<b>Preface</b>	<b>XI</b>
<b>Chapter 1</b> Numerical Simulation of Icing Characteristics on a Blade Airfoil for Vertical-Axis Wind Turbine under Various Icing Conditions <i>by Zhi Xu</i>	<b>1</b>
<b>Chapter 2</b> An Overview of Power Loss Estimation in Wind Turbines Due to Icing <i>by Oluwagbenga Apata and Tadiwa Mavende</i>	<b>19</b>
<b>Chapter 3</b> A Review of Wind Turbine Icing Prediction Technology <i>by Lidong Zhang, Yimin Xu and Yuze Zhao</i>	<b>45</b>
<b>Chapter 4</b> Experimental Visualization of the Icing Process of Water Droplets on Cold Aluminum Plate Surface <i>by Yingwei Zhang, Yuxin Xu and Wenfeng Guo</i>	<b>63</b>
<b>Chapter 5</b> A Brief Review of Blade Surface Icing Adhesive Theories for Wind Turbines <i>by He Shen and Yan Li</i>	<b>79</b>
<b>Chapter 6</b> Experimental Study on the Ultrasonic De-Icing Method of Wind Turbine Blades <i>by Jianlong Ma, He Shen and Wenfeng Guo</i>	<b>93</b>



# Preface

In recent years, with the increasing attention paid to environmental and energy issues in the world, the development and utilization of clean and renewable energy have been greatly valued and developed. Among the potential renewable energy sources, wind energy has become one of the most widely commercialized. However, wind turbines installed in cold regions often experience icing on the surface of their blades. Blade icing can cause many serious impacts on wind turbines and has become an important issue to address. This book focuses on the recent research progress on wind turbine icing. It includes three research reports and three brief reviews.

Investigating the distribution characteristics of icing on the blade surface is the basis for studying wind turbine icing. Numerical simulation is one of the important methods for icing research. In this book, an icing model coupling water film flow with water film evaporation considering airfoil surface roughness is developed to investigate the effect of icing conditions on the icing distribution characteristics of a blade airfoil for vertical-axis wind turbines by numerical simulation. The calculated results are in good agreement with the experimental results. The findings obtained through numerical simulation contribute to the theoretical basis for exploring anti-icing and de-icing methods in wind turbines.

The most direct impact of icing on wind turbines is to reduce their power generation. Accurately predicting the power loss caused by icing conditions on wind turbines is very important. This book provides an overview of power loss estimation in wind turbines due to icing for establishing a foundation for deep research and investigations into the impact of icing on wind turbine power output. Various methodologies available for estimating power loss in wind turbines under icing conditions are collected and compared for analysis. Understanding the magnitude of power loss under icing conditions is crucial for optimizing wind turbine design, operation, and maintenance strategies.

The primary task in solving the problem of wind turbine icing is to accurately predict the occurrence of icing. Therefore, improving wind turbine ice prediction technology can assist wind farms in achieving more precise operation scheduling, avoiding needless shutdowns, and increasing power generation efficiency. This book reviews traditional wind turbine icing prediction methods. Specifically, it gives a detailed introduction to machine learning prediction methods. It provides a comprehensive description of the applicability and accuracy of various machine learning algorithms in wind turbine icing prediction and summarizes the applications and advantages.

The microscopic process of supercooled water droplets freezing on the blade surface is important for exploring the icing mechanism. This book examines the icing process of a single water droplet on a cold aluminum plate surface using a visualized method. The effects of volume and temperature on the icing characteristics are tested and acquired. The profile parameters of iced water droplets are processed and analyzed

via the program, including the contact diameter, maximum diameter and height of iced water droplets, contact angle, and more. These parameters can provide the experimental foundation to study the icing characteristics of wind turbine blades.

To research and develop efficient anti-icing and de-icing technologies, exploring the adhesive properties between the ice and the blade surface is necessary. This book summarizes the main theories of the icing adhesive mechanism, including mechanical theory, electronic theory, and wetting theory. It compares and analyzes the characteristics of several theories, discusses the impact of environmental factors on these theories, and makes suggestions for future research.

At present, there are several types of anti-icing and de-icing methods being developed, including electro-thermal, hot air, microwave, ultrasonic, pneumatic impulse, and other methods. This book introduces the theoretical and experimental studies on the ultrasonic de-icing of wind turbines. It analyzes and decides the de-icing vibration modes of the plate element and an airfoil blade for a wind turbine by simulation method. It tests the icing protection effects of ultrasonic vibration on the iced plate and blade segment. The results show that ultrasonic vibration could decrease the amount and adhesive strength of ice dramatically and have de-icing capability at the frequency of de-icing vibration mode.

Finally, it can be foreseen that with the continuous and rapid development of wind energy utilization and the frequent occurrence of extreme environments, the problem of icing on wind turbine blades will receive increasing attention. In addition, developing more economical and effective anti-icing and de-icing methods will become an important research direction.

**Yan Li**  
College of Engineering,  
Northeast Agricultural University,  
Harbin, China

# Numerical Simulation of Icing Characteristics on a Blade Airfoil for Vertical-Axis Wind Turbine under Various Icing Conditions

*Zhi Xu*

## Abstract

The phenomenon of icing on wind turbines gives rise to significant liability concerns in regions characterized by cold and humid climates, especially those with extreme climatic conditions. Accordingly, investigating the icing characteristics is essential for the safety operation of wind turbines. In this chapter, an icing model coupling water film flow with water film evaporation considering airfoil surface roughness is developed to investigate the effect of icing conditions on the icing characteristics of a blade airfoil for vertical-axis wind turbines by numerical simulation. The mechanism of heat and mass transfer under various icing conditions is explored. The results show that the simulated and experimental ice shapes on the airfoil agree well. The ice shape contour fluctuates along the airfoil surface at higher ambient temperature due to water film flow and heat flux variation. A large area of airfoil surface is covered by ice accretion at high wind speed due to an increase in driving force acting on water film and convective cooling between water film and air. The maximum ice thickness changes more significantly at wind speeds of 2–7 m/s than that at wind speeds of 7–12 m/s. This contributes to theoretical basis for exploring anti/de-icing method in wind turbines.

**Keywords:** wind turbine blade, icing condition, icing characteristics, numerical simulation, heat and mass transfer mechanism

## 1. Introduction

Wind energy is widely used in electricity generation due to huge reserve and cleanness [1, 2]. Owing to the fact that wind turbines are installed in humid and cold regions, ice may accumulate on the wind turbine blades. It causes liability issues such as aerodynamic performance degradation, increased noise, decreased lifetime, ice shedding, and safety risks [3, 4]. Therefore, investigating the icing characteristics on wind turbines is crucial to explore anti/de-icing methods.

In the last few decades, numerical simulation methods can provide the insight of flow and heat transfer physics in detail, which is not easily possible using icing wind tunnel [5]. Numerical simulation is therefore reliable-efficient ways to investigate the

icing characteristics of wind turbines under various icing conditions. For instance, Fu et al. [6] built the model to investigate the effect of angular speed on the icing characteristics at different locations of blades for a horizontal-axis wind turbine by numerical simulation. It was found that ice accumulation increased at the tip of blades with an increase in angular speed. Homola et al. [7] conducted numerical simulation to investigate the influences of ambient temperature and medium volume droplet diameter (MVD) on the icing characteristics. It was found that ice horns were observed at higher ambient temperature, and ice accretion increased with an increase in MVD. Etemaddar et al. [8] employed numerical approach to analyze the effect of ice accretion on the aerodynamic performance at various icing conditions. It was found that wind power loss increased by up to 35% when ice accumulated on the blades in below rated wind speed. Villalpando et al. [9] described the ice accretion shapes on different positions of a blade under icing conditions by numerical simulation. Yirtici et al. [10] employed numerical simulation to predict the influence of ice accretion on the power losses under various icing conditions. Jin and Virk [5] compared the ice accretion shapes on symmetric and asymmetric airfoils under icing conditions and reported that the ice accretion shapes were more streamlined on symmetrical airfoils as compared to asymmetric airfoils. Ibrahim et al. [11] evaluated the influence of blade thickness on the icing characteristics, and reported that the ice accretion thickness at the location of flow stagnation increased significantly with an increase in blade thickness due to higher droplet collection efficiency. Wang et al. [12] developed an improved multi-shot icing model to investigate the effect of ice accretion shapes on the aerodynamic performance on various positions of airfoils under yaw condition, and found that ice horn at 94% span position resulted in aerodynamic performance degradation due to flow separation. Manatbayev et al. [13] developed an icing model considering rotating effect to analyze the effect of ice accretion shapes on the aerodynamic performance for vertical axis wind turbines at various angles of attack and found that the glaze ice had a significant effect on aerodynamic performance degradation. Son et al. [14, 15] presented a more accurate method with moving reference frame and surface roughness effect to predict maximum ice accretion thickness and growth direction on different positions of airfoils. Baizhuma et al. [16] proposed an icing model coupling sliding mesh technique with multiple reference frame to analyze the effect of icing characteristics on the aerodynamic performance for rotating wind turbines under various icing conditions.

From the literature review, it is found that icing conditions including ambient temperature and wind speed have a great effect on the icing characteristics of wind turbine blades. Currently, there are some limitations in the above research as follows:

1. Most of researchers developed models to investigate the water film flow and icing process on clean airfoils under various icing conditions by numerical simulation. However, less attention has been paid to the effect of the water film flow and evaporation on the icing characteristics of rough airfoil surfaces.
2. The mechanism of the icing distribution on a rough airfoil of wind turbines is not clear.

Therefore, the main purposes of this study are as follows: (a) to propose the relationship between water evaporation and water film flow considering surface roughness effect; (b) to compare simulated and experimental ice shapes in order to validate the feasibility of numerical method; and (c) to investigate the heat and mass transfer mechanism of the ice accretion on a blade airfoil of wind turbines under different icing conditions.

## 2. Modeling

### 2.1 Mathematical model

#### 2.1.1 Airflow model

The external flow and heat transfer characteristics of wind turbine blades is investigated according to conservation of mass, momentum, and energy, which is expressed as follows [17]:

Continuity equation

$$\frac{\partial \rho_1}{\partial t} + \nabla \cdot (\rho_1 \vec{V}_1) = 0 \quad (1)$$

Momentum equation

$$\frac{\partial (\rho_1 \vec{V}_1)}{\partial t} + \nabla \cdot (\rho_1 \vec{V}_1 \vec{V}_1) = \nabla \cdot \sigma^{ij} + \rho_1 \vec{g} \quad (2)$$

$$\sigma^{ij} = -\delta^{ij} p_1 + \tau^{ij} \quad (3)$$

The Spalart-Allmaras model is employed at low Reynolds number to determine reliable wall shear force and heat transfer values for near-wall regions by numerical approach, which is expressed as follows [11, 18, 19]:

$$\frac{D\bar{v}}{Dt} = c_{b1}(1 - f_{t2})\bar{S}\bar{v} + \frac{1}{\sigma \text{Re}_\infty} \left\{ \nabla \cdot [(\bar{v} + \nu)\nabla\bar{v}] + c_{b2}(\nabla\bar{v})^2 \right\} - \frac{1}{\text{Re}_\infty} \left( c_w f_w - \frac{c_{b1}}{\kappa^2} f_{t2} \right) \left( \frac{\bar{v}}{d} \right)^2 + \text{Re}_\infty f_{t1} (\Delta V)^2 \quad (4)$$

$$\bar{S} = S + \frac{1}{\text{Re}_\infty} \frac{\bar{v}}{\kappa^2 d^2} f_{v2} \quad (5)$$

$$S = \sqrt{2\Omega_{ij}\Omega_{ij}} \quad (6)$$

$$\Omega_{ij} = \frac{1}{2} \left( \frac{\partial V_i}{\partial x_j} - \frac{\partial V_j}{\partial x_i} \right) \quad (7)$$

where  $c_{b1}$ ,  $c_{b2}$ ,  $c_w$ ,  $\kappa$ , and  $\sigma$  are the closure coefficients,  $f_w$  is the closure function, and  $f_{t1}$  and  $f_{t2}$  are tripping functions from laminar to turbulent flow.

Energy equation

$$\frac{\partial (\rho_1 E_1)}{\partial t} + \nabla \cdot (\rho_1 \vec{V}_1 H_1) = \nabla \cdot [k_1 (\nabla T_1) + V_i \tau^{ij}] + \rho_1 \vec{g} \cdot \vec{V}_1 \quad (8)$$

#### 2.1.2 Droplet flow model

The Eulerian two-fluid approach is employed to get droplet flow distribution on the blade airfoil for wind turbine according to continuity and momentum equations with droplet volume fraction, which is expressed as follows [20, 21]:

$$\frac{\partial \alpha}{\partial t} + \nabla \cdot (\alpha \vec{V}_2) = 0 \quad (9)$$

$$\frac{\partial (\alpha \vec{V}_2)}{\partial t} + \nabla \cdot (\alpha \vec{V}_2 \vec{V}_2) = \frac{C_D \text{Re}_2}{24K} \alpha (\vec{V}_1 - \vec{V}_2) + \alpha \left(1 - \frac{\rho_1}{\rho_2}\right) \frac{1}{\text{Fr}^2} \quad (10)$$

The drag coefficient is determined by Reynolds number, which is given by [22]:

$$C_D = \left(\frac{24}{\text{Re}_2}\right) (1 + 0.15 \text{Re}_2^{0.687}), \text{Re}_2 \leq 1300 \quad (11)$$

$$C_D = 0.4, \text{Re}_2 \geq 1300 \quad (12)$$

Meanwhile, droplet collection efficiency is given by [23]:

$$\beta = \frac{\alpha \vec{V}_2 \cdot \vec{n}}{V_\infty} \quad (13)$$

### 2.1.3 Water film and ice accretion model

The water film velocity is considered as the linear film velocity distribution normal to the wall where zero velocity is imposed, which is expressed as follows [18, 24]:

$$\vec{V}_f = \frac{y}{\mu_f} \vec{\tau}_{1,\text{wall}} \quad (14)$$

$$\tau_{1,\text{wall}} = C_f \frac{1}{2} \rho_1 V_\infty^2 \quad (15)$$

$$C_f = [3.476 - 0.707 \ln(k_s/s)]^{-2.46} \quad (16)$$

The mass conservation equation consists of the mass transfer caused by the incoming water droplets, water evaporation, and ice accretion, which is written by:

$$\rho_f \left[ \frac{\partial h_f}{\partial t} + \nabla \cdot (\vec{V}_f h_f) \right] = V_\infty \beta LWC - \dot{m}_{\text{evap}} - \dot{m}_{\text{ice}} \quad (17)$$

The energy conservation equation consists of the heat transfer caused by the incoming water droplets, phase change, ice accretion, convective, and radiative heat fluxes, which is calculated by:

$$\rho_f \left[ \frac{\partial h_f c_f \tilde{T}}{\partial t} + \nabla \cdot (\vec{V}_f h_f c_f \tilde{T}) \right] = \left( c_f \tilde{T}_{2,\infty} + \frac{1}{2} \vec{V}_2^2 \right) V_\infty LWC \beta - 0.5 \dot{m}_{\text{evap}} (L_{\text{evap}} + L_{\text{subl}}) + \dot{m}_{\text{ice}} (L_{\text{fus}} - c_{\text{ice}} \tilde{T}) + \sigma \varepsilon (T_\infty^4 - T_f^4) + \dot{Q}_h \quad (18)$$

The mass of water evaporation is given by:

$$\dot{m}_{\text{evap}} = h_m (\rho_s - \rho_\infty) = h_m \left( \frac{P_s}{RT_s} - \frac{P_\infty}{RT_\infty} \right) \quad (19)$$



Eq. (19) is substituted into Eq. (18), which is obtained as follows:

$$\begin{aligned} \rho_f \left[ \frac{\partial h_f c_f \tilde{T}}{\partial t} + \nabla \cdot (\vec{V}_f h_f c_f \tilde{T}) \right] &= \left( c_f \tilde{T}_{2,\infty} + \frac{1}{2} \vec{V}_2^2 \right) V_\infty LWC \beta \\ -0.5 h_m \left( \frac{P_s}{RT_s} - \frac{P_\infty}{RT_\infty} \right) (L_{\text{evap}} + L_{\text{subl}}) &+ \dot{m}_{\text{ice}} (L_{\text{fus}} - c_{\text{ice}} \tilde{T}) + \sigma \varepsilon (T_\infty^4 - T_f^4) + \dot{Q}_h \end{aligned} \quad (20)$$

The mass of water evaporation caused by water film flow considering roughness effect is written by:

$$\begin{aligned} \rho_f \left[ \frac{\partial h_f c_f \tilde{T}}{\partial t} + \nabla \cdot (\vec{V}_f h_f c_f \tilde{T}) \right] &= \left( c_f \tilde{T}_{2,\infty} + \frac{1}{2} \vec{V}_2^2 \right) V_\infty LWC \beta \\ -0.5 \text{St} V_f L_e^{-2/3} \left( \frac{P_s}{RT_s} - \frac{P_\infty}{RT_\infty} \right) &(L_{\text{evap}} + L_{\text{subl}}) + \dot{m}_{\text{ice}} (L_{\text{fus}} - c_{\text{ice}} \tilde{T}) + \sigma \varepsilon (T_\infty^4 - T_f^4) + \dot{Q}_h \end{aligned} \quad (21)$$

Stanton number is different for laminar and turbulent regimes according to empirical relationship [25], which is expressed as follows:

$$\text{St} = \begin{cases} 0.5 C_f \text{Pr}_t^{-2/3} \\ 0.5 C_f / (\text{Pr}_t + \sqrt{0.5 C_f} \text{St}_k^{-1}) \end{cases} \quad (22)$$

A series of functional equations are added to close the above equations due to unknown variables such as the water film thickness, the interface equilibrium temperature, and the ice accretion mass, which are expressed as follows:

$$\begin{cases} h_f \geq 0 \\ \dot{m}_{\text{ice}} \geq 0 \\ h_f \tilde{T} \geq 0 \\ \dot{m}_{\text{ice}} \tilde{T} \leq 0 \end{cases} \quad (23)$$

#### 2.1.4 Roughness model

Roughness model is expressed as follows [26]:

$$\left[ \frac{(k_s/c)}{(k_s/c)_{\text{base}}} \right]_{V_\infty} = 0.4286 + 0.0044139 V_\infty \quad (24)$$

$$\left[ \frac{(k_s/c)}{(k_s/c)_{\text{base}}} \right]_{LWC} = 0.5714 + 0.2457(LWC) + 1.2571(LWC)^2 \quad (25)$$

$$\left[ \frac{(k_s/c)}{(k_s/c)_{\text{base}}} \right]_{T_s} = 0.047 T_s - 11.27 \quad (26)$$

$$(k_s/c)_{\text{base}} = 0.001177 \quad (27)$$

The value of sand-grain roughness is calculated by:

$$k_s = \left[ \frac{(k_s/c)}{(k_s/c)_{base}} \right]_{V_\infty} \left[ \frac{(k_s/c)}{(k_s/c)_{base}} \right]_{LWC} \left[ \frac{(k_s/c)}{(k_s/c)_{base}} \right]_{T_s} (k_s/c)_{base}^c \quad (28)$$

## 2.2 Geometry and computational mesh

The chord length and span length of the blade airfoil are 0.5334 and 0.1 m, respectively. The computational domain was meshed by structured elements, as shown in **Figure 1**. The near-wall refinement method with inflation factor (1.1) was employed to generate the nonuniform grids on the blade airfoil. The mesh cells of 41,130 were used to guarantee high computational precision and improve computational efficiency due to less than 0.5% relative error between 41,130 and 89,356 mesh cells in numerical approach.

In-cloud measurements indicate that the liquid water content (LWC) changes from 0 to 5 g/m<sup>3</sup> [27, 28]. The actual droplet size distribution in-cloud is represented by a single variable called the median volume diameter (MVD), which varies from 10 μm (in freezing fog) to 5000 μm (in freezing rain) [28]. In addition, the ambient temperature and wind speed have a great effect on the icing characteristics of wind turbine blades. According to the book reported by Battisti [28], under operating conditions of wind turbines, the ambient temperature changes in the range of 233–323 K, and wind speed varies in the range of 2–25 m/s. In this study, the icing conditions were selected as follows: liquid water content (LWC) of 0.6 g/m<sup>3</sup> with medium volume diameter (MVD) of 50 μm, ambient temperatures of 263–268 K, and wind speeds of 2–12 m/s. An angle of attack was 12°, and icing time was 30 min. The ice conditions were illustrated in **Table 1**.

## 2.3 Boundary condition and solution method

The far-field and wall boundary conditions were employed in external flow field and solid surface of a blade airfoil for wind turbines in numerical simulation, respectively. The coupled boundary condition was used to deal with fluid-solid interface. The detailed parameters were displayed in **Table 2**.

Numerical approach was employed to investigate the icing characteristics on a blade airfoil of wind turbines under various icing conditions by FNESAP-ICE. Spatial discretization was performed by finite element method with a streamline upwind term. The matrix equations linearized by the Newton approach was iteratively solved using the implicit Gear scheme and a generalized minimum residual procedure. The time-marching scheme is explicit, and the automatic time step was employed to obtain the optimal time step for each grid/film speed combination, resulting in considerable computational cost savings. The ALE (Arbitrary Lagrangian Eulerian) formulation was used for the mesh displacement due to ice accretion in time or body motion.

## 2.4 Model validation

Numerical method is validated in terms of ice shapes on a NACA 0012 airfoil in the NASA Icing Wind Tunnel [29]. The ice conditions were as follows: angle of attack of 4°, wind speed of 12 m/s, liquid water content (LWC) of 0.55 g/m<sup>3</sup> with medium volume droplet diameter (MVD) of 20 μm, ambient temperatures of 267 K and 247 K, and icing time of 420 s.

It is found that the simulated and experimental ice shapes on the airfoil agree well at ambient temperatures of 267 and 247 K, as shown in **Figure 2**. Ice horns are observed at the leading edge at ambient temperature of 267 K, as displayed in **Figure 2a**. The impinging water will immediately freeze into ice at the leading edge due to high droplet collection efficiency. On the other hand, the impinging water will partly form unfrozen water film due to the fact that the latent heat is not removed at relatively high ambient

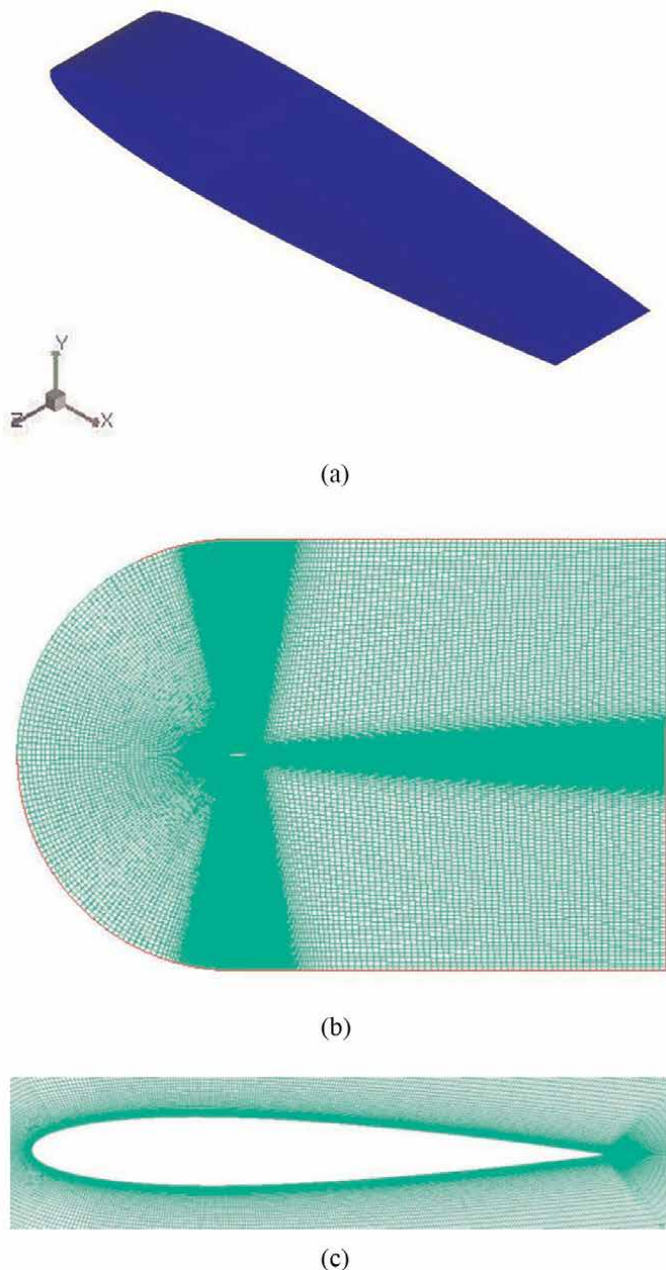


**Figure 1.**  
*Geometry and computational mesh of NACA0012 blade airfoil.*

Parameters	Value
Wind speed (m/s)	2–12
Ambient temperature (K)	263–268
Liquid water content (g/m <sup>3</sup> )	0.6
Medium volume droplet diameter (μm)	50

**Table 1.**  
*The ice conditions.*

Type	Values
Far-field	Pressure: 101325 Pa Temperature: 263–268 K Speed: 2–12 m/s LWC: 0.6 g/m <sup>3</sup>
Wall	No slip, coupled condition

**Table 2.**  
*Boundary conditions.*

temperature. The runback water flows along the surface of blade airfoil where convective cooling rate is high, freezing to form ice horns. It is found that the rime ice appears at the leading edge when the ambient temperature is 247 K, as illustrated in **Figure 2b**. Compared with the glaze ice, ice horns are not observed at the leading edge under rime ice condition. This is attributed to the fact that all water droplets impinging at the leading edge will immediately freeze into ice instead of water film formation at relatively low ambient temperature, and ice accretion grows gradually in the direction of the impinging water droplets, forming smooth and streamlined ice shape.

### 3. Results and discussion

#### 3.1 The effect of ambient temperature on icing characteristics

To investigate the influence of ambient temperature variation on ice accretion shape and rate, numerical analyses were performed at different ambient temperatures of 263–268 K. **Figure 3** illustrates the ice shapes on the blade airfoil at different ambient temperatures for wind speed of 7 m/s. The collision efficiency is not affected by the ambient temperature variation, but the rate and shape of ice accretion change with the change in ambient temperature due to surface heat flux variation. At lower ambient temperature, the rate of ice accretion grows rapidly and the ice shape is smooth due to higher droplet freezing fraction. In contrast, at higher ambient temperature, most of droplets do not freeze into ice due to the fact that the latent heat released by solidification is not removed by air, forming unfrozen water film to flow along the airfoil surface caused by airflow effect. Therefore, the growth rate of ice accretion becomes slow, and the ice shape is not smooth at higher ambient temperature as compared to lower ambient temperature.

**Figure 4** shows the ice accretion thickness distribution on the blade airfoil at different ambient temperatures. With the ambient temperature decreasing from 268 to 263 K, it is observed that the maximum ice accretion thickness increases from 4.55

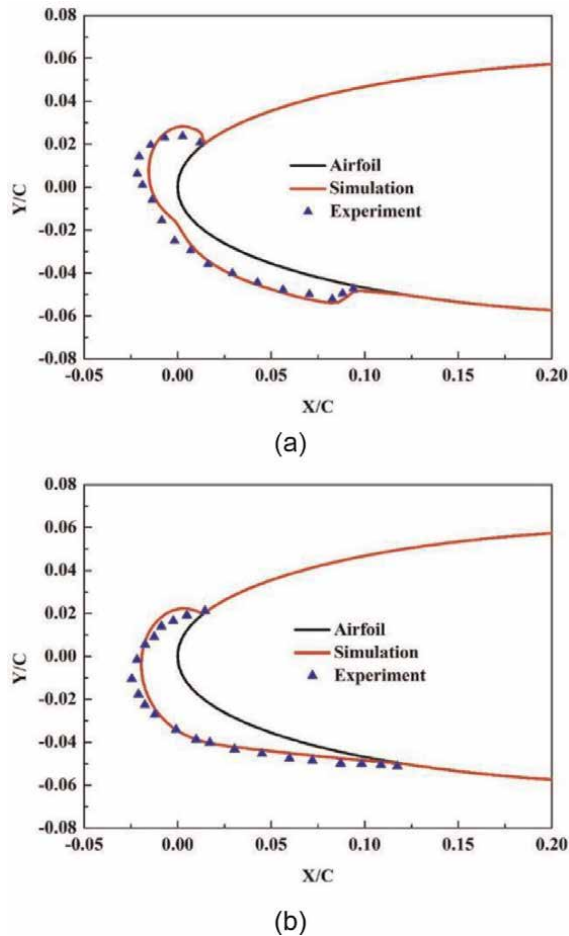
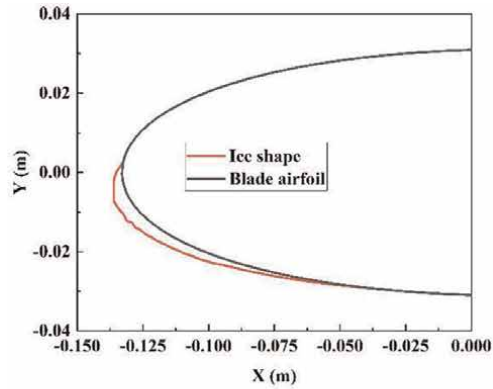


**Figure 2.** The simulated and experimental ice shapes on the airfoil (a) Ambient temperature of 267 K and (b) ambient temperature of 247 K.

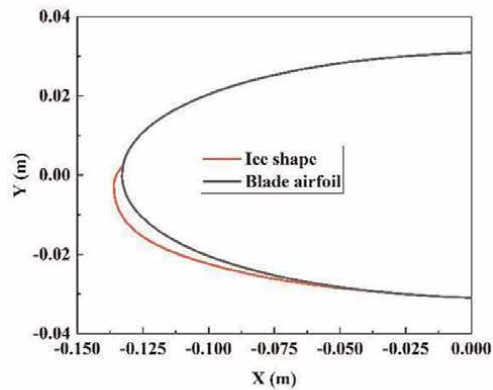
to 4.73 mm. This is mainly due to the fact that the droplet freezing fraction increases with the ambient temperature decreasing. The growth rate of ice accretion becomes faster at ambient temperature of 263 K than that at ambient temperature of 268 K. This is explained by the fact that most latent heat released by solidification is removed by air at lower ambient temperature. In addition, the ice accretion thickness fluctuates along the airfoil surface at higher ambient temperature due to water film flow and heat flux variation. In a word, the discrepancy in icing characteristics caused by various ambient temperatures can be explained by the insight of coupling water film flow with heat transfer in detail.

### 3.2 The effect of wind speed on icing characteristics

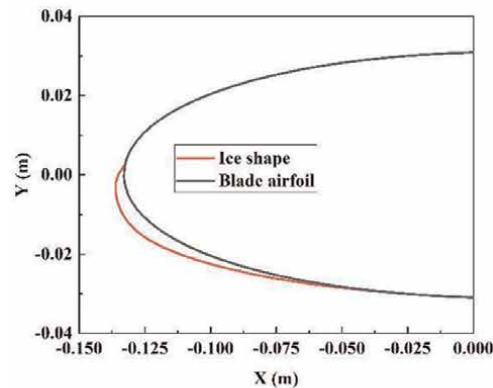
Figure 5 shows the effect of wind speed on the ice shapes at ambient temperature of 263 K. It is found that the maximum ice accretion thickness is observed at the leading edge. This is due to the fact that the largest amount of impinging water can be collected at the leading edge, freezing to form the thickest ice layer at ambient



(a)



(b)



(c)

**Figure 3.** The effect of ambient temperature on ice shapes (a) 268 K, (b) 265 K, and (c) 263 K.

temperature of 263 K. With the wind speed gradually increasing, the ice accretion at the leading edge grows along the direction, which is normal to the blade surface or tangential to trajectory of the blade airfoil. This can be attributed to the fact that the amount of the impinging water increases as the wind speed increases, forming thicker

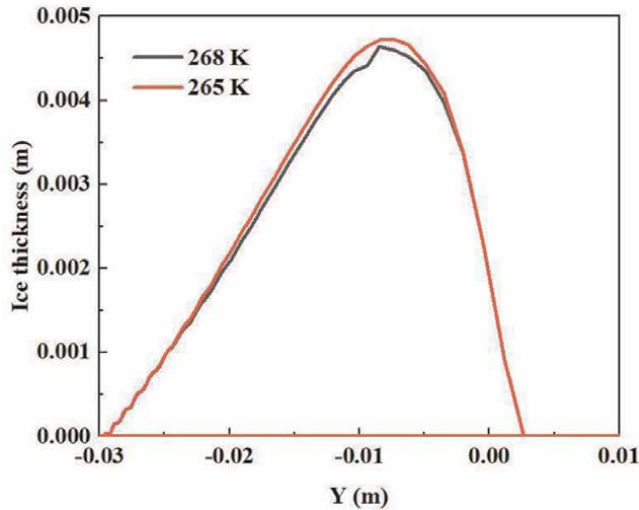


**Figure 4.**  
*The effect of ambient temperature on ice thickness.*

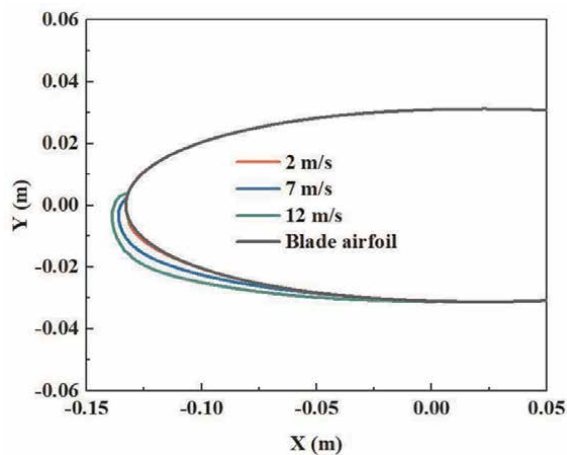


**Figure 5.**  
*The effect of wind speed on ice shapes at 263 K.*

ice layer due to convective heat transfer enhancement caused by higher wind speed. In addition, a wider ice shape contour covered on the blade airfoil is observed at higher wind speed. The impinging water partly forms unfrozen water film due to the fact that the latent heat released by solidification cannot be immediately removed by air. Thus, the unfrozen water film driven by airflow moves toward the further downstream where the convective cooling rate enhances due to higher wind speed, resulting in freezing into ice layer.

**Figure 6** shows the ice accretion thickness on the blade airfoil for different wind speeds at ambient temperature of 263 K. It is found that ice accretion distribution is wider at wind speed of 12 m/s than that at wind speed of 2 m/s. When the wind speed increases in the range of 2–12 m/s with steps of 5 m/s, the maximum ice accretion thickness varies from 0.783 to 8.16 mm. This is explained by the fact that more

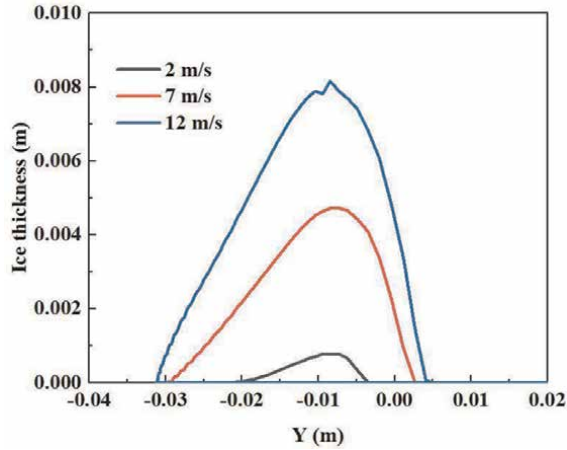


**Figure 6.**  
The effect of wind speed on ice thickness at 263 K.

impinging water droplets accumulate at the leading edge with an increase in wind speed, resulting in forming thicker ice accretion caused by solidification. Meanwhile, unfrozen water film flows along the surface of blade airfoil due to shear force of air. Owing to the fact that the driving force acting on water film is proportional to wind speed, a wider water film distribution on the surface of blade airfoil is obvious at higher wind speed. Further, the convective heat transfer rate between air and water film enhances due to high wind speed, leading to an increase in ice accretion area. This explains the effect of various wind speeds on the icing characteristics.

**Figure 7** illustrates the relationship between the maximum ice accretion thickness and ambient temperature, and wind speed. It is obvious that the maximum

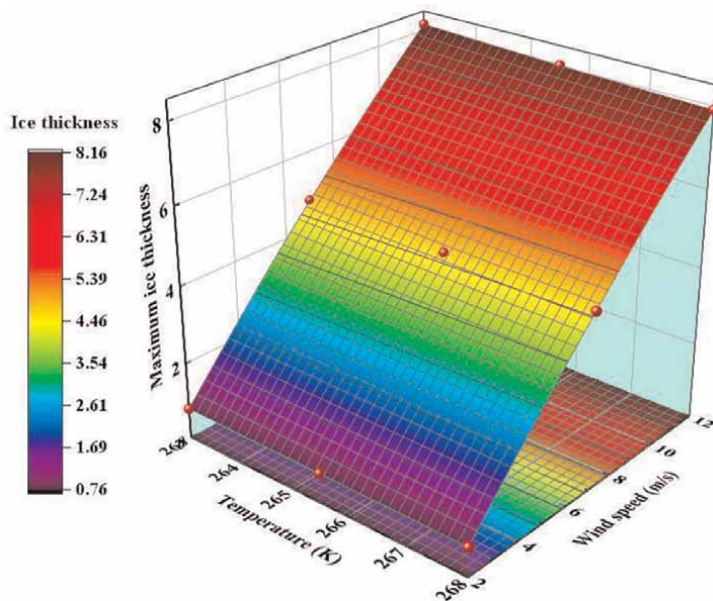


**Figure 7.**  
The maximum ice thickness for various temperatures and wind speeds.



ice thickness varies more significantly at wind speeds of 2–7 m/s than that at wind speeds of 7–12 m/s. This discrepancy can be attributed to the heat and mass transfer mechanism of water droplets on the blade airfoil. At lower wind speed, an increase in wind speed increases the mass rate of impinging water droplets at the leading edge, which is more dominant than water film evaporation caused by wind speed. Meanwhile, owing to the fact that convective heat transfer rate on the surface of water film enhances in terms of Stanton number, the water film will freeze to form thicker ice layer. At higher wind speed, the evaporation rate of water film and driving force acting on water film will become more significant. Therefore, the growth rate of the maximum water film become slower at high wind speed as compared to low wind speed. This explains the difference in ice growth rate at various wind speeds. The maximum ice thickness reduces slightly with an increase in ambient temperature. This is explained by the fact that the latent heat caused by solidification is not removed immediately at higher ambient temperature, leading to a decrease in ice accretion thickness. Additionally, investigating the maximum ice accretion thickness will lay a foundation for exploring anti-icing energy demand on the blade airfoil of wind turbines.

#### **4. Conclusions**

In this study, an icing model coupling water film flow with water film evaporation considering airfoil surface roughness has been developed to investigate the effect of icing conditions (ambient temperature and wind speed) on the icing characteristics (ice shape and ice thickness) of a blade airfoil for wind turbines by numerical simulation. The mechanism of heat and mass transfer for wind turbine icing under various icing conditions has been explored. The following conclusions have been obtained.

1. The simulated and experimental ice shapes on the airfoil agree well under different icing conditions.
2. With the ambient temperature decreasing from 268 to 263 K, the maximum ice accretion thickness increases from 4.55 to 4.73 mm due to an increase in the freezing fraction.
3. The ice shape contour fluctuates along the airfoil surface at higher ambient temperature due to water film flow and heat flux variation.
4. With the wind speed increasing in the range of 2–12 m/s, the maximum ice accretion thickness varies from 0.783 to 8.16 mm due to an increase in the droplet collection efficiency.
5. A large area of airfoil surface is covered by ice accretion at high wind speed due to an increase in driving force acting on water film and convective cooling between water film and air.
6. The maximum ice thickness changes more significantly at wind speeds of 2–7 m/s than that at wind speeds of 7–12 m/s.

## Acknowledgements

This study was supported by the National Youth Foundation of China (Grant No. 52106228).

## Conflict of interest

The author declares no conflict of interest.

## Appendices and nomenclature

$c$	chord length (m)
$c_{ice}$	specific heat capacity of ice (J/kg K)
$c_f$	specific heat capacity of water film (J/kg K)
$C_D$	drag coefficient
$d$	characteristic length (m)
$E$	internal energy (J/kg)
$Fr$	Froude number
$\vec{g}$	gravity vector (m/s <sup>2</sup> )
$h_f$	water film thickness (m)
$k$	thermal conduction coefficient (W/m K)
$k_s$	surface roughness (m)
$K$	inertia parameter
$L$	latent heat (J/kg)
$Le$	Lewis number
$LWC$	liquid water content (g/m <sup>3</sup> )
$\dot{m}$	mass rate per unit area (kg/m <sup>2</sup> s)
$\vec{n}$	surface normal vector
$\Omega$	pressure (Pa)
$\dot{Q}_h$	heat flux (W/m <sup>2</sup> )
$Re$	Reynolds number
$\bar{S}$	vorticity (1/s)
$St$	Stanton number
$t$	time (s)
$u$	temperature (K)
$\bar{T}$	equilibrium temperature (°C)
$\vec{V}$	velocity (m/s)
$y$	distance normal to the wall (m)

## Greek symbols

$\alpha$	droplet volume fraction
$\beta$	droplet collection efficiency
$\varepsilon$	emissivity
$\mu$	dynamic viscosity (Pa s)

$\bar{\nu}$  kinematic viscosity ( $\text{m}^2/\text{s}$ )  
 $\phi$  density ( $\text{kg}/\text{m}^3$ )  
 $\tau$  shear stress ( $\text{kg}/\text{m s}^2$ )

## Subscripts

1 air  
2 droplet  
evap evaporation  
fus fusion  
f water film  
ice ice  
subl sublimation  
 $\infty$  free stream

## Author details

Zhi Xu<sup>1,2</sup>


1 College of Engineering, Northeast Agricultural University, Harbin, China

2 Heilongjiang Provincial Key Laboratory of Technology and Equipment for the Utilization of Agricultural Renewable Resources in Cold Region, Northeast Agricultural University, Harbin, China

\*Address all correspondence to: [zxu@neau.edu.cn](mailto:zxu@neau.edu.cn)

## IntechOpen

---

© 2023 The Author(s). Licensee IntechOpen. This chapter is distributed under the terms of the Creative Commons Attribution License (<http://creativecommons.org/licenses/by/3.0>), which permits unrestricted use, distribution, and reproduction in any medium, provided the original work is properly cited. 

## References

- [1] Kusiak A, Zhang Z, Verma A. Prediction, operations, and condition monitoring in wind energy. *Energy*. 2013;**60**:1-12. DOI: 10.1016/j.energy.2013.07.051
- [2] Willis DJ, Niezrecki C, Kuchma D, Hines E, Arwade SR, Barthelmie RJ, et al. Wind energy research: State-of-the-art and future research directions. *Renewable Energy*. 2018;**125**:133-154. DOI: 10.1016/j.renene.2018.02.049
- [3] Cheng X, Shi F, Liu Y, Liu X, Huang L. Wind turbine blade icing detection: A federated learning approach. *Energy*. 2022;**254**:124441. DOI: 10.1016/j.energy.2022.124441
- [4] Zhang Y, Tang N, Niu Y, Du X. Wind energy rejection in China: Current status, reasons and perspectives. *Renewable and Sustainable Energy Reviews*. 2016;**66**:322-344. DOI: 10.1016/j.rser.2016.08.008
- [5] Jin JY, Virk MS. Study of ice accretion along symmetric and asymmetric airfoils. *Journal of Wind Engineering and Industrial Aerodynamics*. 2018;**179**:240-249. DOI: 10.1016/j.jweia.2018.06.004
- [6] Fu P, Farzaneh M. A CFD approach for modeling the rime-ice accretion process on a horizontal-axis wind turbine. *Journal of Wind Engineering and Industrial Aerodynamics*. 2010;**98**:181-188. DOI: 10.1016/j.jweia.2009.10.014
- [7] Homola MC, Virk MS, Wallenius T, Nicklasson PJ, Sundsbo PA. Effect of atmospheric temperature and droplet size variation on ice accretion of wind turbine blades. *Journal of Wind Engineering and Industrial Aerodynamics*. 2010;**98**:724-729. DOI: 10.1016/j.jweia.2010.06.007
- [8] Etemaddar M, Hansen MOL, Moan T. Wind turbine aerodynamic response under atmospheric icing conditions. *Wind Energy*. 2014;**17**:241-265. DOI: 10.1002/we.1573
- [9] Villalpando F, Reggio M, Ilinca A. Prediction of ice accretion and anti-icing heating power on wind turbine blades using standard commercial software. *Energy*. 2016;**114**:1041-1052. DOI: 10.1016/j.energy.2016.08.047
- [10] Yirtici O, Ozgen S, Tuncer IH. Predictions of ice formations on wind turbine blades and power production losses due to icing. *Wind Energy*. 2019;**22**:945-958. DOI: 10.1002/we.2333
- [11] Ibrahim GM, Pope K, Muzychka YS. Effects of blade design on ice accretion for horizontal axis wind turbines. *Journal of Wind Engineering and Industrial Aerodynamics*. 2018;**173**:39-52. DOI: 10.1016/j.jweia.2017.11.024
- [12] Wang Q, Yi X, Liu Y, Ren JH, Li WH, Wang Q, et al. Simulation and analysis of wind turbine ice accretion under yaw condition via an improved multi-shot icing computational model. *Renewable Energy*. 2020;**162**:1854-1873. DOI: 10.1016/j.renene.2020.09.107
- [13] Manatbayev R, Baizhuma Z, Bolegenova S, Georgiev A. Numerical simulations on static vertical axis wind turbine blade icing. *Renewable Energy*. 2021;**170**:997-1007. DOI: 10.1016/j.renene.2021.02.023
- [14] Son C, Kim T. Development of an icing simulation code for rotating wind turbines. *Journal of Wind Engineering and Industrial Aerodynamics*. 2020;**117**:104239. DOI: 10.1016/j.jweia.2020.104239

- [15] Son C, Kelly M, Kim T. Boundary-layer transition model for icing simulations of rotating wind turbine blades. *Renewable Energy*. 2021;**167**: 172-183. DOI: 10.1016/j.renene.2020.11.070
- [16] Baizhuma Z, Kim T, Son C. Numerical method to predict ice accretion shapes and performance penalties for rotating vertical axis wind turbines under icing conditions. *Journal of Wind Engineering and Industrial Aerodynamics*. 2021;**216**:104708. DOI: 10.1016/j.jweia.2021.104708
- [17] Reid T, Baruzzi GS, Habashi WG. FENSAP-ICE: Unsteady conjugate heat transfer simulation of electrothermal de-icing. *Journal of Aircraft*. 2012;**49**: 1101-1109. DOI: 10.2514/1.C031607
- [18] Beaugendre H, Morency F, Habashi WG. FENSAP-ICE's three-dimensional in-flight ICE accretion module: ICE3D. *Journal of Aircraft*. 2003;**40**:239-247. DOI: 10.2514/2.3113
- [19] Virk MS, Homola MC, Nicklasson PJ. Relation between angle of attack and atmospheric ice accretion on large wind turbine's blade. *Wind Engineering*. 2010;**34**:607-614. DOI: 10.1260/0309-524x.34.6.607
- [20] Ahn GB, Jung KY, Myong RS, Shin HB, Habashi WG. Numerical and experimental investigation of ice accretion on rotorcraft engine air intake. *Journal of Aircraft*. 2015;**52**:903-909. DOI: 10.2514/1.C032839
- [21] Hannat R, Morency F. Numerical validation of conjugate heat transfer method for anti/de-icing piccolo system. *Journal of Aircraft*. 2014;**51**:104-116. DOI: 10.2514/1.C032078
- [22] Clift R, Grace JR, Weber ME. *Bubbles, Drops, and Particles*. New York, New York: Academic Press; 1978. ISBN: 012176950X
- [23] Kim JW, Dennis PG, Sankar LN. Ice accretion modeling using an Eulerian approach for droplet impingement. In: 51st AIAA Aerospace Sciences Meeting; 07–10 January 2013. Grapevine, Texas: AIAA; 2013. pp. 1-11
- [24] Beaugendre H, Morency F, Habashi WG, Benquet P. Roughness implementation in FENSAP-ICE: Model calibration and influence on ICE shapes. *Journal of Aircraft*. 2003;**40**:1212-1215. DOI: 10.2514/1.2318
- [25] Zhang ZX, Dong ZN. *Viscous Fluid Mechanics*. Beijing: Tsinghua University Press; 1999 (in Chinese)
- [26] Croce G, De Candido E, Habashi WG, Munzar J, Aube MS, Baruzzi GS, et al. Analytical model for spatial and temporal evolution of in-flight icing roughness. *Journal of Aircraft*. 2010;**47**:1283-1289. DOI: 10.2514/1.47143
- [27] Gao L, Liu Y, Hu H. An experimental investigation of dynamic ice accretion process on a wind turbine airfoil model considering various icing conditions. *International Journal of Heat and Mass Transfer*. 2019;**133**:930-939. DOI: 10.1016/j.ijheatmasstransfer.2018.12.181
- [28] Battisti L. *Wind Turbines in Cold Climates*. *Green Energy and Technology*; 2015. DOI: 10.1007/978-3-319-05191-8
- [29] Shin J, Bond TH. Results of an icing test on a NACA0012 airfoil in the NASA Lewis icing research tunnel. In: 30th Aerospace Sciences Meeting & Exhibit; 6–9 January 1992. Reno, Washington: AIAA; 1992. pp. 1-19



## Chapter 2

# An Overview of Power Loss Estimation in Wind Turbines Due to Icing

*Oluwagbenga Apata and Tadiwa Mavende*

### Abstract

Wind turbines are susceptible to severe meteorological conditions, which can result in power loss. Several methods have been proposed to estimate the extent of power loss in wind turbines. This chapter aims to establish a foundation for new research and investigations into the impact of icing on wind turbine power output. It provides an overview of various methodologies available for estimating power loss in wind turbines under icing conditions. One of the prominent methods utilized in the past decade is computational fluid dynamics (CFD), enabling three-dimensional numerical simulations of wind turbines. When combined with the blade element momentum theory (BEM), CFD can also facilitate two-dimensional simulations. By analyzing these methodologies, researchers can gain insights into the estimation techniques suitable for studying icing effects on wind turbine performance. Understanding the magnitude of power loss under icing conditions is crucial for optimizing wind turbine design, operation, and maintenance strategies. Overall, this chapter contributes to the body of knowledge by consolidating various methods employed for power loss estimation in wind turbines subjected to icing.

**Keywords:** CFD, BEM, icing conditions, wind turbine, power loss

### 1. Introduction

Wind energy has emerged as one of the most promising and sustainable sources of electricity generation in recent years. Wind turbines, comprising large rotating blades, convert the kinetic energy of wind into electrical energy. However, wind turbines are subject to various operational challenges, one of which is the formation of ice on the turbine blades during cold and humid conditions, especially in Nordic countries characterized by higher wind potential. It is predicted that the installed wind power capacity in cold climates will increase to 224 GW in 2025 from the reported power of 156 GW in 2020 [1]. However, icing on wind turbine blades has a significant impact on their performance, leading to reduced power generation and increased maintenance costs [2–6]. This occurs when supercooled liquid droplets or freezing rain come into contact with the blades and freeze upon impact. This ice accumulation alters the aerodynamic properties of the blades, resulting in decreased lift and increased drag

forces. As a consequence, the turbine experiences reduced rotational speed and power output.

The phenomenon of power loss in wind turbines due to icing has garnered substantial attention in recent years, as it poses a significant challenge for wind farm operators and renewable energy stakeholders. Accurate estimation of the power loss caused by icing is crucial for efficient wind turbine operation, maintenance planning, and optimizing overall power generation. The impact of icing losses on the yearly power output and aerodynamic performance of the wind turbine is reported in [2, 7] respectively.

Traditionally, the assessment of ice accretion effects on wind turbines has been limited to two-dimensional analyses, focusing on a simplified representation of an airfoil section of the blade. However, horizontal-axis wind turbines (HAWTs) usually have a twisted blade geometry comprising of multiple section forms [8]. To accurately capture the impact of icing, three-dimensional simulations are necessary to account for the intricate blade geometry. It's important to note that icing effects extend beyond the blade itself, affecting the entire wind turbine. Various three-dimensional phenomena come into play, such as the influence of airflow along the radial direction induced by the rotation of the blades. Considering these three-dimensional effects is crucial for a comprehensive understanding of the icing's impact on the wind turbine system.

Several factors influence the magnitude of power loss due to icing in wind turbines. The severity of icing is primarily determined by environmental conditions, including air temperature, humidity, and wind speed. Other factors such as the design and characteristics of turbine blades, the type of ice formed, and the operating conditions of the turbine also play a role in determining the extent of power loss. Estimating the power loss due to icing is a complex task that requires a multidisciplinary approach. Researchers and engineers have employed various methodologies to quantify the impact of icing on wind turbine performance. Experimental investigations, computational fluid dynamics (CFD) simulations, and field measurements have been utilized to understand the aerodynamic effects of ice accretion and its subsequent influence on turbine power production.

This chapter focuses on the current state-of-the-art in estimating power loss in wind turbines under icing conditions using numerical methods, particularly computational fluid dynamics (CFD). It aims to provide a comprehensive understanding of the modeling of icing phenomenon and the analysis of wind turbine performance. The objective is to present the available methods for quantifying power loss in wind turbines when subjected to icing conditions. The study also recognizes the significance of comprehending and addressing the consequences of icing on wind turbines, considering its considerable influence on power generation, structural stability, and operational safety. The primary objective of this research is to enhance our understanding of icing phenomena by examining the different factors involved and investigating methodologies for estimating power losses in wind turbines when subjected to icing conditions. Through an analysis of existing research and identification of research gaps, this study aims to facilitate the advancement of improved icing prediction systems and effective mitigation strategies within the wind energy industry.

The chapter is structured into several sections: Section 2 explains the CFD approach used for simulating ice accretion, Section 3 discusses the Blade Element Momentum (BEM) theory for aerodynamic analysis, Section 4 reviews the CFD-BEM and three dimensional (3D) CFD approaches, and finally, Section 5 presents the main conclusions and future research directions.



## 2. CFD approach used for icing conditions in wind turbines

CFD-based models for icing conditions in wind turbines involve using techniques to simulate and analyze the impact of ice accretion on wind turbine performance. These models aim to provide insights into the complex interactions between airflow, water droplets, ice formation, and the resulting effects on turbine aerodynamics and power production. CFD-based models for icing conditions in wind turbines provide valuable insights into the complex phenomena associated with ice formation and its impact on turbine performance. These models aid in understanding the icing risks, optimizing turbine design, and developing effective strategies to mitigate the adverse effects of icing in wind energy applications. As shown in [8, 9], the numerical simulation of the CFD-based model can be described by fluid flow simulation, surface thermodynamics, droplet behavior and phase changes.

### 2.1 Fluid flow simulation

Fluid flow simulation in CFD-based models for icing conditions in wind turbines involves simulating the airflow around the turbine components to understand the complex flow patterns and their interaction with ice formation. By simulating the fluid flow around wind turbines using CFD-based models, engineers and researchers can gain valuable insights into the complex flow phenomena associated with icing conditions. This information is crucial for optimizing turbine designs, assessing ice-related risks, and developing mitigation strategies to enhance the safety and performance of wind energy systems.

The fundamental equations that describe fluid flow are the Navier-Stokes equation [10] which are used to solve for the velocity, pressure, and temperature fields in the flow domain. In the case of steady-state simulations, the equations simplify to the Reynolds-averaged Navier-Stokes (RANS) equations. In their general form, the Navier-Stokes equations can be written as follows:

Conservation of mass (continuity equation):

$$\partial\rho/\partial t + \nabla \cdot (\rho\mathbf{u}) = 0 \quad (1)$$

where  $\rho$  is the density of the fluid,  $t$  is time,  $\mathbf{u}$  is the velocity vector, and  $\nabla$  represents the divergence operator.

Conservation of momentum (Navier-Stokes equations):

$$\partial(\rho\mathbf{u})/\partial t + \nabla \cdot (\rho\mathbf{u} \otimes \mathbf{u}) = -\nabla p + \nabla \cdot \boldsymbol{\tau} + \rho\mathbf{g} \quad (2)$$

where  $\partial(\rho\mathbf{u})/\partial t$  is the rate of change of momentum,  $\otimes$  represents the outer product (tensor product),  $p$  is the pressure,  $\boldsymbol{\tau}$  is the stress tensor, and  $\mathbf{g}$  is the gravitational acceleration vector.

Conservation of energy:

The energy equation accounts for the conservation of thermal energy and can be written as:

$$\partial(\rho e)/\partial t + \nabla \cdot (\rho e + p) \mathbf{u} = \nabla \cdot (k\nabla T) + \nabla \cdot (\mu_{\text{eff}}\nabla \mathbf{u}) + \rho \mathbf{u} \cdot \mathbf{g} \quad (3)$$

where  $\partial(\rho e)/\partial t$  is the rate of change of energy,  $e$  is the internal energy per unit mass,  $p$  is the pressure,  $k$  is the thermal conductivity of the fluid,  $T$  is the temperature,

$\mu_{\text{eff}}$  is the effective viscosity,  $\nabla T$  is the gradient of temperature, and  $\mathbf{u} \cdot \mathbf{g}$  represents the dot product of velocity and gravitational acceleration.

These equations, coupled with appropriate boundary conditions, form the basis for solving fluid flow problems using the Navier-Stokes equations. It's worth noting that the equations can be further simplified and specialized depending on the specific assumptions and modeling techniques used in different scenarios. Appropriate boundary conditions need to be specified to simulate the icing conditions accurately. This includes specifying the inlet conditions (velocity, temperature, and turbulence properties), the airfoil/wind turbine blade surface conditions, and the icing conditions (e.g., supercooled droplet size, liquid water content). An icing model is incorporated to simulate the growth and accumulation of ice on the wind turbine blades. These models typically consider the impingement of supercooled water droplets, heat transfer, phase change, and ice accretion processes. Different icing models exist, such as the Messinger model or the Leontiev model, which can be implemented based on the specific requirements of the simulation.

Since turbulence plays a crucial role in wind turbine flows, the choice of turbulence model depends on factors such as the level of accuracy required, computational resources available, and the specific flow characteristics being simulated. The Reynolds-Averaged Navier-Stokes (RANS) models and Large Eddy Simulation (LES) models remain the two commonly used turbulence models [9]. In the RANS model, the governing equations of fluid motion, known as the Navier-Stokes equations described above, are averaged in time. This averaging process results in the set of equations that describe the mean flow behavior. The time-averaged equations are then solved numerically to obtain the mean flow field.

The RANS equations are expressed in terms of the mean velocity components, pressure, and other flow properties. These equations include the conservation of mass, momentum, and energy, similar to the original Navier-Stokes equations. However, in the RANS model, additional terms called Reynolds stresses appear in the momentum equations to account for the effect of turbulent fluctuations on the mean flow.

To close the RANS equations, a turbulence model is needed to approximate the Reynolds stresses. The turbulence model provides a closure relation for the Reynolds stresses based on the mean flow variables. The most commonly used turbulence model in RANS simulations is the eddy viscosity model, where the Reynolds stresses are related to the mean velocity gradients through an eddy viscosity coefficient.

The eddy viscosity coefficient is usually determined by solving an additional transport equation called the turbulence model equation. This equation accounts for the evolution of turbulence and provides a link between the mean flow and the turbulent fluctuations. Different turbulence models, such as the k-epsilon model [2, 11], the Spalart-Allmaras model [12], k-omega models [13] and the Reynolds Stress models (RSM) [14] have all been developed with varying levels of complexity and accuracy to capture different aspects of turbulence.

The k-epsilon models are based on the two-equation approach, which includes transport equations for turbulent kinetic energy (k) and its dissipation rate (epsilon). The eddy viscosity is computed using the turbulent kinetic energy and the turbulent length scale. Popular variations include the Standard k-epsilon model and the RNG k-epsilon model, which employ different assumptions and closure coefficients. This model is quite popular because of its relatively steady, good, and rapid convergence rate as well as low computational cost. However, in some cases, it is not adequate in flows with high-pressure gradients.

Similar to k-epsilon models, k-omega models are also two-equation models. They involve transport equations for turbulent kinetic energy ( $k$ ) and the specific dissipation rate ( $\omega$ ). The eddy viscosity is calculated using the turbulent kinetic energy and the turbulent frequency, which is related to the specific dissipation rate.

RSMs consider the full Reynolds stress tensor in the turbulent flow equations. These models involve solving transport equations for the six components of the Reynolds stress tensor, and the eddy viscosity is computed from the resolved Reynolds stresses.

The Spalart-Allmaras model is a one-equation model which employs a transport equation for the eddy viscosity, which is determined based on the turbulent kinetic energy and a modified turbulent length scale. The model introduces a turbulent viscosity that adapts to the flow's nature, including near-wall effects and low-Reynolds-number flows. Due to its ability to strike a balance between computational efficiency and desired precision in turbulent flow simulations, this turbulence model finds widespread use in the field of aerodynamics. Moreover, numerous researchers have acclaimed this model as the top-performing choice for accurately simulating ice accumulation on electrical cables, wind turbines, and aircraft.

It's worth noting that these models have their own advantages and limitations, and their performance varies depending on the flow characteristics and specific applications. The choice of a suitable turbulence model depends on factors such as flow regime, geometrical complexity, and available experimental or reference data for validation. Once the RANS equations and the turbulence model are defined, they can be solved numerically using appropriate numerical methods, such as finite difference, finite volume, or finite element methods. The resulting simulations provide information about the mean flow field, including velocity profiles, pressure distribution, and other important flow characteristics.

The LES models are more computationally demanding but provide a higher level of turbulence resolution. Unlike the Reynolds-averaged Navier-Stokes (RANS) model that relies on averaging turbulent fluctuations, LES focuses on resolving large-scale turbulent structures while modeling the effect of small-scale fluctuations. In LES, the flow is divided into large eddies and small-scale turbulence. The large eddies, which contain the most significant energy-containing structures, are resolved directly in the simulation, while the small-scale turbulence is modeled. This approach allows for a more accurate representation of the flow physics compared to RANS models. The LES equations consist of the filtered Navier-Stokes equations, where a filter operation is applied to the flow variables to separate the resolved scales from the unresolved ones. This filter operation effectively removes the small-scale fluctuations, and the resulting equations are then solved numerically to simulate the resolved flow field. To model the unresolved scales, a subgrid-scale (SGS) model is employed. The SGS model represents the effect of small-scale turbulence on the resolved flow by providing closure relations for the filtered variables. These closure relations are typically based on assumptions and modeling approaches, such as the Smagorinsky model, which relates the SGS stress tensor to the strain rate of the resolved flow.

The LES approach requires resolving a sufficient range of turbulent scales to capture the important features of the flow. This is achieved by using a fine computational mesh that can resolve the larger eddies while employing suitable numerical schemes to capture the details of the flow dynamics. LES is particularly useful for studying flows with significant turbulence and large-scale structures, such as turbulent boundary layers, swirling flows, and turbulent wakes. It provides more accurate predictions compared to RANS models and is often used in engineering applications

where capturing detailed turbulence dynamics is critical. However, LES simulations are computationally expensive due to the high resolution required to resolve the large eddies. Therefore, LES is generally used for research purposes or in cases where the detailed understanding of the turbulence physics is essential. In practical engineering simulations, hybrid approaches combining RANS and LES, such as detached eddy simulation (DES), are often employed to strike a balance between accuracy and computational cost.

Both the RANS and LES models introduce additional equations to account for turbulence quantities such as turbulent kinetic energy and turbulent dissipation rate. The computational domain is discretized into a grid or mesh of cells or elements. This discretization can be structured (e.g., Cartesian) or unstructured (e.g., tetrahedral or hexahedral elements). The governing equations are then solved numerically on this grid using methods such as finite volume, finite element, or finite difference techniques. The discretized equations are solved iteratively using numerical algorithms. The solution procedure involves applying appropriate solvers to compute the flow field variables, such as pressure, velocity, and temperature. The solution is obtained by iterating until convergence is achieved. Once the simulation is complete, post-processing is carried out to analyze the results. This may involve visualizing the flow patterns, calculating performance metrics (e.g., power output, thrust), and evaluating the ice accretion on the wind turbine blades.

Different turbulence models can lead to discrepancies in predicting turbulent flows due to their inherent assumptions and limitations. Some of the discrepancies that can arise from turbulence models include but not limited to boundary layer flows, complex geometries, compressible flows and high Reynolds number flows.

The k-epsilon model is known to struggle with accurately predicting near-wall flows, such as boundary layers. It can overpredict the turbulent kinetic energy near walls, leading to incorrect velocity profiles and flow separation predictions. Reynolds stress models, on the other hand, offer improved predictions in boundary layers by explicitly considering the Reynolds stress terms. They capture the anisotropic nature of turbulence and can provide more accurate velocity profiles and boundary layer characteristics.

Turbulence models like the Spalart-Allmaras model may have limitations in predicting separated flows accurately. They might fail to capture the complex behavior near separation regions, resulting in inaccurate pressure distributions and flow reattachment lengths. Reynolds stress models, with their ability to account for the anisotropy of turbulence, can offer better predictions of separated flows, including reattachment locations and flow structures.

Turbulence models, including k-epsilon, k-omega, and Spalart-Allmaras, may struggle in simulating flows around complex geometries, such as bluff bodies or turbomachinery. They might provide less accurate predictions of flow separation, pressure losses, and flow recirculation regions. Reynolds stress models, with their explicit modeling of Reynolds stress terms, have the potential to better capture complex flow features and flow physics in such scenarios.

The k-epsilon model and Spalart-Allmaras model can be limited in accurately predicting compressible flows, especially in regions with shock waves or strong density gradients. They might fail to capture the complex interactions between turbulence and compressibility effects. Reynolds stress models and some k-omega models, which explicitly account for the Reynolds stress terms, can better handle compressible flows and provide improved predictions of shock-boundary layer interactions.

## 2.2 Surface thermodynamics

Surface thermodynamics deals with the heat transfer processes occurring at the surface of the wind turbine blades. In the presence of icing conditions, the transfer of heat between the blade surface and the surrounding air is crucial. The surface temperature distribution affects ice accretion and subsequent ice behavior. Modeling surface thermodynamics involves considering factors such as conduction, convection, and radiation heat transfer mechanisms. By accurately modeling surface thermodynamics, the simulation can provide insights into the temperature distribution on the wind turbine blades.

Heat conduction occurs when there is a temperature gradient within a solid material. In the case of wind turbine blades, heat is conducted from the interior of the blade to the surface. The thermal conductivity of the blade material determines how efficiently heat is transferred. It is important to accurately model the heat conduction within the blade, considering its composition and any internal temperature variations that may arise due to operational conditions or heating elements. The heat conduction equation, based on Fourier's law, governs the conduction process:

$$q = -k \nabla T \quad (4)$$

where  $q$  is the heat flux vector,  $k$  is the thermal conductivity, and  $\nabla T$  is the temperature gradient. By solving this equation, the temperature distribution within the blade can be determined, which directly affects the surface temperature.

Convection refers to the transfer of heat between a solid surface and a moving fluid (in this case, air). In icing simulations, convective heat transfer occurs between the wind turbine blade surface and the surrounding air, affecting the blade temperature and ice formation. The convective heat transfer coefficient,  $h$ , characterizes the rate of heat transfer through convection. It depends on several factors, including the local flow velocity, air properties (density, viscosity, and specific heat capacity), blade surface geometry, and roughness. Determining the convective heat transfer coefficient can be challenging as it relies on accurately capturing the complex flow patterns around the blade surface. Empirical correlations, such as those based on Nusselt number relationships, or more advanced CFD methods can be employed to estimate the convective heat transfer coefficient in the icing simulation.

Radiation heat transfer occurs through electromagnetic waves emitted by a surface. In the context of wind turbine blades, both incoming solar radiation and thermal radiation from the surrounding environment contribute to the heat exchange. The net radiation heat transfer between the blade surface and its surroundings depends on various factors, including the surface emissivity, absorptivity, reflectivity, and the temperature difference between the blade and the surroundings. It's important to consider the radiative properties of the blade surface and account for both solar and thermal radiation in the icing simulation.

Surface roughness influences the formation and behavior of the boundary layer, which affects the convective heat transfer. Rough surfaces can disrupt the laminar flow and induce turbulence, enhancing heat transfer and potentially altering ice formation patterns. Accurate representation of the blade surface roughness is crucial for realistic icing simulations. Wettability refers to the ability of the surface to repel or retain water. Hydrophobic surfaces can reduce ice adhesion and promote ice shedding. Surface coatings or modifications can be incorporated in the simulation to represent different surface conditions.

There are various physical models available that plays a crucial role in examining the thermodynamic properties of the icing process on wind turbine blades when water droplets impact the blade surface. One pioneering and significant contribution in this area is the Messinger model, dating back to 1953. The Messinger model is a numerical approach based on the first-order differential equations of mass conservation and heat transfer that relates to icing and is based on the temperature of unheated surfaces. The Messinger model serves as the fundamental basis for simulating icing on aircraft wings, however, its application has been extended to wind turbine systems employing a straightforward approach that relies on mass and energy balance principles as shown in Eqs. (5) and (6) respectively.

$$\dot{m}_{in} + \dot{m}_{imp} = \dot{m}_{ice} + \dot{m}_{e,s} + \dot{m}_{out} \quad (5)$$

$$\dot{Q}_{cov} + \dot{Q}_{es} + \dot{Q}_{imp} = \dot{Q}_{kin} + \dot{Q}_{ice} + \dot{Q}_{in} \quad (6)$$

$\dot{m}_{in}$  is the rate of water inflow,  $\dot{m}_{out}$  is the rate of water outflow,  $\dot{m}_{imp}$  is the rate of droplets impingement,  $\dot{m}_{ice}$  is the ice accretion rate and  $\dot{m}_{e,s}$  is either the rate of evaporation or the rate of sublimation depending on the type of ice.

The Messinger model performs well for dry icing conditions, where there is low liquid water content (LWC) in the air, and the air temperature is considerably below freezing. However, the model encounters difficulties when dealing with conditions that involve higher LWC and air temperatures closer to freezing. To address this limitation and improve the model's predictive capabilities under conditions of higher LWC and air temperatures near freezing, an extension to the Messinger model was proposed. This extension involves the incorporation of conduction terms, which helps enhance the model's accuracy and reliability in such scenarios. By including these conduction terms, the improved model can better handle conditions with higher LWC and air temperatures close to freezing, providing more accurate predictions of ice formation on structures in these challenging conditions. Ice formation relies on the extended Messinger model, which is a conventional approach utilizing differential equations to describe phase change phenomena, known as the Stefan problem. This thermodynamic model relies on a phase transition phenomenon, commonly referred to as the Stefan problem. The model is controlled by the conduction of heat through both ice and water, as well as considerations of mass balance and the conditions for phase change as shown in the equations below.

$$\frac{\partial T}{\partial t} = \frac{k_i}{\rho_i C_{pi}} \frac{\partial^2 T}{\partial y^2} \quad (7)$$

$$\frac{\partial \theta}{\partial t} = \frac{k_w}{\rho_w C_{pw}} \frac{\partial^2 \theta}{\partial y^2} \quad (8)$$

$$\rho_i \frac{\partial B}{\partial t} + \rho_w \frac{\partial h}{\partial t} = \rho_a \beta V_\infty + \dot{m}_{in} - \dot{m}_{e,s} \quad (9)$$

$$\rho_i L_F \frac{\partial B}{\partial t} = k_i \frac{\partial T}{\partial y} - k_w \frac{\partial \theta}{\partial y} \quad (10)$$

where  $\theta$  and  $T$  are the temperatures,  $k_w$  and  $k_i$  are the thermal conductivities,  $C_{pw}$  and  $C_{pi}$  are the specific heats,  $h$  and  $B$  are the thicknesses of water and ice layers, respectively.

To obtain the ice and water thicknesses and the temperature distribution at each layer, specific boundary and initial conditions need to be defined. These conditions are established on the basis of the following assumptions:

- a. The ice is assumed to be in perfect contact with the airfoil surface, and its temperature is considered equal to the air temperature.
- b. The temperature remains continuous at the boundary between ice and water, where it is set to the freezing temperature.
- c. At the interface between air and water (glaze ice) or air and ice (rime ice), the heat flux is influenced by various factors, including convection, radiation, latent heat release, cooling caused by incoming droplets, heat carried by runback water, evaporation or sublimation, aerodynamic heating, and the kinetic energy of incoming droplets.
- d. Airfoil surface is initially clean

Another frequently utilized model is the Makkonen model, which formulates a differential equation representing the gradual accumulation of ice over time. This model incorporates the LWC in the equation to characterize the ice accretion process. The Makkonen model readily facilitates the simulation of ice load and ice accretion rate. Typically, ice load is expressed in kg/m, while the ice accretion rate is given in kg/m/h. The latter measurement pertains to each meter of the cylinder employed in the model. Alternatively, the ice accretion rate may be presented in terms of active ice hours, denoting the hours when the ice accretion rate exceeds a predefined threshold, often set at 10 g/m/h. This model relies on three fractions: collision efficiency, sticking efficiency, and accretion efficiency. Makkonen model variants in combination with numerical weather prediction (NWP) can predict icing and production losses on wind turbines.

The challenge associated with employing physical models is the absence of measured values for parameters like liquid water content (LWC) and median volume diameter (MVD). As a result, Numerical Weather Prediction (NWP) is utilized to estimate these values. However, this approach has a limitation in that these estimated values are typically available for the entire wind park, and not at a per wind turbine level. Though the Messinger and Makkonen models can both be used to simulate ice accretion in wind turbines, they may have discrepancies in their approaches and predictive capabilities. While the Messinger model is primarily based on first-order differential equations of mass conservation and heat transfer. It focuses on the energy required for icing protection and the freezing fraction of impinging water. On the other hand, the Makkonen model involves a differential equation that describes the ice accretion over time, considering the LWC as a key parameter.

### **2.3 Droplet behavior**

The concept of droplet behavior is important to understand the formation and growth of ice on turbine surfaces. Droplet behavior refers to the motion and interaction of water droplets in the air, which can lead to ice accretion on turbine blades. To simulate droplet behavior in CFD models, several key phenomena need to be considered. These include droplet transport, evaporation, collision/coalescence, and impingement.

Droplet transport involves modeling the motion of individual water droplets in the airflow around the turbine. The transport of droplets can be described using the equations of motion, taking into account the forces acting on the droplets, such as gravity, drag, and lift forces. The Navier–Stokes equations are typically solved to determine the airflow, and droplet trajectories are computed based on the local flow field.

Water droplets can evaporate as they travel through the air due to the difference in vapor pressure between the droplet and its surroundings. The rate of droplet evaporation can be estimated using various empirical or semi-empirical correlations, such as the Reynolds analogy or the Hertz-Knudsen equation. These correlations relate the evaporation rate to factors such as droplet size, temperature, relative humidity, and air velocity.

In regions with a high concentration of droplets, collisions between droplets can occur, leading to coalescence (merging) or breakup. The probability of collision and the resulting droplet behavior depend on factors like droplet size, relative velocity, and the concentration of droplets. These effects are typically modeled using stochastic or statistical methods, such as the Smoluchowski coagulation equation or the kinetic theory of coalescence.

When droplets come into contact with a solid surface, such as wind turbine blades, they can impinge and freeze, leading to ice accretion. The impingement process depends on the droplet size, impact velocity, surface temperature, and surface characteristics. Empirical models or experimental data are often used to determine the droplet impingement efficiency, which represents the fraction of impinging droplets that freeze upon impact.

The droplets' behavior in wind turbine icing can be described by considering the icing phenomenon as a multiphase flow because the icing rate may be affected by a mixture of ice, air, and liquid water since icing on wind turbine surfaces involves the simultaneous presence of multiple phases [15]. By treating the system as a multiphase flow, it becomes possible to model and understand the behavior of these phases, their interactions, and their effects on the icing process. Multiphase flow analysis allows for the consideration of interactions between the different phases. In the case of wind turbine icing, this includes the interaction between liquid water droplets and the turbine surfaces, the interaction between droplets and the surrounding air, as well as the growth and interaction of ice with the other phases. These interactions play a significant role in determining the rate and characteristics of ice formation. Several models are used to study droplet behavior in wind turbine icing. These models aim to simulate and understand the complex interactions between droplets, ice, and the surrounding air. The Lagrangian Particle Tracking model (LPT) and the Eulerian model remain the most used models for simulating disperse phase present in multiphase flows [16].

The Lagrangian Particle Tracking Model is a computational approach that tracks individual droplets as Lagrangian particles in the flow field surrounding a wind turbine. It is commonly used to analyze the behavior of liquid water droplets, including their impingement, adhesion, and freezing. The Lagrangian Particle Tracking Model employs Newton's equations of motion to solve for the movement of each individual droplet or particle. It incorporates a collision model to handle interactions between particles. The trajectory calculation of the particles involves two steps: (1) determining the particle motion based on Newton's second law and the forces acting on the particle, excluding collisions, such as gravity and the fluid phase's traction force on the particle. (2) Considering the particle's collision with another particle. The utilization of this method is commonly seen in 2D icing analysis. To assess the icing rate, the



velocities of water droplets are determined by numerically tracking a few droplets near the object experiencing icing. However, tracking a sufficient number of droplets in 3D to create the shape of the ice layer becomes computationally expensive [2].

In the context of wind turbine icing, an essential aspect of the LPT model is the consideration of droplet deposition on the turbine surfaces. Deposition models are used to determine whether droplets adhere to the surface based on criteria such as impact velocity and surface conditions. Additionally, droplet evaporation models may be incorporated to account for the reduction in droplet size due to the heat and mass transfer between the droplets and the surrounding air. To determine the forces acting on the droplets, the LPT model requires information about the fluid flow field. Typically, this information is obtained from a separate Computational Fluid Dynamics (CFD) simulation or experimental data. The fluid flow parameters, such as velocity, pressure, and turbulence characteristics, are interpolated from the CFD data to the droplet locations and times during the Lagrangian integration.

The Eulerian model, on the other hand, focuses on describing the behavior of the continuous fluid phase [17]. In this model, the fluid flow field is divided into a grid or mesh, and the governing equations for mass, momentum, and energy conservation are solved for each grid cell. The Eulerian model provides a detailed understanding of the fluid flow characteristics, such as velocity, pressure, and turbulence, which are critical for the behavior of the dispersed phase. Within the Eulerian framework, different sub-models are used to represent the dispersed phase, such as the volume fraction or concentration fields, and additional transport equations are solved to account for the interactions between the dispersed phase and the continuous phase.

In the Eulerian model, the flow domain is discretized into a structured or unstructured grid composed of cells or control volumes. The grid is a spatial representation of the domain where the fluid flow is simulated. Each grid cell represents a small portion of the domain, and the flow properties are computed at the cell centers or vertices. The Navier-Stokes equations, are solved for each grid cell in the Eulerian model. These equations include the conservation of mass (continuity equation) and the conservation of momentum (momentum equations). Additional equations, such as the energy equation, may be solved if heat transfer is significant in the system. These equations are solved numerically using appropriate discretization schemes, such as finite difference, finite volume, or finite element methods.

The Eulerian model calculates the flow variables, such as velocity, pressure, temperature, and turbulence characteristics, at each grid cell in the computational domain. These variables are represented as fields, meaning they are functions of space and time. The values of these variables are determined by solving the governing equations and considering the boundary conditions.

The conservation equations, derived from the Navier-Stokes equations, are solved for each grid cell. The continuity equation represents the conservation of mass, ensuring that mass is conserved within each control volume. The momentum equations represent the conservation of momentum and account for the various forces acting on the fluid, such as pressure gradients, viscous forces, and external body forces. Boundary conditions are essential in the Eulerian model to specify the flow behavior at the domain boundaries. Different types of boundary conditions are applied, such as velocity inlets, pressure outlets, wall boundaries, and symmetry conditions. These boundary conditions provide the necessary information to define the flow characteristics and interactions with the surroundings.

By solving the governing equations on the grid using the Eulerian model, detailed information about the flow field, including velocity profiles, pressure distributions,

and temperature variations, can be obtained. The Eulerian model is computationally efficient and well-suited for large-scale simulations of fluid flows, making it a valuable tool in various engineering applications, including aerodynamics, hydrodynamics, and industrial fluid dynamics.

The liquid water content (LWC) and droplet volume diameter have significant effects on the droplet collection efficiency. The collection efficiency refers to the fraction of droplets that are captured or collected by a specific surface or device. The LWC represents the amount of liquid water present in a unit volume of air. It has a direct impact on the droplet collection efficiency. Generally, as the LWC increases, the collection efficiency tends to increase as well. This is because a higher LWC implies a greater number of droplets available for capture, increasing the chances of collisions between the droplets and the capturing surface. The increased droplet concentration enhances the overall collection efficiency. The droplet volume diameter, often referred to as the droplet size, is the measure of the droplet's size or diameter. It plays a crucial role in determining the droplet collection efficiency. The relationship between droplet size and collection efficiency is complex and depends on various factors, including the capturing mechanism and the size of the capturing surface.

The combined effects of LWC and droplet volume diameter can be complex and interdependent. Higher LWC provides a higher number of droplets, which can compensate for the lower collection efficiency of smaller droplets due to factors like Brownian diffusion. In some cases, an optimal droplet size range may exist where the collection efficiency is maximized.

It's important to note that the specific capturing mechanism, the characteristics of the capturing surface, and the airflow conditions also influence the droplet collection efficiency. Additionally, the interaction between droplets, such as coalescence or breakup, can further complicate the behavior of droplet collection. Understanding the effects of LWC and droplet volume diameter on droplet collection efficiency is crucial for various applications, including aerosol sampling, wet scrubbers, and precipitation estimation in atmospheric science. Experimental measurements, numerical simulations, and theoretical models are often employed to investigate and quantify these effects under specific conditions and configurations.

## **2.4 Phase changes**

Phase changes play a vital role as a main component in CFD-based models for simulating wind turbine icing. These models incorporate phase change phenomena to accurately predict the formation, growth, and behavior of ice on turbine surfaces. Understanding phase changes is essential for optimizing turbine design, developing anti-icing strategies, and ensuring the safe and efficient operation of wind turbines in icy conditions.

In wind turbine icing, phase changes primarily involve the freezing of liquid water droplets and the subsequent growth of ice. When liquid water droplets come into contact with cold turbine surfaces or experience a decrease in temperature due to environmental conditions, they undergo a phase change from a liquid to a solid state, known as freezing. Freezing occurs when the droplets' temperature reaches the freezing point, causing a transformation into solid ice.

One crucial aspect of phase changes in wind turbine icing is supercooling. Supercooling refers to the phenomenon where a liquid is cooled below its freezing point without solidifying. Some liquid water droplets may experience supercooling before freezing due to factors such as a lack of ice nucleation sites or rapid cooling

rates. Supercooling delays the phase change from liquid to solid until a critical temperature or external stimulus triggers the nucleation and growth of ice crystals.

Nucleation is the initial formation of ice crystals or nuclei within a supercooled liquid. In wind turbine icing, nucleation can occur on the surfaces of turbine blades or on the droplets themselves. Nucleation serves as a starting point for ice growth, and it can be either heterogeneous or homogeneous. Heterogeneous nucleation happens when ice crystals form on foreign particles or surface irregularities, while homogeneous nucleation occurs spontaneously in a homogeneous liquid.

Following nucleation, ice crystals continue to grow by attracting water molecules from the surrounding liquid or by condensing water vapor from the air. Ice growth is a crucial phase change mechanism in wind turbine icing as it leads to the formation of a solid ice layer. The rate of ice growth depends on various factors, including temperature, humidity, liquid water availability, and the presence of impurities. Understanding these factors and their interactions is essential for accurately modeling ice growth in CFD-based models.

Sublimation is another phase change phenomenon of significance in wind turbine icing. Sublimation occurs when ice directly changes from a solid to a gas without going through the liquid phase. In icing conditions, sublimation can cause ice on the turbine surfaces to evaporate, reducing ice accretion and mitigating the effects of icing. Proper consideration of sublimation in CFD-based models helps assess the loss of ice and its impact on turbine performance.

Incorporating phase changes into CFD-based models involves several considerations and modeling techniques. Numerical simulations and experimental studies utilize phase change models to simulate the freezing process accurately, account for supercooling effects, predict ice growth rates, and estimate ice accretion patterns on turbine surfaces. These models consider factors such as heat transfer, energy exchange, nucleation kinetics, and ice growth mechanisms. Numerous numerical methods for simulating vapor/liquid phase change in CFD have been developed. The commonly utilized methods include the volume-of-fluid (VOF) method [18, 19], level set (LS) method [20], front-tracking method (FT) [21], and the hybrid VOF/LS method [22].

The volume-of-fluid (VOF) method also known as the Enthalpy-Porosity method, is a widely used approach for simulating phase change. It tracks the volume fractions of different phases (e.g., liquid water, ice, and vapor) within a computational domain. The method solves conservation equations for mass, momentum, energy, and species transport, and uses a source term to account for phase change effects. Notwithstanding its slightly lower accuracy in capturing interface curvature, the volume-of-fluid (VOF) method has gained popularity due to its good conservative properties and relatively high computational efficiency [23]. The Level Set Method is another popular approach for tracking phase interfaces and capturing phase change phenomena. It represents the interface between different phases as a level set function. By solving an advection equation for the level set function, the method tracks the evolution of the phase interface and enables the simulation of phase change processes. The Front Tracking Method is a technique that tracks the position and characteristics of sharp phase interfaces, such as the solid-liquid interface during phase change. It involves discretizing the interface into discrete points or markers and solving equations for the motion and deformation of these markers. This method is particularly useful when simulating complex and irregular phase change interfaces.

The various phase change models used in CFD simulations each have their strengths and limitations. The VOF method is known for its good conservative

properties. It accurately preserves mass and volume fractions of the different phases during phase change simulations. The FT method generally maintains good conservation properties as it explicitly tracks the phase interface. However, proper implementation is crucial to ensure accurate conservation. The LS method can face challenges in accurately conserving mass and volume fractions due to numerical diffusion and interface smearing, especially for large-scale simulations.

The LS method is generally computationally more expensive than the VOF method. Solving the advection equation for the level set function requires additional computational effort, making it comparatively slower. The FT method can be computationally expensive due to the need to explicitly track individual interface markers. The computational cost increases as the complexity and number of markers increase.

The LS method offers better accuracy in capturing interface curvature compared to the VOF method. It represents the phase interface as a level set function, allowing for more accurate representation of sharp and complex interfaces. The FT method typically provides excellent accuracy in capturing interface curvature. By explicitly tracking the movement and deformation of interface markers, it can accurately represent sharp phase interfaces. The VOF method may exhibit slightly inferior accuracy in capturing interface curvature. This is because it uses a piecewise-constant representation of the phase interface, which can lead to some numerical diffusion and smearing of sharp features.

### **3. Blade Element Momentum (BEM) theory**

Blade Element Momentum (BEM) theory is a mathematical approach used to analyze the aerodynamic performance of rotating blades, particularly in wind turbine applications. It provides a detailed understanding of how the blades interact with the oncoming wind and generate lift and drag forces. The BEM theory provides a comprehensive understanding of the aerodynamic behavior of wind turbine blades, allowing for the optimization of rotor design and performance prediction [12]. While it simplifies the analysis by treating the blade as a series of individual sections, it provides valuable insights into the complex interactions between the blades and the surrounding air flow. The accuracy of BEM theory depends on the assumptions made, such as the airfoil characteristics, wake modeling, and tip loss corrections, which can be refined to improve the accuracy of the predictions.

The BEM theory divides the rotor blade into a number of small elements along its span, typically referred to as blade sections or blade elements. Each element is treated as an isolated airfoil and analyzed individually based on local conditions, such as local wind speed, local angle of attack, and airfoil characteristics. The main concept of BEM theory is to break down the complex aerodynamic interaction between the blade and the flow field into simpler, manageable calculations for each element. By considering the local conditions at each element, such as the local wind speed and the local angle of attack, the theory provides a detailed understanding of how the blade generates lift and drag forces.

Each blade element is typically represented by its own airfoil, which is characterized by specific lift and drag coefficients that depend on the angle of attack. These coefficients are typically obtained from experimental data or airfoil databases. The angle of attack at each element is determined by the relative wind direction, which is the vector sum of the inflow wind speed and the induced velocity caused by the rotor's rotation and wake effects from neighboring blades. Using the lift and drag coefficients

and the local conditions, the theory calculates the lift and drag forces acting on each blade element. The resultant force is then resolved into axial (thrust) and tangential (torque) components. The axial force represents the thrust generated by the rotor, while the tangential force contributes to the torque and rotational motion of the rotor.

To account for the induced effects caused by the rotor's rotation, BEM theory considers the changes in flow direction and the additional velocity induced by the blades. The induced velocity is typically modeled as a combination of axial and tangential components. It represents the downwash effect caused by the generation of lift. At the blade tips, BEM theory applies Prandtl's tip loss correction [24, 25]. The correction accounts for the reduced efficiency at the tips due to the high-pressure gradient and vortex shedding. The correction is typically applied by reducing the effective angle of attack at the blade tips compared to the angle of attack at the mid-span sections. This reduction in effective angle of attack is proportional to the strength of the tip vortices and is determined based on empirical or analytical models. By incorporating the tip loss correction, the BEM theory provides more accurate predictions of the aerodynamic forces and power production of the wind turbine. It improves the estimation of thrust and torque at the blade tips, which are crucial parameters for evaluating the performance and efficiency of the rotor. It reduces the calculated forces at the blade tips to improve the accuracy of the analysis. By integrating the calculated forces for each blade element along the rotor span, the theory provides an estimation of the overall thrust and torque generated by the rotor. These parameters are crucial for assessing the aerodynamic performance and power production of the wind turbine.

There are several different tip loss models used in the analysis of wind turbine aerodynamics to account for the reduced efficiency and increased losses at the blade tips. These models aim to capture the impact of tip vortices on the performance of the rotor. The Prandtl's Classical Tip Loss Model [26, 27] is the original tip loss model proposed by Ludwig Prandtl. It assumes that the tip vortices are concentrated at the blade tips and that the flow behaves as if the blade ends at a virtual point called the "ideal tip." The model applies an idealized downwash distribution along the spanwise direction to account for the induced flow caused by the tip vortices.

The Glauert's Tip Loss Model, developed by Friedrich Glauert is an extension of Prandtl's classical tip loss model. It considers the spanwise distribution of downwash and introduces a correction factor, known as the Glauert correction, to adjust the effective angle of attack at the blade tips. The correction factor is derived based on assumptions about the circulation distribution along the span. It considers that the circulation decreases linearly from the root to the tip of the blades. This assumption implies that the strength of the tip vortices decreases towards the tip, leading to a reduction in the downwash effect on the downstream blades. The Glauert correction factor is defined as the ratio between the local induced velocity at the blade tip and the axial velocity of the inflow wind. It is typically denoted by the symbol "F" and is a function of the local radial position along the blade span. By incorporating the Glauert correction factor, the effective angle of attack at the blade tips is adjusted, which in turn affects the lift and drag forces acting on the blades. This correction helps to improve the accuracy of the analysis by accounting for the downwash effects and the resulting reduction in lift production near the blade tips. It is important to note that the Glauert model assumes an idealized spanwise circulation distribution and does not account for some complex phenomena, such as tip leakage flow or three-dimensional effects. While it provides a significant improvement over the classical model, it still involves simplifications and assumptions to make the analysis tractable.

Goldstein's Tip Loss Model is a comprehensive approach that accounts for the complex behavior of tip vortices and their impact on the aerodynamic performance of wind turbine blades. It was developed by Alan Goldstein and provides a more accurate estimation of the downwash effect at the blade tips compared to simpler models. Goldstein's model considers the tip vortices as a rotating vortex sheet along the blade tips, taking into account the variation in the strength of the vortices and the associated downwash distribution. The model utilizes a complex variable method to calculate the induced velocities and adjust the effective angle of attack at the blade tips. In Goldstein's model, the blade tip is treated as a line source of vorticity, and the flow around the blades is represented by a complex potential function. This complex potential function enables the representation of both the velocity and vorticity fields in a unified manner. By solving the complex potential equation, Goldstein's model determines the induced velocities caused by the tip vortices at each point along the span of the blades. These induced velocities are then used to adjust the effective angle of attack, taking into account the downwash effect on the downstream blades. The strength of the tip vortices is determined by the circulation distribution along the blades, which can be estimated based on the rotor's operating conditions and the geometric characteristics of the blades. The model incorporates the variation in circulation along the span to capture the changes in tip vortex strength. The downwash distribution resulting from the tip vortices is determined by the superposition of the individual downwash velocities caused by each vortex. The induced velocities and downwash distribution are then used to adjust the effective angle of attack at the blade tips, influencing the lift and drag forces acting on the blades. Goldstein's Tip Loss Model provides a more accurate representation of the complex behavior of the tip vortices compared to simpler models. It takes into account the spatial variation of the vortices and provides a more refined estimation of the downwash effect on the blades. This allows for improved predictions of the aerodynamic performance and power production of wind turbines, especially at high tip speed ratios and under highly loaded conditions. It is worth noting that Goldstein's model is computationally more demanding than simpler tip loss models due to the need to solve the complex potential equation and consider the detailed vorticity distribution. However, with the advancements in computational tools and resources, this model has gained popularity in research and advanced engineering analyses to provide more accurate insights into the behavior of wind turbine blades near the tips.

#### **4. Estimation of power loss in wind turbines under icing conditions**

Estimating power loss in wind turbines under icing conditions is a complex task due to the varied and dynamic nature of ice accretion on the blades. Several factors contribute to power loss, including changes in aerodynamic performance, additional weight on the blades, and altered turbine operation.

Icing alters the smooth surface of wind turbine blades, leading to an increase in surface roughness. This roughness causes more air resistance (drag) as the blades rotate through the wind. Consequently, the blades experience reduced lift and a lower ability to convert wind energy into rotational motion, resulting in decreased power generation. As ice accumulates on the turbine blades, it adds significant weight to the rotating components. The extra weight affects the blades' rotational speed, requiring more force from the wind to maintain the same rotation rate. This increased resistance decreases the turbine's ability to capture wind energy efficiently and reduces power

output. To prevent damage and excessive stress on the blades, wind turbines may adjust their operation during icing events. Blade pitch control is one method used to regulate blade angles and reduce the impact of icing. Additionally, turbines may partially shut down or enter a “de-icing mode” to allow accumulated ice to shed off, thereby protecting the turbine’s structural integrity. These operational adjustments during icing events lead to reduced power generation.

The severity of the icing event plays a crucial role in the power loss experienced by wind turbines. Light icing may have a minimal impact on power output, whereas severe icing can cause substantial reductions. Moreover, different types of ice, such as rime ice or glaze ice, have distinct physical properties that affect aerodynamics differently, leading to varying levels of power loss. Wind turbine blades are designed to optimize aerodynamic efficiency under normal conditions. Some turbines incorporate specialized coatings or materials on the blade surfaces to reduce ice adherence or facilitate ice shedding. Additionally, active anti-icing systems, like blade heating, may be employed to prevent or reduce ice formation. The effectiveness of these design features and anti-icing systems influences the extent of ice accretion and power loss during icing events. The wind speed and direction during icing events play a significant role in the ice distribution on the turbine blades. Icing patterns can be non-uniform, with varying ice thickness along the blade length, depending on the wind characteristics. Turbines may experience higher power losses when encountering turbulent and gusty wind conditions during icing events. Local climate conditions, including ambient temperature and humidity, impact ice formation and adhesion on the turbine blades. Colder temperatures generally lead to more severe icing, while humidity levels affect the water content in the air, influencing the potential for ice accretion.

Estimating power loss accurately requires a comprehensive understanding of these factors, along with access to meteorological data, turbine design specifications, and icing event observations. Developers and investors in wind farms rely on a thorough understanding and accurate assessment of the losses caused by icing. This is essential for estimating the expected energy generation of a project, assessing associated risks, and evaluating its financial feasibility. This section provides an overview of the CFD-BEM and full three-dimensional (3D) CFD methodologies for power loss estimation in wind turbines as a result of icing conditions.

#### **4.1 CFD-BEM approach**

The CFD-BEM (Computational Fluid Dynamics - Blade Element Momentum) approach is a computational technique that combines the strengths of CFD and BEM theory to analyze and design wind turbines [28, 29]. This approach provides a comprehensive understanding of the aerodynamic behavior and performance of wind turbine blades, allowing for more accurate predictions and optimizations [30]. While BEM theory is computationally efficient and provides a good estimation of the overall aerodynamic performance of wind turbine rotors, it lacks the ability to capture three-dimensional effects, flow unsteadiness, and complex flow phenomena. CFD, on the other hand, can simulate the detailed flow behavior but is computationally expensive. The CFD-BEM approach bridges this gap by utilizing CFD simulations to generate inputs for the BEM analysis, enabling more accurate predictions of the turbine performance.

In the CFD-BEM approach, CFD simulations are performed to model the flow field around the wind turbine. This can be achieved by incorporating appropriate ice

accretion models based on the environmental conditions, such as temperature, humidity, and liquid water content. The CFD component of the approach simulates the airflow and the movement of water droplets in the vicinity of the turbine blades. These simulations help to predict the ice accretion pattern and its effects on the blade surfaces. The CFD solver solves the governing equations of fluid flow, typically the Navier-Stokes equations, in a computational domain that includes the turbine geometry and the surrounding flow domain. The simulations consider the wind inflow conditions, the rotor geometry, and the rotational motion of the blades. The CFD solver discretizes the domain into a grid or mesh and solves the equations iteratively to obtain the flow velocities, pressures, and other flow characteristics while in the BEM analysis, the rotor blades are divided into small sections or elements along the span. Each element is treated as an isolated airfoil and analyzed based on local conditions such as the local wind speed, angle of attack, and airfoil characteristics.

CFD is used to discretize the entire fluid domain into a grid of cells, where the governing equations (typically the Navier-Stokes equations) are solved for each cell. On the other hand, BEM is employed to discretize the boundaries or surfaces of objects in the domain, where the integral form of the governing equations is solved. In this approach, the discretization scheme involves volume discretization where the fluid domain is divided into a finite number of cells, usually using techniques like structured or unstructured grids. Structured grids have a regular arrangement of cells, such as a Cartesian or curvilinear grid. Unstructured grids have cells with arbitrary shapes, which can be more flexible for complex geometries. The boundaries or surfaces of objects in the domain are discretized into a collection of elements. These elements can be triangles, quadrilaterals, or other suitable shapes depending on the geometry and requirements of the problem. The choice of element shape affects the accuracy and efficiency of the BEM calculations. Once the domain is discretized, numerical integration methods are employed to approximate the integral terms in the governing equations. These integrals arise due to the BEM formulation, where the influence of boundary values on the interior points is determined. Various integration schemes like Gaussian quadrature or midpoint rule can be used depending on the accuracy requirements and complexity of the problem. The boundary conditions, such as velocities or pressures, are prescribed or obtained from the problem statement. These conditions are then applied to the discretized boundary elements, ensuring that the appropriate values are used during the calculations. The discretized equations, including the CFD equations for the interior cells and the BEM equations for the boundary elements, are solved iteratively or simultaneously. The solution procedure involves solving the equations for each cell or element while considering the interdependence between neighboring cells or elements. Once the solution is obtained, post-processing is performed to analyze and visualize the results. This may involve calculating derived quantities of interest, such as forces, velocities, or pressure distributions, and presenting them in a suitable format for analysis or presentation.

In the context of the CFD-BEM approach, the iterative method refers to the iterative process used to solve the discretized equations of the combined CFD and BEM formulations [31]. Since the CFD and BEM equations are coupled through the boundary conditions, an iterative approach is employed to obtain a converged solution. The process starts with an initial guess for the solution variables. These variables can include the velocity components, pressure, and other relevant quantities. The CFD equations for the interior cells are solved using the current values of the solution variables. This typically involves discretizing the governing equations, applying boundary conditions, and solving the resulting system of equations using numerical



methods like finite difference, finite volume, or finite element techniques. With the updated values of the solution variables from the CFD step, the BEM equations for the boundary elements are solved. This involves evaluating the influence coefficients between boundary elements and determining the boundary values at each element. The boundary values are typically obtained by integrating the influence of neighboring elements and interior cell values using numerical integration techniques. The BEM-calculated boundary values are then used to update the boundary conditions for the CFD calculations. These updated boundary conditions are applied in the subsequent CFD step to solve the equations for the interior cells. This coupling ensures consistency between the CFD and BEM solutions. The BEM-calculated boundary values are then used to update the boundary conditions for the CFD calculations. These updated boundary conditions are applied in the subsequent CFD step to solve the equations for the interior cells. This coupling ensures consistency between the CFD and BEM solutions. Once the iterative process has converged and a satisfactory solution is obtained, post-processing is performed to analyze and visualize the results. This may include calculating derived quantities, generating plots or animations, and extracting relevant information for further analysis or interpretation.

The BEM analysis uses the inputs from the CFD simulations to estimate the lift, drag, and other aerodynamic forces on each blade element. These forces are integrated along the blade span to obtain the overall aerodynamic performance of the rotor, including thrust, power, and torque. The CFD simulations provide the necessary inputs for the BEM analysis, including the local wind flow conditions and the aerodynamic characteristics of the airfoils. The CFD results, such as the flow velocities and pressures, are interpolated and integrated into the BEM analysis to obtain more accurate estimates of the aerodynamic forces and power output of the wind turbine. This integration is typically performed at specific points along the blade span, where the BEM analysis is carried out.

Using the aerodynamic forces obtained from the BEM analysis, the power loss in the wind turbine can be estimated. The power output of a wind turbine is directly related to the aerodynamic forces acting on the blades. By comparing the power output of the iced turbine with the power output of the clean turbine (without ice accretion), the power loss can be quantified. The power loss is typically expressed as a percentage of the clean turbine power. In addition to the overall power loss estimation, the CFD-BEM approach can also provide insights into load-based power losses. Ice accretion affects the distribution of aerodynamic forces along the blade span, leading to uneven loading on different blade sections. This uneven loading can result in structural and fatigue issues. By analyzing the changes in load distribution caused by ice accretion, the CFD-BEM approach can estimate load-based power losses and identify critical areas prone to structural concerns. By considering load-based power losses, the CFD-BEM approach provides a comprehensive analysis of the impact of icing on wind turbine performance beyond the overall power loss estimation.

Power loss estimation also considers the dynamic effects induced by ice accretion. Ice adds mass to the blades, altering their natural frequencies and mode shapes. This can lead to resonant vibrations and increased fatigue damage. The CFD-BEM approach accounts for these dynamic effects by incorporating the changes in blade properties due to ice accretion, allowing for a more accurate estimation of power losses associated with blade dynamics. Ice accretion on wind turbine blades is a time-dependent process, with ice formation, growth, and shedding occurring over time. The CFD-BEM approach can perform time-dependent analyses to capture the temporal evolution of ice accretion and its impact on power losses. By simulating the icing

process and updating the BEM analysis at different time steps, the approach provides a more realistic estimation of the dynamic power losses associated with changing ice conditions.

To account for uncertainties in the power loss estimation, the CFD-BEM approach can incorporate uncertainty quantification techniques. Uncertainties may arise from variations in meteorological conditions, ice accretion models, and input parameters. By performing sensitivity analyses and probabilistic simulations, the approach can provide confidence intervals or probability distributions of the estimated power losses, allowing for a better understanding of the associated uncertainties.

## **4.2 Full three-dimensional (3D) CFD approach**

3D CFD refers to the numerical simulation of fluid flow and heat transfer in three-dimensional geometries. It is a powerful tool used to analyze and predict the behavior of fluids under various conditions, including the estimation of power loss in wind turbines during icing conditions. When wind turbines operate in cold climates, they can be exposed to icing conditions where ice accretes on the rotor blades. The presence of ice on the blades can significantly impact their aerodynamic performance, leading to reduced power output and increased structural loads. To estimate the power loss caused by icing, 3D CFD simulations can be employed. This process typically involves geometry modeling, mesh generation, applying boundary conditions, solver and simulation and post-processing.

In geometry modeling, the wind turbine's components, including the rotor, nacelle, and blade surfaces, are accurately represented using computer-aided design (CAD) software. The rotor blades are typically modeled with high geometric fidelity, including airfoil shapes and surface roughness. The geometry model serves as the basis for constructing the computational domain for the CFD simulation. To model the wind turbine's rotor, nacelle, and other relevant components, detailed CAD models are created. The rotor blades are of particular importance and are modeled with high geometric fidelity. This includes accurately capturing the airfoil shapes, which determine the aerodynamic performance of the blades. The CAD model should also account for other blade characteristics such as twist, chord length, and surface roughness. Surface roughness plays a crucial role in determining the airflow behavior around the blades. It affects the boundary layer development, separation points, and ultimately the aerodynamic performance. Therefore, the CAD model must incorporate realistic surface roughness profiles based on the blade's manufacturing specifications. In addition to the blades, the nacelle, hub, and other wind turbine components are also modeled in detail. The nacelle includes the generator, gearbox, and control systems. The hub connects the rotor blades to the main shaft. Accurate representation of these components ensures that the simulation captures the overall behavior of the wind turbine system. The CAD model is typically created by experienced designers using specialized software. It requires expertise in wind turbine design and knowledge of the specific turbine being analyzed. The fidelity and accuracy of the geometry model have a direct impact on the reliability and accuracy of the subsequent CFD simulations. Once the geometry model is created, it needs to be converted into a suitable format for CFD simulations. This may involve meshing the geometry, which is the process of dividing it into small elements or cells for numerical analysis. The meshing process, discussed in the subsequent steps, is essential to accurately capture the flow behavior and aerodynamic characteristics of the wind turbine components. Overall,

the geometry modeling step establishes the foundation for the subsequent stages of the 3D CFD process. It ensures that the wind turbine components are accurately represented in the computational domain, allowing for realistic simulations and analysis of the fluid flow and heat transfer during icing conditions.

The computational domain is divided into small control volumes or cells through mesh generation. The mesh captures the geometric details of the wind turbine components and discretizes the computational domain. A fine mesh is crucial to capture the flow features accurately, especially near the blade surfaces. Advanced meshing techniques, such as boundary layer resolution and adaptive mesh refinement, may be employed to enhance the simulation's accuracy. There are various techniques for mesh generation, including structured, unstructured, and hybrid methods. In structured meshes, the cells are arranged in a regular, well-organized pattern, such as a Cartesian or cylindrical grid. Structured meshes offer good numerical accuracy and efficiency but may struggle to handle complex geometries. Unstructured meshes, on the other hand, allow for more flexibility in representing complex geometries. The cells in unstructured meshes can be of different sizes and shapes, adapting to the geometry of the wind turbine. They are typically generated using techniques like Delaunay triangulation or advancing front methods. Unstructured meshes are well-suited for capturing the flow features around complex geometries but can be computationally more expensive. Hybrid meshes combine structured and unstructured elements to leverage their respective strengths. For example, structured meshes can be used in regions where the geometry is relatively simple, while unstructured meshes can be employed in complex areas. Hybrid meshes provide a balance between accuracy and computational efficiency. Special attention should be given to the near-wall region, particularly around the blade surfaces, where the flow behavior is highly influenced by boundary layer effects. Fine mesh resolution is required in these regions to accurately capture the flow gradients and resolve the boundary layer structures. To improve the accuracy of the simulation, adaptive mesh refinement techniques can be employed. These techniques dynamically refine the mesh in areas with high flow gradients or areas of particular interest, such as regions experiencing ice accretion. By refining the mesh in these critical areas, the simulation can capture the local flow features more accurately without requiring an excessively fine mesh throughout the entire domain. Overall, mesh generation in 3D CFD involves selecting an appropriate mesh type (structured, unstructured, or hybrid) and generating a mesh with suitable resolution, especially in areas of interest. The goal is to strike a balance between accuracy and computational efficiency to ensure an effective simulation of the fluid flow and heat transfer in the wind turbine system during icing conditions.

The boundary conditions define the inflow conditions, environmental parameters, and ice accretion rates. These conditions are based on the anticipated environmental conditions during icing events. The wind inflow conditions specify the velocity, temperature, and humidity of the incoming air. Additional parameters such as ice water content and droplet size distribution are also considered to accurately model ice accretion on the blades.

The CFD solver numerically solves the governing equations, such as the Navier-Stokes equations, in the computational domain. The solver simulates the fluid flow, icing, and heat transfer processes, considering the time-dependent behavior of the icing process. The simulation progresses in discrete time steps, allowing the computation of the airflow, ice accretion, and thermal behavior of the wind turbine blades. The solver utilizes numerical algorithms and iterative methods to approximate the solutions of the governing equations.

Once the simulation is completed, post-processing techniques are employed to analyze and interpret the results. Visualization tools enable the examination of flow patterns, temperature profiles, and ice accretion distribution on the blade surfaces. Quantitative analysis provides insights into the power loss caused by icing. Power coefficients, which represent the efficiency of power conversion from the wind, are calculated and compared for different icing scenarios. These analyses help identify the regions of maximum power loss and provide valuable information for design optimization, such as anti-icing systems, blade de-icing strategies, and operational adjustments during icing events.

## **5. Future research directions and conclusion**

Future research in power loss estimation in wind turbines due to icing can explore several directions to improve our understanding and develop more accurate models for predicting and mitigating the effects of icing. Enhancing the accuracy of icing models is crucial for more precise power loss estimation. Future research can focus on developing advanced CFD models that capture the complex interaction between ice accretion, airflow, and turbine performance. Incorporating more detailed physics, such as ice formation and shedding dynamics, can lead to more accurate predictions of power loss. Current icing models primarily focus on the aerodynamic aspects of ice accretion, but future research can expand the scope to include multi-physics modeling. This involves incorporating thermal, mechanical, and electrical aspects of ice formation and shedding. By considering the thermodynamic behavior of ice formation, mechanical stresses induced by ice loading, and the electrical effects of ice on blade performance, more comprehensive models can be developed.

To improve the accuracy of icing models, it is essential to validate them using extensive field measurements. Collaborations with wind farm operators and instrumented turbine installations can provide valuable datasets on ice accretion and turbine performance under various icing conditions. These field measurements can serve as benchmark data for validating and refining icing models, enhancing their predictive capabilities. Light Detection and Ranging (LiDAR) technology has shown promise in measuring ice thickness and shape remotely. By emitting laser pulses and analyzing the reflected signals, LiDAR systems can provide detailed information about ice accumulation on wind turbine blades. Ongoing research can focus on improving the resolution and accuracy of LiDAR-based ice measurement techniques, enabling real-time monitoring of ice conditions across large wind farms. Also, combining data from multiple sensors and measurement techniques can enhance the accuracy and reliability of ice accretion estimation. By fusing data from LiDAR, thermal imaging, and optical methods, researchers can obtain a more comprehensive understanding of ice accumulation on wind turbine components. Data fusion techniques, along with advanced signal processing and data analysis algorithms, can be explored to improve the accuracy and robustness of ice measurement systems. Advancements in ice accretion measurement techniques will not only improve power loss estimation in wind turbines but also aid in the development of effective anti-icing and de-icing strategies.

While wind tunnel tests and scaled-down turbine experiments are useful for studying ice accretion, the scaling effects between laboratory conditions and full-scale wind turbines can introduce discrepancies. Future research can investigate the scaling laws and conduct full-scale testing to validate the models under real-world conditions. Full-scale testing provides a comprehensive understanding of the impact of icing on large wind

turbines and allows for the validation of model predictions at the actual operational scale. Comparative studies involving multiple wind turbine models and designs can provide insights into the influence of turbine characteristics on icing-related power loss. By testing different blade geometries, materials, and surface treatments, researchers can evaluate their performance under icing conditions. These studies help identify design features that are more resistant to ice accretion and shedding, leading to reduced power losses.

Research can focus on optimizing anti-icing and de-icing systems to improve their effectiveness and energy efficiency. This includes developing advanced coatings, heating technologies, and aerodynamic designs that minimize ice accretion or facilitate ice shedding. Exploring novel materials and techniques for preventing ice adhesion and developing adaptive de-icing systems can lead to more reliable and cost-effective solutions.

Icing has a significant impact on the performance and power loss in wind turbines. When ice accumulates on various parts of the turbine, it alters the aerodynamic characteristics, adds weight, and affects the overall operation of the turbine. Ice formation on the turbine blades disrupts the smooth flow of air and modifies the aerodynamic profile of the blades. The ice adds thickness and roughness, changing the shape of the airfoil and reducing its lift-to-drag ratio. As a result, the blades experience increased drag and reduced lift, leading to reduced turbine efficiency and power output. Icing can also cause increased turbulence in the airflow around the blades.

The irregular surface created by ice formations generates local flow separations, vortices, and eddies. This turbulent flow disrupts the ideal aerodynamic conditions and further reduces the efficiency of the blades. Turbulence also increases the loads on the turbine components, potentially leading to structural damage. Ice accumulation adds weight to the rotating turbine blades. The additional mass creates an imbalance, which can cause uneven loading on the rotor and generate vibrations. These imbalances and vibrations can lead to increased mechanical stresses and damage to the turbine structure, bearings, and other components. The presence of ice on the blades can cause erosion as the ice particles impact the leading edges. The repeated impact of ice particles can remove protective coatings and damage the blade surface, further degrading the aerodynamic performance and reducing power output.

Understanding and accurately estimating the power loss caused by icing is essential for optimizing wind farm operations, improving energy production efficiency, and ensuring the reliability of wind energy generation. In summary, power loss estimation in wind turbines due to icing is a complex and multi-faceted challenge. Ongoing research efforts, technological advancements, and collaborations between academia, industry, and policymakers are essential for improving the understanding of icing effects, refining prediction models, and implementing effective mitigation strategies. By addressing the power loss associated with icing, it is possible to enhance the reliability, efficiency, and economic viability of wind energy generation in cold climate regions, contributing to the sustainable and clean energy transition.

In conclusion, power loss estimation in wind turbines due to icing is a crucial aspect of wind farm operation in cold climate regions. Icing on wind turbine components, particularly the blades, can significantly impact performance and reduce power output. Overall, icing on wind turbines can cause a significant reduction in power output. The extent of power loss depends on the severity and duration of icing events, the turbine's design and anti-icing measures, and the specific aerodynamic and structural characteristics of the turbine. Proper monitoring, icing detection, and mitigation strategies are crucial to minimizing power losses and ensuring safe turbine operation in icing conditions.


## **Author details**

Oluwagbenga Apata\* and Tadiwa Mavende  
The Independent Institute of Education, IIEMSA, Johannesburg, South Africa

\*Address all correspondence to: [g.apata@ieee.org](mailto:g.apata@ieee.org)

## **IntechOpen**

---

© 2023 The Author(s). Licensee IntechOpen. This chapter is distributed under the terms of the Creative Commons Attribution License (<http://creativecommons.org/licenses/by/3.0>), which permits unrestricted use, distribution, and reproduction in any medium, provided the original work is properly cited. 

## References

- [1] Clifton A, Barber S, Stökl A, Frank H, Karlsson T. Research challenges and needs for the deployment of wind energy in hilly and mountainous regions. *Wind Energy Science*. 2022;**7**(6):2231-2254
- [2] Fu P, Farzaneh M. A CFD approach for modeling the rime-ice accretion process on a horizontal-axis wind turbine. *Journal of Wind Engineering and Industrial Aerodynamics*. 2010;**98** (4-5):181-188
- [3] Makkonen L, Laakso T, Marjaniemi M, Finstad KJ. Modelling and prevention of ice accretion on wind turbines. *Wind Engineering*. 2001;**25**(1):3-21
- [4] Jasinski WJ, et al. Wind turbine performance under icing conditions. 1998:60-65
- [5] Shu L, Li H, Hu Q, Jiang X, Qiu G, He G, et al. 3D numerical simulation of aerodynamic performance of iced contaminated wind turbine rotors. *Cold Regions Science and Technology*. 2018; **148**:50-62
- [6] Pedersen MC, Sørensen H. Towards a CFD model for prediction of wind turbine power losses due to icing in cold climate. In: 16th International Symposium on Transport Phenomena and Dynamics of Rotating Machinery; 2016 Apr; Honolulu, United States. <hal-01891321>
- [7] Jin JY, Virk MS. Study of ice accretion along symmetric and asymmetric airfoils. *Journal of Wind Engineering and Industrial Aerodynamics*. 2018;**179**: 240-249
- [8] Abbadi M, Mussa I, Lin Y, Wang J. Preliminary analysis of ice accretion prediction on wind turbine blades. In: AIAA Scitech 2020 Forum, Orlando, FL, 6-10 January 2020. DOI: 10.2514/6.2020-0619
- [9] Martini F, Contreras Montoya LT, Ilinca A. Review of wind turbine icing modelling approaches. *Energies*. 2021; **14**(16):5207
- [10] Virk M, Mughal U, Hu Q, Jiang X. Multiphysics based numerical study of atmospheric ice accretion on a full scale horizontal axis wind turbine blade. *The International Journal of Multiphysics*. 2016;**10**(3):237-246
- [11] Homola MC, Virk MS, Wallenius T, Nicklasson PJ, Sundsbø PA. Effect of atmospheric temperature and droplet size variation on ice accretion of wind turbine blades. *Journal of Wind Engineering and Industrial Aerodynamics*. 2010;**98**(12):724-729
- [12] Homola MC, Virk MS, Nicklasson PJ, Sundsbø PA. Performance losses due to ice accretion for a 5 MW wind turbine. *Wind Energy*. 2012;**15**(3): 379-389
- [13] Bai C-J, Wang W-C. Review of computational and experimental approaches to analysis of aerodynamic performance in horizontal-axis wind turbines (HAWTs). *Renewable and Sustainable Energy Reviews*. 2016;**63**: 506-519
- [14] Tian L, Song Y, Zhao N, Shen W, Wang T. AD/RANS simulations of wind turbine wake flow employing the RSM turbulence model: Impact of isotropic and anisotropic inflow conditions. *Energies*. 2019;**12**(21):4026
- [15] Van Wachem BGM, Almstedt AE. Methods for multiphase computational fluid dynamics. *Chemical Engineering Journal*. 2003;**96**(1-3):81-98

- [16] Contreras Montoya LT, Lain S, Ilinca A. A review on the estimation of power loss due to icing in wind turbines. *Energies*. 2022;**15**(3):1083
- [17] Lain S, Aliod R. Study on the Eulerian dispersed phase equations in non-uniform turbulent two-phase flows: Discussion and comparison with experiments. *International Journal of Heat and Fluid Flow*. 2000;**21**(3): 374-380
- [18] Carey VP. *Liquid-Vapor Phase-Change Phenomena: An Introduction to the Thermophysics of Vaporization and Condensation Processes in Heat Transfer Equipment*. United States: CRC Press; 2018
- [19] Rudman M. A volume-tracking method for incompressible multifluid flows with large density variations. *International Journal for Numerical Methods in Fluids*. 1998;**28**(2):357-378
- [20] Son G, Dhir VK, Ramanujapu N. Dynamics and heat transfer associated with a single bubble during nucleate boiling on a horizontal surface. *Journal of Heat and Mass Transfer*. 1999;**121**(3): 623-631
- [21] Unverdi SO, Tryggvason G. A front-tracking method for viscous, incompressible, multi-fluid flows. *Journal of Computational Physics*. 1992;**100**(1):25-37
- [22] Balcázar N, Lehmkuhl O, Jofre L, Rigola J, Oliva A. A coupled volume-of-fluid/level-set method for simulation of two-phase flows on unstructured meshes. *Computers & Fluids*. 2016;**124**: 12-29
- [23] Wang Y, Wang X, Chen H, Taylor RA, Zhu Y. A combined CFD/visualized investigation of two-phase heat and mass transfer inside a horizontal loop thermosiphon. *International Journal of Heat and Mass Transfer*. 2017;**112**:607-619
- [24] Hansen MO, Johansen J. Tip studies using CFD and comparison with tip loss models. *Wind Energy: An International Journal for Progress and Applications in Wind Power Conversion Technology*. 2004;**7**(4):343-356
- [25] Wood DH, Okulov VL, Bhattacharjee D. Direct calculation of wind turbine tip loss. *Renewable Energy*. 2016;**95**:269-276
- [26] Schmitz S. *Aerodynamics of Wind Turbines: A Physical Basis for Analysis and Design*. Hoboken, NJ: John Wiley & Sons; 2020
- [27] Edmunds M, Williams AJ, Masters I, Croft TN. An enhanced disk averaged CFD model for the simulation of horizontal axis tidal turbines. *Renewable Energy*. 2017;**101**:67-81
- [28] Mauro S, Lanzafame R, Messina M, Brusca S. On the importance of the root-to-hub adapter effects on HAWT performance: A CFD-BEM numerical investigation. *Energy*. 2023;**275**:127456
- [29] Martini F, Ibrahim H, Contreras Montoya LT, Rizk P, Ilinca A. Turbulence modeling of iced wind turbine airfoils. *Energies*. 2022;**15**(22): 8325
- [30] Zidane IF, Swadener G, Ma X, Shehadeh MF, Salem MH, Saqr KM. Performance of a wind turbine blade in sandstorms using a CFD-BEM based neural network. *Journal of Renewable and Sustainable Energy*. 2020;**12**(5):12-19
- [31] Bangga G. Comparison of blade element method and CFD simulations of a 10 MW wind turbine. *Fluids*. 2018; **3**(4):73



## Chapter 3

# A Review of Wind Turbine Icing Prediction Technology

*Lidong Zhang, Yimin Xu and Yuze Zhao*

### Abstract

The global wind energy business has grown considerably in recent years. Wind energy has a bright future as a major component of the renewable energy sector. However, one of the major barriers to the growth of wind energy is the freezing of wind turbine blades. The major solution to overcome the aforementioned problem will be to foresee wind turbine ice using existing anti-icing technologies. As a result, improving wind turbine ice prediction technology can assist wind farms in achieving more precise operation scheduling, avoiding needless shutdowns, and increasing power generation efficiency. Traditional wind turbine icing prediction methods have problems such as misjudgment and omission, while machine learning algorithms have higher accuracy and precision. Because of the rapid advancement of deep learning technology, machine learning algorithms have become an important tool for predicting wind turbine icing. However, in real applications, machine learning algorithms still face obstacles and limits such as inadequate data and poor model interpretability, which require additional study and refinement. This chapter discusses the application of machine learning algorithms in wind turbine icing prediction, provides a comprehensive description of the applicability and accuracy of various machine learning algorithms in wind turbine icing prediction, and summarizes the applications and advantages.

**Keywords:** wind turbine, icing prediction, machine learning, artificial neural network, forecasting accuracy

### 1. Introduction

The percentage of total power generation provided by wind has grown continuously as humanity has learned how to utilize wind resources. According to BP's World Energy Outlook 2023 [1], primary energy sources such as wind power would provide 25 to 55% of global primary energy from 2019 to 2050. Renewable and nuclear energy growth is predicted to meet all worldwide electricity demand between 2022 and 2025, according to the International Energy Agency's Electricity Market Report 2023, released in 2022 [2]. Wind resources' improving cost competitiveness, as well as legislative incentives, are driving the rapid spread of wind power [1]. Wind energy resource-rich areas of the world are primarily found in the northern hemisphere [3]. However, icing of wind turbine blades in cold climates [3, 4], single anti-deicing methods [5, 6], and imprecise wind turbine icing forecast are all issues in the growth of wind power

generation. Long-term wind turbine operation in cold weather conditions lowers power generation [6]. When icing conditions are met, water droplets in the air, rainfall, drizzle, or wet snow freeze or stick to wind turbine blades, resulting in the formation of ice. Wind turbine ice can shorten the life of components by causing uneven blade mass distribution and higher blade loading [7]. While moderate freezing can have an effect on the aerodynamic qualities of wind turbine blades, significant icing can cause the wind turbine to shut down completely, decreasing the efficiency of wind resource utilization [8]. Wind turbines exposed to mild or moderate ice for 10% of the year can lose 24% of their overall power production, whereas wind turbines exposed to icing for lengthy periods of time can lose up to 50% of their annual power production [9, 10]. Wind turbine shutdowns due to icing can result in not only power production losses, but also in large-scale power outages, as seen on February 14, 2021, in the United States, state of Texas, when cold weather hit Texas with a minimum temperature of  $-21^{\circ}\text{C}$  (the average winter temperature in Texas is  $1.4^{\circ}\text{C}$ ). Cold weather prompted the closure of 57.3% of wind turbines (about 18,000 MW), affecting nearly 4 million people [11]. Several contributing elements are currently unaccounted for in faulty wind turbine ice prediction models, making it difficult to effectively anticipate wind turbine icing [12, 13]. If historical meteorological data and data from Supervisory Control And Data Acquisition (SCADA) systems are included in classical ice prediction models, and then supervised machine learning methods are applied to forecast icing, the models can anticipate the majority of icing events [14–16].

To summarize, the advancement of wind power generation is a significant step toward a more sustainable energy future. Nonetheless, wind turbine ice continues to be a significant barrier to the effective and dependable use of wind resources. Accurate prediction of wind turbine ice may considerably increase wind turbine performance and assure power supply stability. It is consequently critical to continue researching and improving improved wind turbine ice prediction models.

## **2. Shallow machine learning-based wind turbine blade icing prediction method**

### **2.1 Neural network**

#### *2.1.1 BP neural network*

In 1986, Rumelhart et al. developed the error Backpropagation method [17], sometimes known as the BP algorithm, for training neural networks for the first time. The BP neural network is a shallow forward-type neural network that operates using the error backpropagation algorithm [17]. **Figure 1** depicts the basic idea of this neural network computational model, which comprises of an input layer [18, 19]. There is a concealed layer and an output layer. A large number of neurons are connected as network nodes, and each neuron processes the excitation function as the network weights' connection strength signal, and the pattern information contained in the input data is mapped to the output layer by adjusting these connection strengths. The information flow direction of forward propagation is input layer (**Figure 1** Layer1) → hidden layer (**Figure 1** Layer2) → output layer (**Figure 1** Layer3) [18, 19].

In 2019, Cheng et al. developed a BP neural network-based icing prediction model for the problem of wind turbine blade icing [20], which cannot be successfully predicted in advance, and testing results demonstrated that the model could

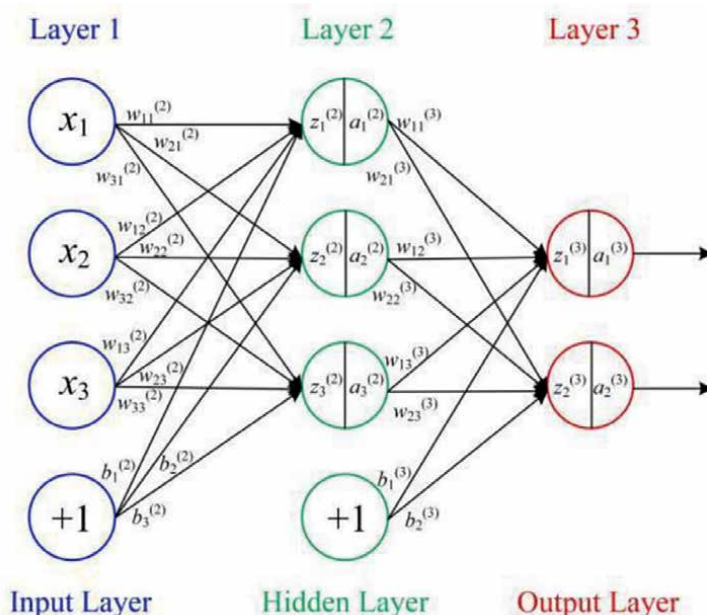


**Figure 1.**  
 Principle of BP neural network computational model.

predict blade icing with an accuracy of 0.984 [20]. Li et al. 2022 compared the trained BP neural network to the Radial Basis Function (RBF) neural network for leaf icing prediction in a research on prediction accuracy [21]. The BP neural network's relative percentage error was lower than the RBF network's using 12 sets of processed data, with an average  $E_{\text{whole}}$  value within 7.5%, indicating superior stability. The findings demonstrated the efficacy and superiority of BP neural networks in forecasting blade icing [21].

### 2.1.2 Elman neural network

The Elman Neural Network (ENN) is a feedback-based neural network model developed by American Psychologist J. L. Elman in 1990 [22, 23]. It has a simple design and outstanding performance. It works as shown in **Figure 2**. The forward neural network has an input layer (**Figure 2** Input Layer), a hidden layer (**Figure 2** Hidden Layer), and an output layer (**Figure 2** Output Layer), as well as a context layer, which is used to remember the hidden layer's output from the previous moment and calculate the characteristics of time-delayed data, giving it dynamic memory [22]. The Elman neural network can anticipate blade icing in wind turbine blade icing prediction applications by analyzing historical meteorological data such as temperature, humidity, and wind speed. Additionally, the Elman neural network can use blade icing thickness, icing time, and other icing data to reduce bias and thus improve prediction accuracy [20, 22, 23].

Cheng et al. used the trained Elman neural network to predict future values of icing-related characteristics in 2019 [20], and the prediction results revealed that the Elman neural network predicted blade icing defects with a 97.8% accuracy rate [20]. Cheng et al. used processed data to perform icing prediction comparison

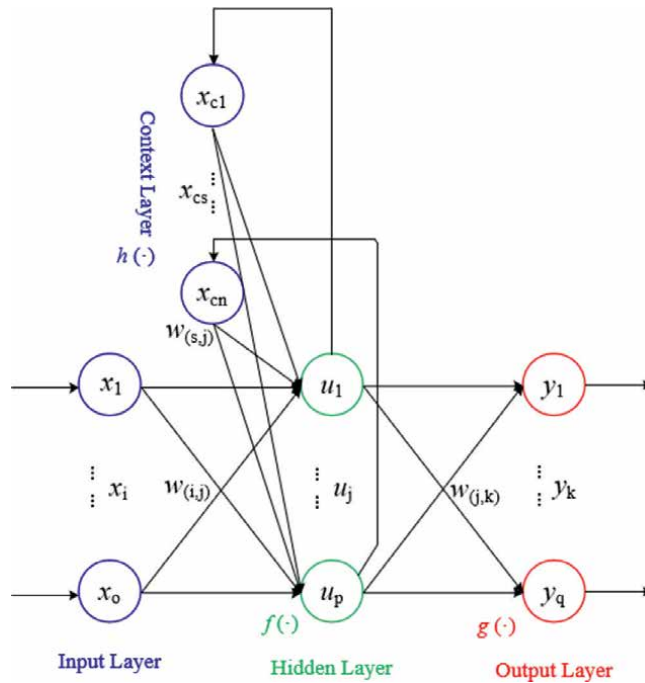


**Figure 2.** Principle of Elman neural network computational model.

tests between the Elman neural network and other neural networks in 2020 [24]. According to the testing results, the Elman neural network exhibited reduced deviation and obtained greater accuracy [24].

When the BP and Elman neural networks are compared, it becomes clear that the Elman network sacrifices computational accuracy for greater efficiency, whereas the BP network is better suited for specific complex models. Both networks have distinct benefits in wind turbine icing prediction, and the proper method may be chosen based on the actual scenario to handle the problem.

## 2.2 Integrated learning

### 2.2.1 Boosting

The Boosting approach is an ensemble learning method for improving classifier performance by combining a large number of weak classifiers [25, 26]. Two of the most well-known algorithms are AdaBoost and XGBoost. Because of its quick training speed and precise forecasting capabilities, XGBoost is an important tool in wind turbine blade icing prediction [27, 28]. The computational model principle of this method is depicted in **Figure 3**.

In 2019, Wang et al. utilized the XGBoost algorithm to predict the wind turbine blade icing process and compared the prediction results with those of traditional machine learning algorithms and neural networks. The XGBoost algorithm achieved higher accuracy in predicting blade icing, reaching up to 95.18%. In 2021 [29], Guo et al. constructed normal behavior models based on output power and rotor speed using the XGBoost algorithm, and the model error was as low as 0.53% [30].

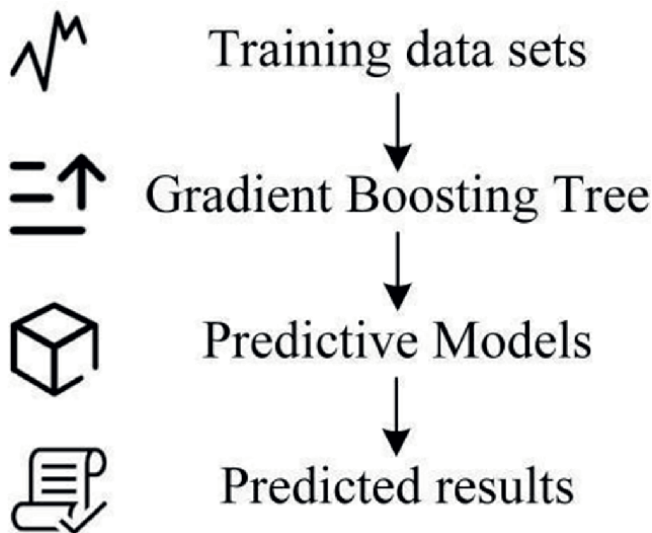


**Figure 3.**  
*Computational model principle of XGBoost algorithm.*

### 2.2.2 Stacking

The Stacking method is a machine learning methodology based on model integration that integrates many base models to build a prediction model that outperforms a single model [26]. The computational model principle of this method is depicted in **Figure 4**. The final prediction results are generated by taking the prediction results from the base model as extra features and then training and predicting these features using a meta-model [26, 31].

Li et al. used the Stacking method to anticipate wind turbine blade icing in 2022 by combining Relief and One-Dimensional Convolutional Superposition of Bidirectional Gated Recurrent Units (1D-CNN-SBiGRU). The prediction results reveal that the suggested technique improves the WA (Weighted Accuracy) by 43.08%/34.61%/14.44% when compared to SVM/CNN/BiLSTM, respectively [32].

### 2.2.3 Bagging

Bagging (Bootstrap Aggregating) is an additional integrated learning method that bootstraps the training set to generate multiple training sets, trains a weak learner based on each training set, and then fuses the prediction results of these weak learners into the final prediction result by voting or averaging to improve the model's accuracy and generalization ability. The computational model principle of this method is depicted in **Figure 5**. Bagging may be used to generate several blade icing prediction models and improve forecast accuracy by fusing the prediction outputs of various models in wind turbine blade icing prediction [28, 33].

Zhang et al. developed a CM technique based on KNN regression and bagging ensemble strategy to detect wind turbine operational conditions in 2022 and tested it with SCADA data gathered in the field [34]. The findings demonstrated that the ensemble model may achieve the anticipated estimate accuracy while also improving operating efficiency by around 30% [34].

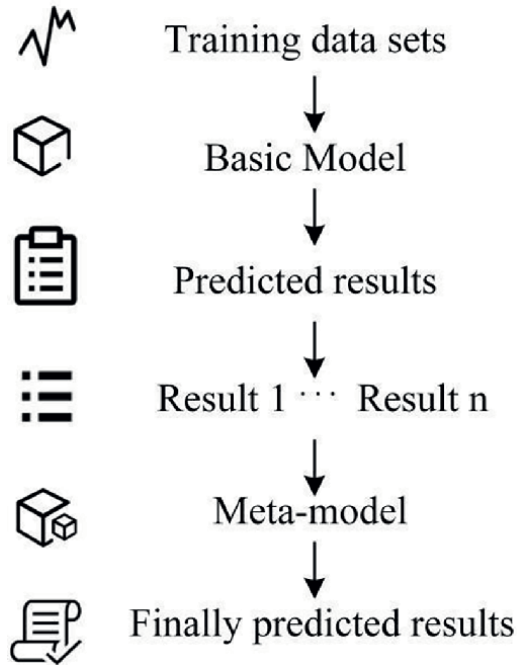


**Figure 4.** Computational model principle of stacking algorithm.

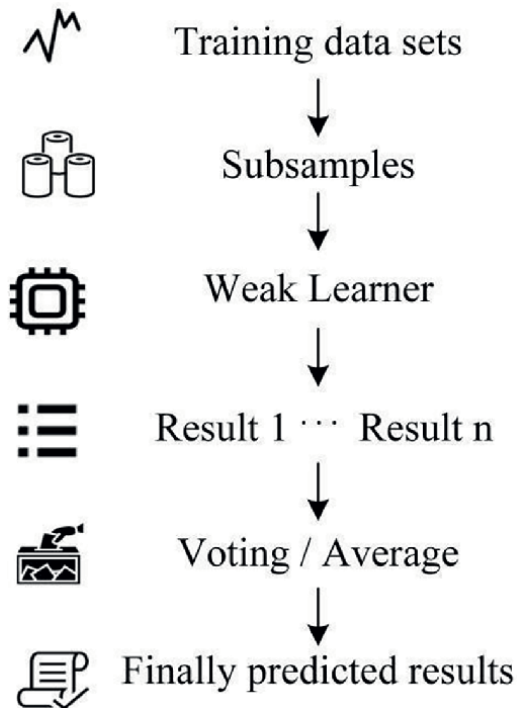


**Figure 5.** Computational model principle of bagging algorithm.

By summarizing the applicability and benefits as well as drawbacks of the three prediction algorithms discussed above, it is easy to conclude that the Bagging algorithm is appropriate when we need to predict complex icing conditions; the Boosting algorithm is appropriate when accuracy is required but data is sparse; and the Stacking algorithm may be a better choice when a high-performance prediction model with sufficient computational is required. In real-world applications, the approach must further consider factors like data amount, icing quality, and distribution, and so on.

### 3. Deep learning

In their 2006 publication “A fast learning algorithm for deep belief nets,” Hinton et al. developed the idea and learning algorithm of deep belief networks [35]. Deep learning reached a new stage of growth with the introduction of deep belief networks, and researchers began to investigate more complicated neural network topologies and sophisticated learning algorithms [36]. Deep learning’s core idea is to use a multilayer neuron structure to abstract and process data layer by layer, with each layer generating a new set of features for the next layer, so that more advanced features can be gradually acquired, eventually achieving accurate data classification and prediction. Deep learning has also been frequently employed in the prediction of wind turbine blade icing in recent years. Deep learning, as a sophisticated model learning method, can leverage historical data from wind turbine blades to accurately forecast and identify wind turbine blade icing conditions [35–38].

Several classical neural network models have emerged with the development of deep learning, including Convolutional Neural Network (CNN), Recurrent Neural Network (RNN), Deep Neural Networks (DNN), and Deep Belief Network (DBN). (DNN), Stacked Autoencoder (SAE), and Transfer Learning (TL). Specific applications of these neural network models to wind turbine blade icing prediction are discussed in this section.

#### 3.1 Convolutional neural networks

In their 1998 study “Gradient-Based Learning Applied to Document Recognition,” LeCun et al. established the topology of convolutional neural networks and successfully applied it to handwritten digit recognition [39]. Convolutional Neural Networks (CNN) are deep learning models that have gained popularity due to their excellent accuracy in image recognition applications. CNN’s core principle is to employ convolutional operations to extract features from multidimensional input, such as **Figure 6**, and to perform hierarchical feature representation using several convolutional and pooling layers (**Figure 6** Convolutional). Eventually, fully linked layers are used to execute classification, regression, and other tasks [37, 39]. Convolutional neural networks are often used to predict ice on the surface of wind turbine blades because of their high efficiency and prediction accuracy in image recognition task [40].

Kreutz et al. proposed in 2021, a convolutional neural network model with dual inputs and a one-dimensional convolutional filter to predict wind turbine blade icing in the next 24 hours using historical data from wind turbines as well as weather forecasts, and experimented with the model using data from three different wind farms, and the experimental results showed that the model had an average prediction accuracy of 97.9% [41]. Following this, in 2022, Cheng et al. suggested a Temporal Attention-based Convolutional Neural Network (TACNN). TACNN

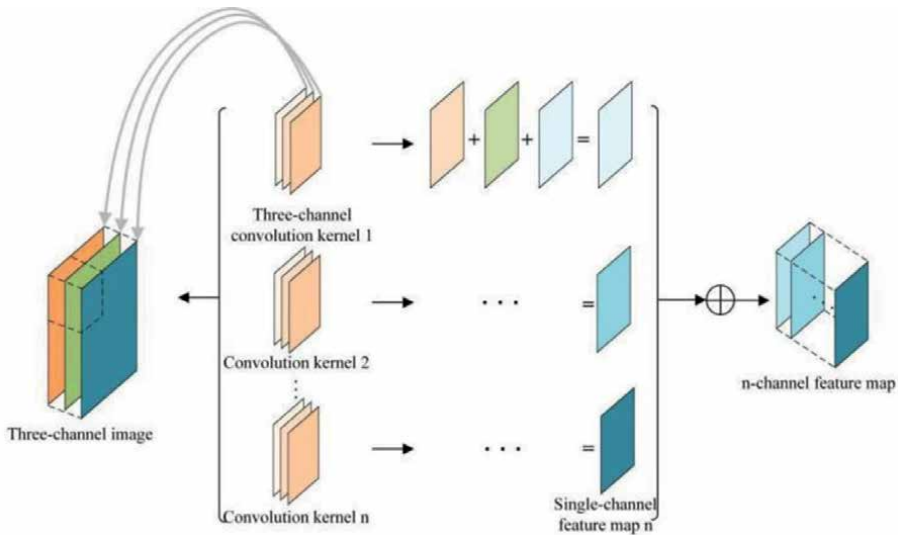


**Figure 6.**  
Principle of convolutional neural network computational model.

was compared to 10 different baseline networks in three data sets in a comparative experiment, and the experimental findings demonstrated that TACNN had considerable benefits over others [42]. In 2022, Xiao et al. combined convolutional neural network (CNN) with recurrent neural network (RNN), Long Short-Term Memory (LSTM), and gated recurrent unit (GRU) to build CNN, CNN-RNN, CNN-LSTM, and CNN-GRU and performed prediction comparison experiments, and the experimental results show that the proposed models outperform single deep learning models in prediction [43].

### 3.2 Recurrent neural networks

Elman et al. developed the recurrent neural network model in 1986, and recurrent neural network research has progressed greatly since then [23]. The Recurrent Neural Network (RNN) is a type of neural network capable of processing sequential data [44]. Its primary idea is to offer a recurrent structure that allows data to be sent from one-time step to the next. An RNN has an input layer ( $x$ ), a hidden layer ( $s$ ), an output layer ( $o$ ), and parameter matrices ( $u$ ,  $v$ , and  $w$ ), as shown in **Figure 7**. The connections between hidden layers in recurrent neural networks allow information from the previous instant to be maintained and passed on to the next instant. In the realm of wind turbine blade icing prediction, RNNs can estimate future wind turbine blade icing using input wind turbine historical temperature, humidity, wind speed, and other meteorological data. RNNs may also be used with other deep learning models, such as convolutional neural networks (CNNs), to improve the accuracy and efficiency of hybrid models for forecasting wind turbine blade icing [45, 46].

In 2022, Li et al. integrated the physical information of the underlying wind turbine system into a data-driven model, using the structural properties and linearized representation of the wind turbine system as physical constraints, and applied them to a Deep Residual Recurrent Neural Network (DR-RNN) to form a deep



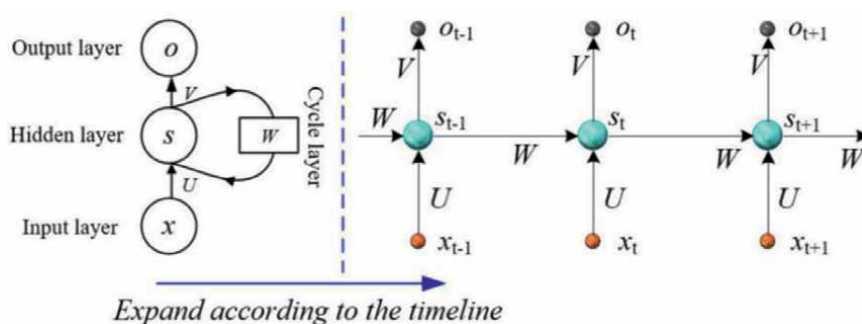


**Figure 7.**  
*Principle of recurrent neural network model.*

learning model based on physical information, as well as conducted experiments. The experimental findings demonstrate the model's accuracy and effectiveness [47]. In the year 2021, Tian et al. presented a Multilayer Convolutional Recurrent Neural Network (MCRNN). On the balanced dataset processed with the data resampling technique, the suggested MCRNN outperforms the ideal baseline by 38.8 and 42.9%, respectively, and by 23.9 and 30.6% on the unbalanced dataset processed with the MCRNN optimized with the equilibrium-like loss function. This model's broad application for icing prediction is demonstrated [48].

### 3.3 Deep neural networks

Deep Neural Network (DNN) research has improved greatly since Frank Rosenblatt's invention of the model in 1960 [49], and it is currently applied in a wide range of fields [50–53]. The computational model principle of this method is depicted in **Figures 8** and **9**. Deep Neural Networks (DNNs) show high accuracy and generalization capabilities in the prediction of wind turbine blade icing. They can predict icing occurrences by automatically learning characteristics and trends from massive amounts of data.

Li et al. proposed a universal DNN model for assessing prediction accuracy using pre-designed model performance indicators such as the reward function. The technique may relate continuously transmitted features to the binary state of turbine blade icing by using intermediate feature variables. Experiment findings suggest that the integrated metric system outperforms a single accuracy measure when assessing prediction models [54]. Cui et al. performed icing impeller model tests as well as natural world icing trials before recommending a deep neural network-based approach for predicting icing quality in 2022 [55]. In the trials, a mapping relationship between the rate of variation of the icing impeller's natural frequency and its mass was discovered, and the correlation coefficients were all greater than 0.93. The DNN prediction model of impeller icing quality uses the rate of change of the first six orders of natural frequency as one of its input components. The results showed that the MAE and MSE of the trained model were close to zero. For different impeller icing states, the DNN model's average prediction errors were 4.79, 9.35, 3.62, and 1.63% [55]. Using a DNN model, Jeong et al. predicted that freezing of wind turbine blades will occur in 2022. Along with meteorological data, the authors gathered field-based experimental data. The DNN model was created and trained to predict blade icing on wind turbines. The results showed that the DNN model had strong prediction ability

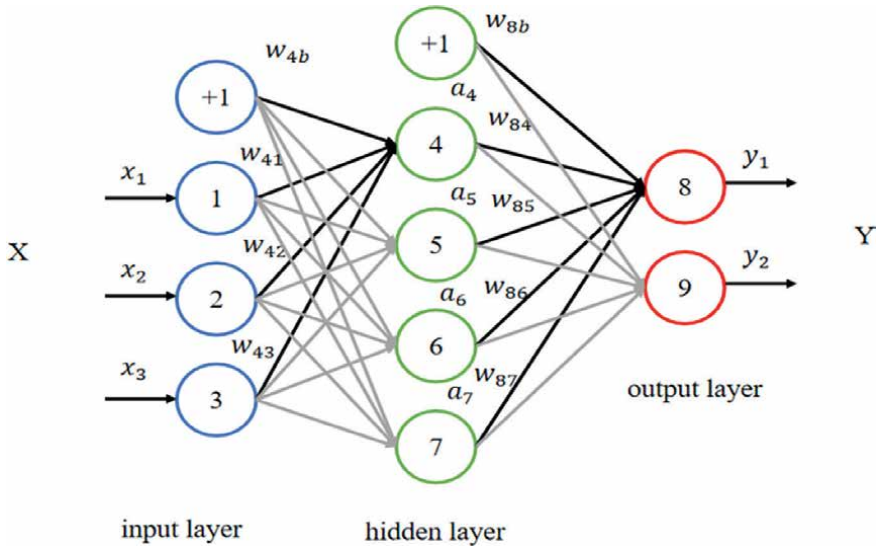


**Figure 8.** Schematic diagram of deep neural network model.

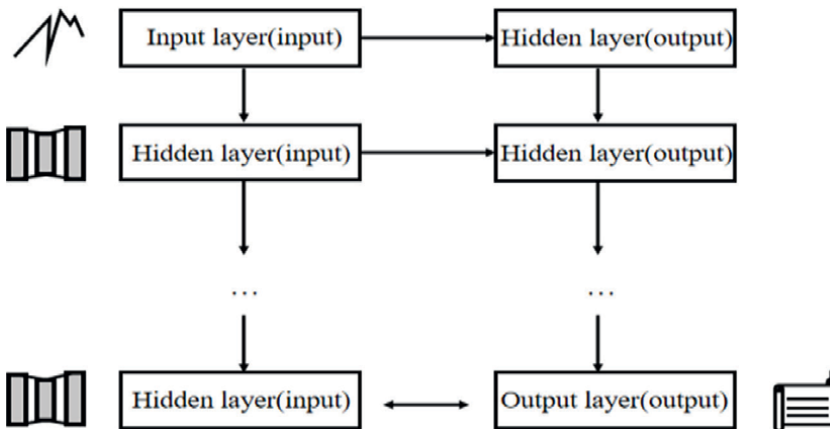


**Figure 9.** Deep neural network calculation principle diagram.

under a range of meteorological situations and could accurately anticipate wind turbine blade icing [56].

### 3.4 Stacked autoencoder

The Stacked Autoencoder (SAE) is a powerful deep learning model that automatically encodes data via unsupervised learning. In 2006 [35], Hinton and Salakhutdinov introduced the model, which employs numerous non-linear transformations to learn higher-order features of the input data [57]. A stacked autoencoder is composed of multiple autoencoders, each of which receives the output of the previous layer as input and trains on it. The main advantage of SAE is its capacity to autonomously extract significant features from data for supervised learning tasks without the need

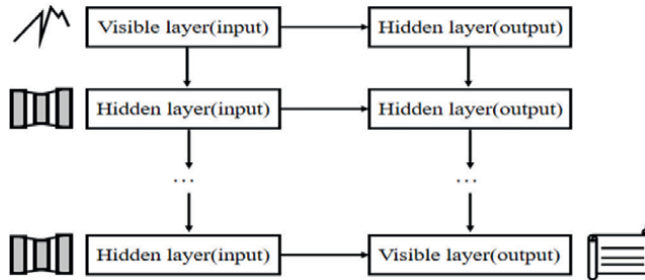


**Figure 10.**  
 Schematic diagram of stack self-coding calculation.

for labeled data. The computational model principle of this method is depicted in **Figure 10**. SAE is commonly used for feature extraction and data dimensionality reduction in wind turbine blade icing prediction [58].

In 2020, Lu et al. used stacked self-coding and Fisher Autoencoder (FAE) to extract discriminative wind turbine icing features, which were then input into a hybrid model that combined DFAE with Self-Organizing Map (DFAE-SOM), and the experiments revealed that the hybrid model is more efficient when data with discriminative features is input [59]. Yi et al. published a wind turbine icing data approach based on discriminative feature learning the same year. The approach constructs representations with SAE using normal operation data and time series information, combines original data, SAE-extracted features, and residual vectors for discriminative features, and performs feature selection and dimensionality reduction. The method’s practicality and superiority were demonstrated using a benchmark dataset [60].

### 3.5 Transfer learning

In 1995, Caruana pioneered transfer learning by developing the first transfer learning model. Transfer Learning (TL) is a machine learning technique that applies previously learned knowledge to a new task. Its central concept is to train and reason by transferring a learnt model from one domain to another related domain in order to improve the model’s generalization capacity and efficiency [61–63]. **Figure 11** shows how it works. Transfer learning may be used to forecast wind turbine icing utilizing current meteorological datasets (e.g., temperature, humidity, wind speed, precipitation, etc.) in the field of wind turbine ice prediction. Training time may be substantially decreased and prediction accuracy can be increased by pre-training a model on a large meteorological dataset and then transferring it to the wind turbine

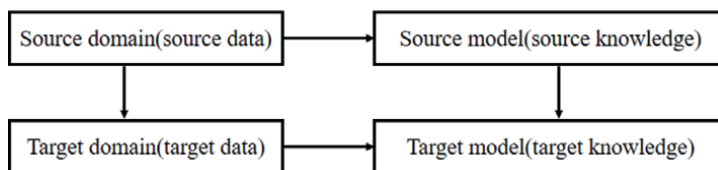


**Figure 11.**  
 Principle diagram of migration learning calculation.

icing prediction job. Transfer learning may also aid in the prediction of wind turbine ice in various areas or models.

In 2022, Li et al. published a generalized DNN-based model for predicting wind turbine icing situations that is based on data from SCADA systems and has a high combined accuracy [64]. Previously, in 2021, Chen et al. developed TrAdaBoost, a ground-breaking transfer learning algorithm that has been shown to increase performance in dealing with imbalances and varying distributions of wind turbine data [65].

In recent years, deep learning has been actively used and researched in the field of wind turbine blade icing prediction, with the objective of enhancing the operating efficiency and safety of wind generating systems. The most often used deep learning models nowadays include CNN, RNN, DNN, SAE, and TL. Each of these models has advantages and disadvantages, and the most appropriate model must be chosen depending on the unique circumstance in real-world applications [66–69].

#### **4. Conclusion**

Overall, the use of deep learning in the prediction of wind turbine blade icing has shown excellent results.

Convolutional Neural Networks (CNNs) are commonly employed in deep learning for extracting spatial information from time series data, allowing them to identify icing spots effectively. For accurate icing time estimates, Recurrent Neural Networks (RNNs) examine serial data and identify temporal correlations. Deep learning algorithms with context adaptation will become more important in wind turbine icing prediction. Future study will concentrate on increasing accuracy, lowering computing complexity, and tackling uncertainty. Furthermore, by incorporating multiple data sources for training and refinement in wind turbine blade icing prediction, federated learning will improve model stability and generalization.

Deep learning is increasingly being used to forecast wind turbine blade ice. As a result of the continuous development and application of machine learning, deep learning, data mining, physical modeling, and data-driven technologies, the performance and accuracy of wind turbine icing prediction methods have significantly improved, providing more effective support and guarantee to ensure the normal operation of wind turbines and promoting the sustainable development and promotion of wind energy.


## **Author details**

Lidong Zhang\*, Yimin Xu and Yuze Zhao  
Northeast Electric Power University, Jilin, China

\*Address all correspondence to: [lidongzhang@neepu.edu.cn](mailto:lidongzhang@neepu.edu.cn)

## **IntechOpen**

---

© 2023 The Author(s). Licensee IntechOpen. This chapter is distributed under the terms of the Creative Commons Attribution License (<http://creativecommons.org/licenses/by/3.0>), which permits unrestricted use, distribution, and reproduction in any medium, provided the original work is properly cited. 

## References

- [1] BP. Energy Outlook 2023 edition. Energy economics. [Internet] 2023 [cited 2023 Apr 1]. Available from: <https://www.bp.com/en/global/corporate/energy-economics/energy-outlook.html>
- [2] IEA. Electricity Market Report 2023 – Analysis. International Energy Agency. [Online]. Available from: <https://www.iea.org/reports/electricity-market-report-2023>. [Accessed: 10-Apr-2023]
- [3] Technical Research Centre of Finland (VTT). Cold climate wind energy showing huge potential. ScienceDaily. 2013. Available from: <https://www.sciencedaily.com/releases/2013/05/130528091611.htm> [Accessed 7 December, 2017]
- [4] Qiuyun M, Guoqiang W, Rongbin G. Wind turbine blade icing condition and anti-ice deicing measures. Science Technology and Engineering. 2022;22:09017-09008
- [5] Technical Research Centre of Finland (VTT). Cold climate wind energy showing huge potential [DB/OL]. ScienceDaily, 2013 [Accessed 18 December, 2021]. Available from: [www.sciencedaily.com/releases/2013/05/130528091611.htm](http://www.sciencedaily.com/releases/2013/05/130528091611.htm)
- [6] Contreras M, Leidy T. A review on the estimation of power loss due to icing in wind turbines. Energies. 2022;15:1083. DOI: 10.3390/en15031083
- [7] Tahir SAR, Virk MS. Vertical axis wind turbine operation in icing conditions: A review study. Wind Engineering. 2021;46:0309524X2110618. DOI: 10.1177/0309524X211061828
- [8] Clement H, Guy F, Jean P. Wind turbine performance under icing conditions. Wind Energy. 2008;11:319-333. DOI: 10.1002/we.258
- [9] Yirtici O, Ozgen S, Tuncer IH. Predictions of ice formations on wind turbine blades and power production losses due to icing. Wind Energy. 2019;22:909-923. DOI: 10.1002/we.2333
- [10] Shakirov VA, Fedyayev AA. Accounting for the impact of blade icing on wind energy production according to Weather Station data. In: 2020 International Multi-Conference on Industrial Engineering and Modern Technologies (FarEastCon) 06-09 October 2020. Vladivostok, Russia: IEEE; 2020
- [11] The 2021 power outage in Texas. Available from: <https://www.texasmonthly.com/news-politics/texas-blackout-preventable/>
- [12] Jesus Maria PP, Fausto Pedro GM, Diego RH. Economic viability analysis for icing blades detection in wind turbines. Journal of Cleaner Production. 2016;135:1150-1160. DOI: 10.1016/j.jclepro.2016.07.026
- [13] Matthew CH, Per JN, Per AS. Ice sensors for wind turbines. Cold Regions Science Technology. 2006;46:125-131. DOI: 10.1016/j.coldregions.2006.06.005
- [14] Jorge M, Sergio M, Estefanía A, Emilio G. Using SCADA data for wind turbine condition monitoring: A systematic literature review. Energies. 2020;13:3132. DOI: 10.3390/en13123132
- [15] Michał C, Robert B, Rafał K, Jörg K. Advances and practical applications of deep and shallow machine learning. Journal of Universal Computer Science. 2022;28:225-226. DOI: 10.3217/jucs-028-03-0225

- [16] Markus K, Abderrahim A, Kamaloddin V, Stephan O. Machine learning-based icing prediction on wind turbines. Elsevier. 2019;**81**:423-428. DOI: 10.1016/j.egypro.2019.03.073
- [17] Rumelhart DE, Hinton GE, Williams RJ. Learning internal representations by error propagation. *Nature*. 1986;**323**:533-536
- [18] BP neural network principle and algorithm derivation process. Available from: <https://blog.csdn.net/wu740027007/article/details/100884238>
- [19] Deep Learning -- the New Wave of machine Learning. Available from: <https://blog.csdn.net/datoubo/article/details/8577366>
- [20] Cheng P, Jing H, Hao C, Xinpan Y, Xiaojun D. Icing prediction of Fan blade based on a hybrid model. *International Journal of Performability Engineering*. 2019;**15**:2882-2890. DOI: 10.23940/ijpe.19.11
- [21] Feiyu L, Hongmei C, Hongjie S, Iderchuluun ZM, Yaxiong Z, Yong Z. Icing condition prediction of wind turbine blade by using artificial neural network based on modal frequency. *Cold Regions Science and Technology*. 2022;**194**:103467. DOI: 10.1016/j.coldregions.2021.103467
- [22] Isonguyo JI, James FW, Martin TB. Bilinear modelling, control and stability of directional drilling. *Control Engineering Practice*. 2019;**82**:161-172. DOI: 10.1016/j.conengprac.2018.10.008
- [23] Elman JL. Finding structure in time. *Cognitive Modeling. Cognitive Science*. 1990;**14**:179-211
- [24] Cheng P, Qing C, Xiaohong Z, Songsong W, Zhaohui T. Wind turbine blades icing failure prognosis based on balanced data and improved entropy. *International Journal of Sensor Networks*. 2020;**34**:126-135. DOI: 10.1504/ijnsnet.2020.110467
- [25] Ludmila IK. Combining pattern classifiers: Methods and algorithms: Second edition. *Technometrics. Technometrics*. 1st ed. Chichester: Wiley; 2014. p. 212-234. DOI: 10.1002/0471660264
- [26] Ensemble learning. Available from: [https://blog.csdn.net/xiao\\_yi\\_xiao/article/details/124040296](https://blog.csdn.net/xiao_yi_xiao/article/details/124040296)
- [27] Breiman L. Bagging predictors. *Machine Learning*. 1996;**24**:123-140. DOI: 10.1007/BF00058655
- [28] Tianqi C, Carlos G. XGBoost: A scalable tree boosting system. In: *Proceedings of the 22nd ACM SIGKDD International Conference on Knowledge Discovery and Data Mining*. New York, United States: IEEE; 13-17 August 2016. p. 785-794. DOI: 10.1145/2939672.2939785
- [29] Liwen W, Yanlong Z. Wind turbine blade icing fault prediction based on SCADA data by XGBoost. *Academic Journal of Engineering and Technology Science*. 2022;**5**:30-35. DOI: 10.25236/AJETS.2022.050206
- [30] Peng G, David I. Wind turbine blade icing detection with multi-model collaborative monitoring method. *Renewable Energy*. 2021;**179**:1098-1105. DOI: 10.1016/j.renene.2021.07.120
- [31] Wolpert DH. Stacked generalization. *Neural Networks*. 1992;**5**:241-259. DOI: 10.1016/S0893-6080(05)80023-1
- [32] Yuanyuan L, Lingyu H, Ming T. Prediction of wind turbine blades icing based on feature selection and 1D-CNN-SBiGRU. *Multimed Tools*

and Applications. 2022;**81**:4365-4385.  
DOI: 10.1007/s11042-021-11700-7

[33] Mendeleev SA, Mokhnachev SA. Bagging-based ensemble method for regression problems with low-dimensional data. *Journal of Computer and Systems Sciences International*. 2019;**58**:186-197. DOI: 10.1134/S1064230719020091

[34] Hongmin Z, Haiming N, Zenghui M, Shuyao Z. Wind turbine condition monitoring based on bagging ensemble strategy and KNN algorithm. *IEEE Access*. 2022;**10**:1. DOI: 10.1109/ACCESS.2022.3164717

[35] Hinton GE, Salakhutdinov RR. Reducing the dimensionality of data with neural networks. *Science*. 2006;**313**:504-507. DOI: 10.1126/science.1127647

[36] Hinton GE, Osindero S, Teh YW. A fast learning algorithm for deep belief nets. *Neural computation*. 2006;**18**:1527-1554. DOI: 10.1162/neco.2006.18.7.1527

[37] LeCun Y, Bengio Y, Hinton GE. Deep learning. *Nature*. 2015;**521**:436-444. DOI: 10.1038/nature14539

[38] Deep learning. Available from: [https://blog.csdn.net/qq\\_46458188/article/details/121594693](https://blog.csdn.net/qq_46458188/article/details/121594693)

[39] LeCun Y, Bottou L, Bengio Y, Haffner P. Gradient-based learning applied to document recognition. *Proceedings of the IEEE*. 1998;**86**:2278-2324. DOI: 10.1109/9780470544976.ch9

[40] Krizhevsky A, Sutskever I, Hinton GE. ImageNet classification with deep convolutional neural networks. *Communications of the ACM*. 2017;**60**:84-90. DOI: 10.1145/3065386

[41] Markus K, Abderrahim A, Kamaloddin V, Jan-Hendrik O, Michael L,

Michael F, et al. Convolutional neural network with dual inputs for time series ice prediction on rotor blades of wind turbines. *Procedia CIRP*. 2021;**104**:446-451. DOI: 10.1016/j.procir.2021.11.075

[42] Xu C, Fan S, Meng Z, Guoyang L, Houxiang Z, Shenyong C. Temporal attention convolutional neural network for estimation of icing probability on wind turbine blades. *IEEE Transactions on Industrial Electronics*. 2022;**69**:6371-6380. DOI: 10.1109/TIE.2021.3090702

[43] Jin X, Chunyan L, Bo L, Jing H, Ling X. Prediction of wind turbine blade icing fault based on selective deep ensemble model. *Knowledge-Based Systems*. 2022;**237**:108290. DOI: 10.1016/j.knosys.2022.108290

[44] Recurrent Neural Network. Available from: [https://blog.csdn.net/vendetta\\_gg/article/details/107213295](https://blog.csdn.net/vendetta_gg/article/details/107213295)

[45] Cho K, Van Merriënboer B, Gulcehre C, Bahdanau D, Bougares F, Schwenk H, et al. Learning phrase representations using RNN encoder-decoder for statistical machine translation. In: *Proceedings of the 2014 Conference on Empirical Methods in Natural Language Processing (EMNLP)*. 25-29 October 2014. Doha, Qatar: Association for Computational Linguistics; 2014. pp. 1724-1734

[46] RNN/LSTM/GRU. Available from: <https://zhuanlan.zhihu.com/p/123211148>

[47] Xuan L, Wei Z. Physics-informed deep learning model in wind turbine response prediction. *Renewable Energy*. 2022;**185**:932-944. DOI: 10.1016/j.renene.2021.12.058

[48] Weiwei T, Xu C, Guoyuan L, Fan S, Shenyong C, Hongxiang Z. A multilevel convolutional recurrent neural network for blade icing detection of wind turbine. *IEEE Sensors Journal*. 2021;**1**:1. DOI: 10.1109/JSEN.2021.3093726



- [49] Rosenblatt F. The perceptron: A probabilistic model for information storage and organization in the brain. *Psychological Review*. 1960;**65**:386-408. DOI: 10.1037/h0042519
- [50] Goodfellow I, Bengio Y, Courville A. *Deep Learning*. The MIT Press; 2016
- [51] Deep Neural Networks Available from: <https://blog.csdn.net/Yasin0/article/details/86167009>
- [52] Deep neural network DNN understanding. Available from: [https://blog.csdn.net/qq\\_54432917/article/details/127970677](https://blog.csdn.net/qq_54432917/article/details/127970677)
- [53] Wei T, Hao C, Xian D, Yibing L, Zhiyong M, Haihua M. DNN-based approach for fault detection in a direct drive wind turbine. *IET Renewable Power Generation*. 2018;**12**:1164-1171. DOI: 10.1049/iet-rpg.2017.0867
- [54] Tingshun L, Jiaohui X, Zesan L, Dadi W, Wen T. Detecting icing on the blades of a wind turbine using a deep neural network. *Computer Modeling In Engineering & Sciences*. 2023;**2**:767-782. DOI: 10.32604/cmescs.2022.020702
- [55] Hongmei C, Zhongyang L, Bingchuan S, Teng F, Yonghao L, Lida L, et al. A new ice quality prediction method of wind turbine impeller based on the deep neural network. *Energies*. 2022;**15**:8454. DOI: 10.3390/en15228454
- [56] Inho J, Haeseong C, Chankyu S, Taeseong K. Sustainable data-driven framework via transfer learning for icing-detection of high aspect ratio blades. *Cold Regions Science and Technology*. 2022;**201**:103606. DOI: 10.1016/j.coldregions.2022.103606
- [57] Schölkopf B, Platt J, Hofmann T. Greedy layer-wise training of deep networks. In: *Advances in Neural Information Processing Systems 19*: Proceedings of the 2006 Conference; 4-7 December 2006. Vancouver, Canada; 2007. pp. 153-160
- [58] Vincent P, Larochelle H, Jajoie I. Stacked denoising autoencoders: Learning useful representations in a deep network with a local denoising criterion. *Journal of Machine Learning Research*. 2010;**11**:3371-3408 ISSN: 1532-4435
- [59] Weipeng L, Xuefeng Y. Deep fisher autoencoder combined with self-organizing map for visual industrial process monitoring. *Journal of Manufacturing Systems*. 2020;**56**:241-251. DOI: 10.1016/j.jmsy.2020.05.005
- [60] Huaikuan Y, Qincho J. Discriminative feature learning for blade icing fault detection of wind turbine. *Measurement Science and Technology*. 2020;**31**:115015. DOI: 10.1088/1361-6501/ab9bb8
- [61] Riyad BR, Mark VA. Transfer learning: Leveraging trained models on novel tasks. In: Albert MV et al., editors. *Bridging Human Intelligence and Artificial Intelligence, Educational Communications and Technology: Issues and Innovations*. Switzerland AG: Springer Nature; 2022. pp. 47-58. DOI: 10.1007/978-3-030-84729-6\_4
- [62] Transfer learning. Available from: <https://blog.csdn.net/houshaolin/article/details/71077705/>
- [63] Mohammadreza I, Khaled R, Hamid Reza A. A Review of Deep Transfer Learning and Recent Advancements. *arXiv*. 2022. DOI: 10.48550/arXiv.2201.09679.
- [64] Tingshun L, Jiaohui X, Zesan L, Dadi W, Wen T. Detecting icing on the blades of a wind turbine using a deep neural network. *Computer Modeling in Engineering & Sciences*.

2022;**134**:767-782. DOI: 10.32604/  
cmes.2022.020702

[65] Wanqiu C, Yingning Q, Yanhui F, Ye L, Andrew K. Diagnosis of wind turbine faults with transfer learning algorithms. *Renewable Energy*. 2021;**163**:2053-2067. DOI: 10.1016/j.renene.2020.10.121

[66] Hacıfendioglu K, Basaga HB, Ayas S, Karimi MT. Automatic detection of icing wind turbine using deep learning method. *Wind and Structures*. 2022;**34**:511-523. DOI: 10.12989/was.2022.34.6.511

[67] Junqing M, Lixin M, Xincheng T. Wind turbine blade icing prediction based on deep belief network. In: 2019 4th International Conference on Mechanical, Control and Computer Engineering. 24-26 October 2019. Hohhot, China: IEEE; 2019. pp. 26-29

[68] Helbing G, Ritter M. Deep learning for fault detection in wind turbines. *Renewable & Sustainable Energy Reviews*. 2018;**98**:189-198. DOI: 10.1016/j.rser.2018.09.012

[69] Joyjit C, Nina D. Deep learning with knowledge transfer for explainable anomaly prediction in wind turbines. *Wind Energy*. 2020;**23**:1693-1710. DOI: 10.1002/we.2510

## Chapter 4

# Experimental Visualization of the Icing Process of Water Droplets on Cold Aluminum Plate Surface

*Yingwei Zhang, Yuxin Xu and Wenfeng Guo*

### Abstract

Ice accretion on the cold airfoil blade surface, such as wind turbines working in winter, affects its performance and degrades its aerodynamic characteristics and efficiency. Therefore, it is necessary to study the icing characteristics on the cold blade surface. At present, many pieces of research on wind turbine blade icing have been explored on the macroscale but seldom on the microscale. In this chapter, the icing process of a single water droplet on the cold aluminum plate surface was examined by a visualized method. The effects of volume and temperature on the icing characteristics were tested and acquired. After that, the profile parameters of iced water droplets were drawn and analyzed by MATLAB software, including the contact diameter, the maximum diameter and height of iced water droplets, the contact angle, and so on. The research findings provide experimental and theoretical foundations to deeply study the icing characteristics of wind turbine blades on a microscale.

**Keywords:** wind turbine, icing, water droplet, visual experiment, cold plate surface

### 1. Introduction

Fuel energy is an important basis related to human and economic development. However, the problems of non-renewability and pollution to the environment promote the rapid development of renewable energy worldwide. Wind energy, a type of renewable energy, has the characteristics of abundance, wide scope of distribution, and cleanness. It has been paid more attention by many countries. Wind turbine, a type of power generation equipment, is the main utilization in the field of wind energy. The total capacity of installation increases annually. According to the distribution of wind resources worldwide, high-quality wind resource is mainly located in high-altitude and high-latitude regions. In these regions, low temperature and humid environment exist. When the wind turbines work under this condition, ice accretion occurs on the blade surface. Then, the profile of the blade surface changes, and the dynamic characteristic of the blade degrades, decreasing the power efficiency of wind turbines [1, 2]. Therefore, it is necessary to explore the icing problem of wind turbines.

Currently, many scholars have studied the icing events of wind turbines, and the research methods include experiments and simulation. Yan Li simulated a quasi-3D ice model of a horizontal axial wind turbine using a 2D simulation method [3]. K. Pope simulated the ice shape on the airfoil S809 with FENSAP ICE software and obtained the load distribution law of the blade surface [4]. Zhaohui Du examined the growth process of ice on the leading edge of the NREL Phase VI blade using the simulation method. These research findings showed that the weight of ice increased along the wingspan. At the tip of the blade, the power efficiency decreased dramatically [5]. Fernando Villalpando explored the growth process of ice accretion on the 2D airfoil blade profile by combining FLUENT with MATLAB. In the aspect of the icing test, Yan Li conducted the ice distributions on the straight blade surface of a vertical axial wind turbine under low and high tip speed ratio conditions. The research findings validated that rotating velocity and relative angle of attack were key factors that affect the change of ice distribution [6, 7]. Additionally, Hu Hui also performed many tests of ice accretions on wind turbine blades. In assessing the power losses because of ice accretion, the field studies of research were performed in the wind farm based on the real horizontal axial wind turbine [8, 9]. Therefore, exploring the icing characteristics of wind turbines can provide theoretical and experimental foundations for developing de-icing technology for wind turbines. Nevertheless, in the previous research, scholars mainly focused on the macroscale ice shape and ice distribution on the blade surface, but the microscale ice process, such as water droplets, also needed to be researched and observed. In the microscale scope, the interactive relation between the iced water droplet and substrate can be explored and the icing mechanism be disclosed. It lays a research basis for developing de-icing technology for wind turbines. In the previous works, it was examined that there were four stages in the icing process, including supercooling of the droplet, nucleation, regrowing, and freezing and solid cooling [10]. By using visualization methods, it was found that there existed even nuclei in the water droplet at the moment of nucleation, and the water droplet changed from transparent to opaque. In the process of freezing, the interface between ice and water increased, and the profile of water droplets varied. Finally, a tip was generated on the top of the water droplet, and the iced water droplet exhibited a peach-like shape [11]. Zheyang Jin also performed a similar test based on the wind turbine icing problem [12]. In this research, scholars mainly explored the icing process and phenomena of water droplets on a cold surface, and the profile of water droplets is seldom analyzed parametrically. In this present study, not only the icing processes of water droplets were tested under different icing conditions, but the profiles of iced water droplets were also acquired and analyzed by image processing technology.

In this chapter, the icing process of a water droplet on a cold aluminum surface was studied based on the previous works. The low-temperature environment was simulated by a refrigerator. The icing process of water droplets was observed and acquired by a high-resolution industrial camera. The effects of the water droplet's volume and ambient temperature on the icing process and ice shape were tested. After that, image processing was conducted by MATLAB software, and the variations of profile, contacting area, and contact angle of water droplets were analyzed. Then, the regressions were performed and parametrically analyzed based on the image processing results. The research finding lays theoretical and experimental foundations for studying the icing characteristic and the adhesive characteristic of ice on the wind turbine blade surface.

## 2. Experimental system

### 2.1 Design of experimental system

The sketch map of the experimental system is shown in **Figure 1**. The system is composed of a refrigerating equipment, an experimental bench for icing, and an image acquisition system.

As shown in **Figure 1**, a refrigerator, BD/BC-305E model, is selected to simulate icing conditions. The temperature scope of the equipment is from 0 to  $-20^{\circ}\text{C}$ , and the resolution is  $1^{\circ}\text{C}$ . In this present study, the icing temperature was in the range of  $-5$  to  $-15^{\circ}\text{C}$ , satisfying the experimental condition. The experimental bench for the icing test is a high-precision mobile platform with XYZ directions. The maximum mobile range in each direction is 9 mm. An aluminum plate is fixed on the mobile platform, which is used to modulate the focal distance between the water droplet and the camera. The image acquisition and transaction system are comprised of a high magnification factor camera and a computer. The camera is used to capture the icing process of water droplets, and the computer is used to get the profile of iced water droplets and analyze the shape parameters. The experimental system is shown in **Figure 2**.

### 2.2 Image acquisition system

As shown in **Figure 1**, an image acquisition system is used to get the icing process of water droplets and conduct image processing. The system is comprised of a computer, a high magnification factor camera, and a supplementary light device. The camera is a type of CMOS camera having 16,000,000 pixels, and the frame rate of acquisition is 30 fps. The image resolution is  $1920 \times 1080$ , and the magnification factor is 100. The acquisition results are stored in the computer.

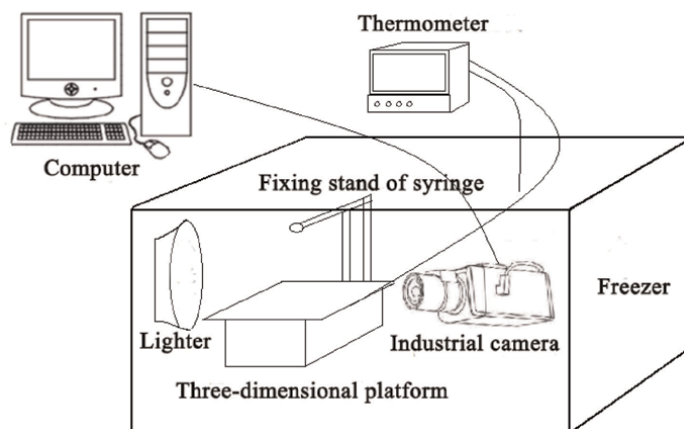


**Figure 1.**  
*Sketch map of the experimental system.*

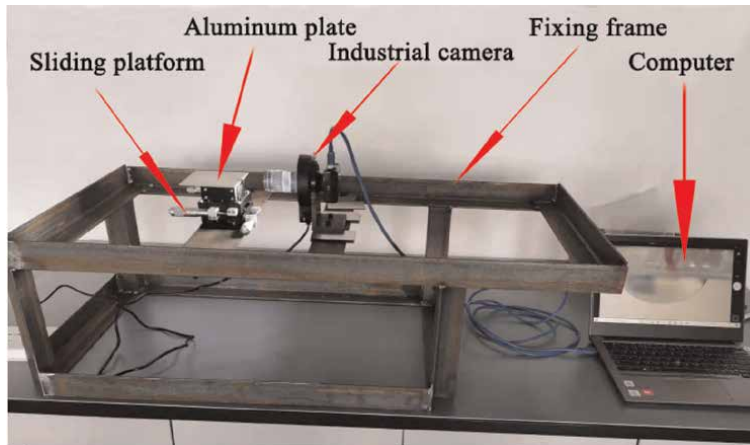


**Figure 2.**  
*Experimental system.*

### 3. Experiment

#### 3.1 Experimental scheme

In this present study, the experimental scheme is listed in **Table 1**.

As listed in **Table 1**, in this present study, the effects of water droplet volume and ambient temperature on the icing process and the shape of the iced water droplet are the key research content. Three kinds of water droplet volumes, including 30, 40, and 50  $\mu\text{L}$  and five kinds of temperatures, such as  $-10$ ,  $-12$ ,  $-14$ ,  $-16$ ,  $-18$ ,  $-20^\circ\text{C}$ , were selected. The experimental procedure is shown in **Figure 3**.

As shown in **Figure 3**, before testing, the experimental temperature was set, and the refrigeration system began to work. When the temperatures of the environment and aluminum plate surface reached the target temperature, the image acquisition system was started. Then, the icing test of the water droplet was performed. After that, the image acquisition and transaction were conducted.

#### 3.2 Image identification of iced water droplets

In this present study, automatic image processing technology was used to acquire the profile of iced water droplets, which is an innovative method. It was different from the manual processing method by using drawing software, such as AUTOCAD, Photoshop, and so on. Based on the procedure of image acquisition, the image analysis was performed using image processing technology developed in MATLAB, and the

Volume of water droplet ( $\mu\text{L}$ )	Temperature ( $^\circ\text{C}$ )
30	$-10$ , $-12$ , $-14$ , $-16$ , $-18$ , $-20$
40	$-10$ , $-12$ , $-14$ , $-16$ , $-18$ , $-20$
50	$-10$ , $-12$ , $-14$ , $-16$ , $-18$ , $-20$

**Table 1.**  
*Experimental scheme.*

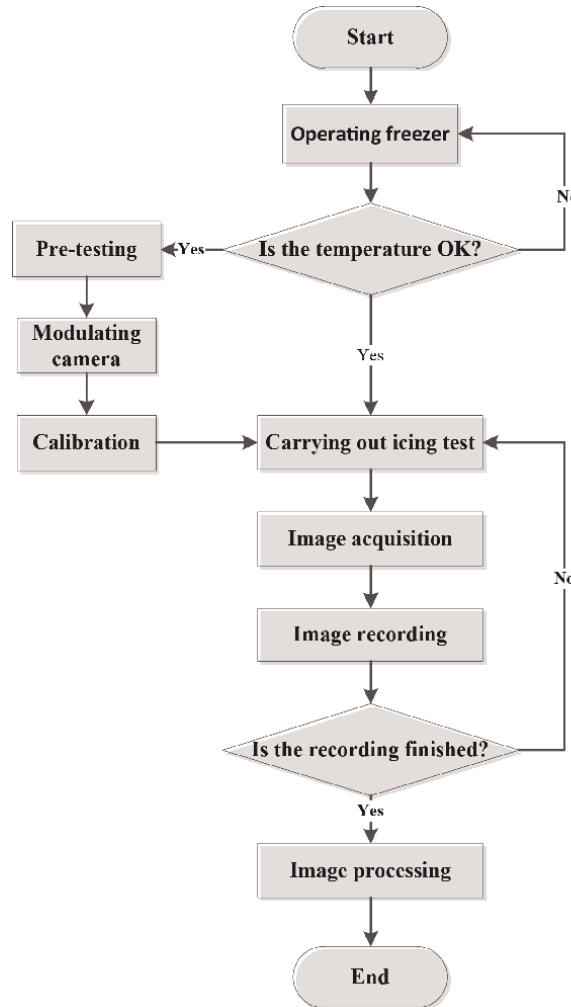


**Figure 3.**  
*Experimental procedure.*

profile of iced water droplets was obtained. Furthermore, the Gaussian filter in the Canny algorithm was replaced by the Wiener self-adaptive filter. In the icing process of water droplets, an image processing program can self-adapt to the variations of environmental brightness and transparency of water droplets in order to intensify the accuracy of identifying the profile of iced water droplets. Based on the image processing, a coordinate was set up and the profile of iced water droplets was regressed by a polynomial. The flowchart identifying the profile of the iced water droplet is shown in **Figure 4**.

As shown in **Figure 4**, the image processing system reads first the images from memory. Then, the colorful image is processed into a gray mode, which is used by the Canny algorithm in image processing [13]. Based on the gray image, the Wiener filter is applied to the image in self-adaption mode. The filter can self-adapt to local variation in the image, such as estimating the local average value and variation around each pixel, which are expressed in the following Eqs. (1) and (2).

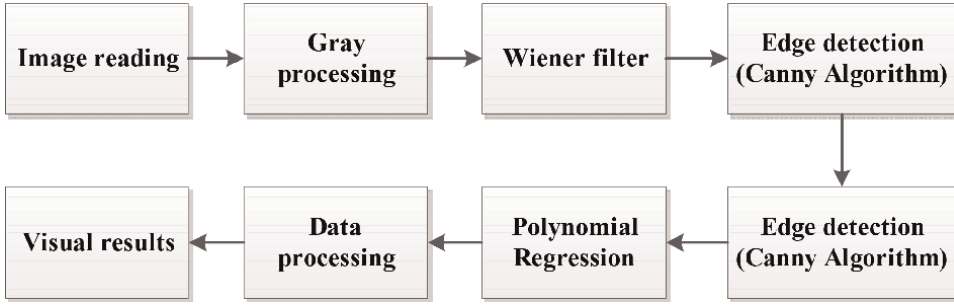


**Figure 4.**  
The flowchart identifies the profile of iced water droplets.

$$\mu = \frac{1}{NM} \sum_{n1, n2 \in \eta} a(n1, n2) \quad (1)$$

$$\sigma^2 = \frac{1}{NM} \sum_{n1, n2 \in \eta} a^2(n1, n2) - \mu^2, \quad (2)$$

where  $\eta$  is a local neighborhood in the range of  $N \times M$ ;  $\mu$  is the local average value around a pixel;  $N$  is the length of the local neighborhood;  $M$  is the width of the local neighborhood;  $a$  is the image matrix;  $\sigma^2$  is the local variation around a pixel;  $n1$  is the abscissa of image matrix; and  $n2$  is the ordinate of image matrix.

Based on Eqs. (1) and (2), the Wiener filter in the magnitude of pixel is set up by estimated value, which is expressed in Eq. (3).

$$b(n1, n2) = \mu + \frac{\sigma^2 - v^2}{\sigma^2} (a(n1, n2) - \mu), \quad (3)$$

where  $v^2$  is the variation of noise;  $b$  is the Wiener filter in the magnitude of pixel; and  $a$  is the local standard deviation around a pixel.

In image processing, the variation of noise cannot be predicted, so the average value of all the local variations was used in this present study. When the variation is high, the smoothing method is not used; conversely, the smoothing method is used when the variation is low [14, 15]. In this method, the processing result is better than the one processed by the linear filtering method. Therefore, the self-adaption filter is better than the linear filter in the aspect of processing the object profile. It can reserve the object edge and other parts with high frequencies in the image.

For the object edge in the image, the value can vary in different directions. Therefore, the classic Canny algorithm uses four gradient operators to calculate the gradients along the directions: horizontal, vertical, and diagonal. This kind of algorithm uses different operators of edges to calculate the modulus and direction which are expressed in Eqs. (4) and (5).

$$G = \sqrt{G_x^2 + G_y^2} \quad (4)$$

$$\theta = \text{atan2}(G_y, G_x), \quad (5)$$

where  $G$  is the gradient;  $G_x$  is the difference along the horizontal direction;  $G_y$  is the difference along the vertical direction;  $\theta$  is the included angle between the differences in the horizontal and vertical.



In the image gray processing, there exists a concentration region for gray variation. It needs to perform non-maximum suppression for gradient results and detect object edges. Then, the local maximum value needs to be found by comparing the gradient values along the gradient direction. After that, the maximum value is reserved, and the object edge with multiple pixels is changed into the one with a single pixel, making the width decrease.

In the border edge detection algorithm, a threshold value is commonly used to filter noise or variation of color, which results in a low gradient value. In the Canny algorithm, two threshold values, the high one and the low one, are selected to distinguish the edge pixel. When the gradient value is higher than the high threshold value, the pixel is marked as a strong edge pixel. Conversely, when the gradient value is lower than the low threshold value, the pixel is depressed. However, the pixel with a strong edge value can be considered as the real border, and the one with a weak edge value can be considered as noise or inference caused by color variation. Commonly, the pixel with a weak value caused by a real border is connected with the one with a strong value, but the one caused by noise is isolated. Based on this characteristic, the delay edge following algorithm is selected in this present study, which detects eight domains connected with a pixel having a weak edge value. In these connected domains, if there exist pixels with strong-edge values, these pixels will be reserved. In this algorithm, all the connected borders with weak-edge values are detected. If there exists a pixel in the weak border connecting with a pixel in the strong border, then the weak border is reserved; otherwise, it is depressed. The breadth-first search and depth-first search detection methods are used in this present study [16, 17].

Based on the border detection, it also needs to carry out morphology closing to deal with the problem of leaking edge. First, image dilation and erosion are conducted to connect the tiny breakpoints and delete the small remnant regions. Then, the image of iced water droplets was transformed into a binary image of an edge with a single connected domain. In this case, the coordinates of pixels with non-zero values in binary images are all obtained, and the tip of the iced water droplet is detected. According to the coordinate values, the origin of the coordinate is established at the tip of iced water droplets. For an iced water droplet, it has an axially symmetric profile. Therefore, the x-axis of the established coordinate has coincided with the symmetry axis of the profile, and the y-axis is vertical to the x-axis in this present study [18]. In the established coordinate system, the curved profile of iced water droplets is expressed by a polynomial fitting equation, which is expressed as Eq. (6).

$$p(x) = p_1x^n + p_2x^{n-1} + \dots + p_nx + p_{n+1}, \quad (6)$$

where  $n$  is the highest power in the polynomial and  $p_i$  is the coefficient in the polynomial.

Based on the polynomial fitting result in the profile of iced water droplets, the ratio of pixel number in the image to the real size of the object should be established, which is expressed by Eq. (7).

$$\mu = \frac{l}{n}, \quad (7)$$

where  $\mu$  is the ratio of pixel number to real size of the object;  $l$  is the real size of the object; and  $n$  is the pixel number in the image.

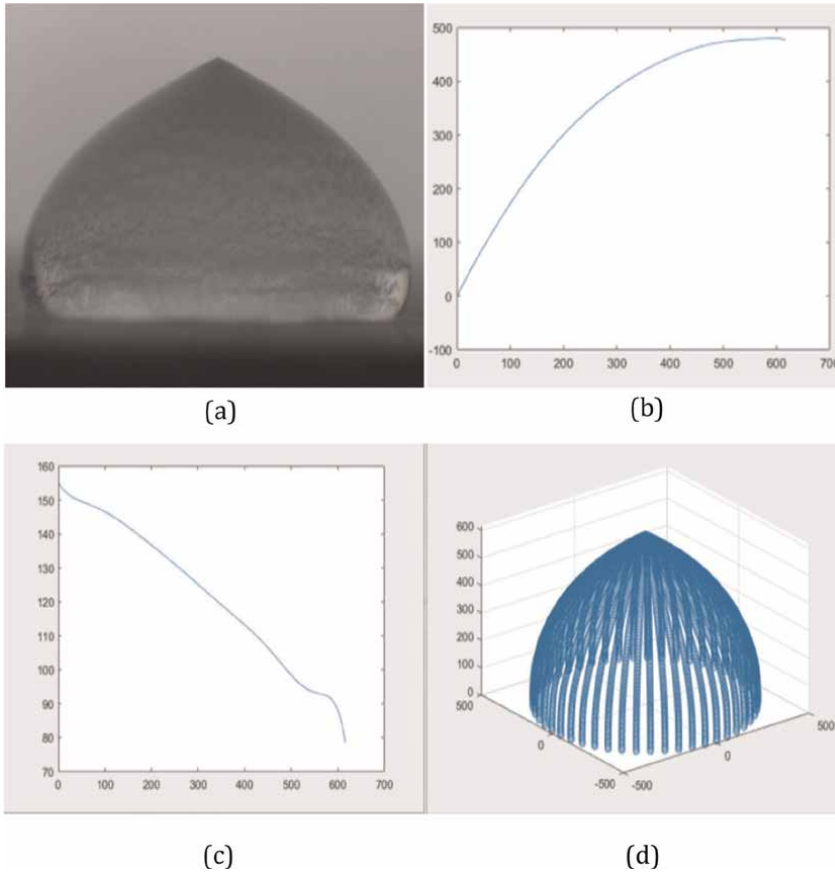


**Figure 5.**  
*Profile of iced water droplets.*

Combining image processing with profile identification, the profile of iced water droplets can finally be shown in **Figure 5**. As shown in **Figure 5a**, it shows the image of iced water droplets. **Figure 5b** shows a half profile of iced water droplets in **Figure 5a** after rotating the iced water droplet anticlockwise. From this figure, the symmetric axis of iced water droplets is located at the x-axis of the coordinate, and the upper half profile is obtained by the polynomial method. **Figure 5c** shows the variation of the included angle between the tangent line of the iced water droplet profile and the substrate plane. The value of the y-axis is the included angle, and the value of the x-axis is the position along the profile of iced water droplets. **Figure 5d** shows the 3D profile of iced water droplets generated from the 2D profile in **Figure 5b**.

## 4. Experimental results

### 4.1 Icing process of the water droplet

According to the experimental scheme in **Table 1**, three kinds of water droplet volumes and six kinds of temperatures were selected in the icing tests. The process of icing is shown in **Figure 6**.

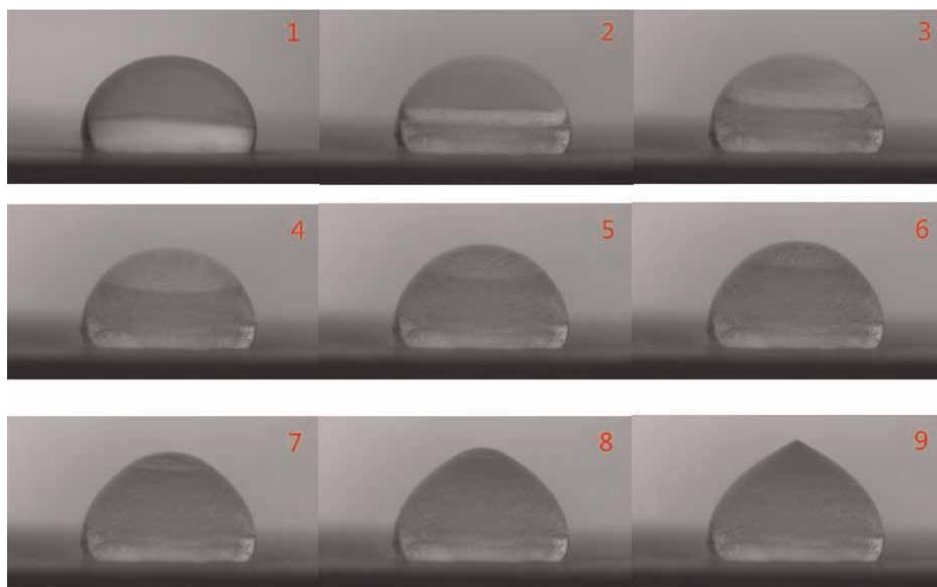


**Figure 6.**  
*Icing process of water droplets.*

**Figure 6** shows the icing process of a droplet of water with a volume of  $40\ \mu\text{L}$  under  $-15^\circ\text{C}$  conditions. The icing time for a droplet of water is 41 s from contacting the cold surface to freezing fully. The time interval between the two pictures is the same. As shown in the figure, the water droplet was transparent when contacting the cold surface initially. After fully freezing, it became opaque. At the initial stage of icing, the interface between ice and water was nearly parallel to the substrate surface. With the development of the icing process, the interface changed from plane to curve. The experimental results show that the icing time in the outer region of the water droplet, being close to the water surface, is shorter than the one in the inner region of the water droplet. The reason for this result is that heat transfer in the outer region of the water droplet happened not only between the water droplet and substrate but also between the water droplet and environmental air. In this instance, the water in the surface region froze faster than the one in the inner region. Additionally, at the initial stage of the icing process, the shape of water droplets did not change significantly; it was kept in the shape of a spherical cap, as shown from Picture 1 to Picture 5 in **Figure 6**. However, at the later stage of the icing process, the top of the water droplet presented a convex shape, looking like a tower tip at last. The reason for this result is that the surface of the water droplet is almost frozen at the end of the icing process, but the inner water has not fully frozen. In this instance, the frozen surface constrained the volume inflation of inner water in the icing process, which squeezed the water from the inner region to the tip surface. Finally, the tip surface of the water droplet became a sharp shape. Similarly, for other volumes of water droplets, the icing processes had the same phenomena.

#### 4.2 Effect of substrate temperature on the shape of iced water droplets

Based on the icing test of the water droplet, the profile of iced water droplets was acquired using the Canny algorithm and fitted using the polynomial equation. The profile of iced water droplets with a volume of  $40\ \mu\text{L}$  is shown in **Figure 7**.

Figure 7 shows the profiles under different ambient temperatures, including  $-10$ ,  $-12$ ,  $-14$ ,  $-16$ ,  $-18$ , and  $-20^{\circ}\text{C}$ . When the ambient temperatures are different, the shapes of iced water droplets are significantly different, such as the height, diameter, contact angle, and so on.

According to the fitting results of profiles, in quantitatively analyzing the variations of profile parameters with substrate temperature, four parameters including the contact angle of iced water droplets, contact diameter between the iced water droplet and substrate, and the maximum height and diameter of iced water droplets were selected in this present study. The variations of these parameters with substrate temperature are shown in Figure 8.

Figure 8a shows the variations in contact angle and diameter of an iced water droplet with ambient temperature. When the volume of the water droplet was constant, the contact diameter increased along with the substrate temperature, and the

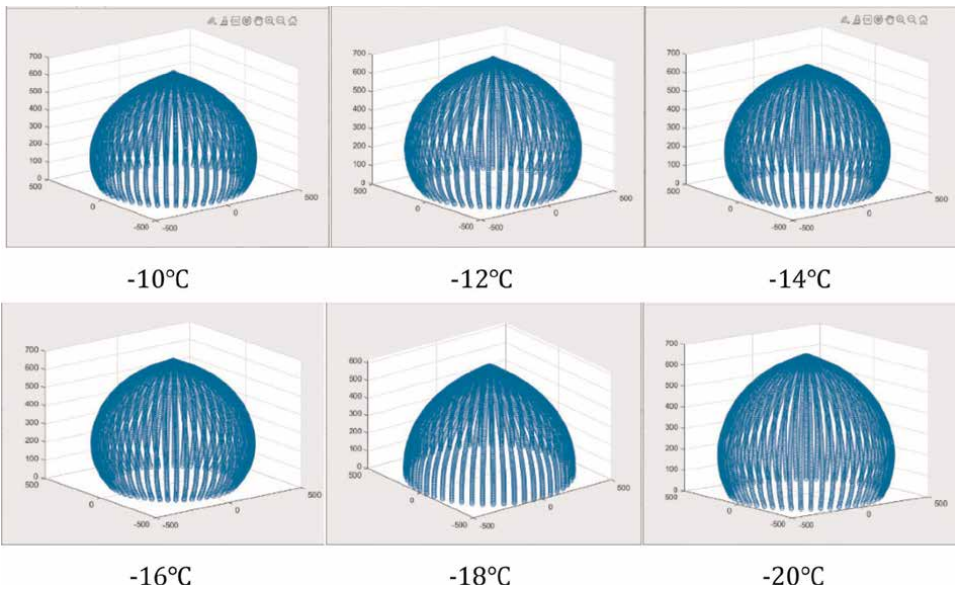


Figure 7. Profile of the iced water droplet with a volume of  $40\ \mu\text{L}$  fitted by polynomial.

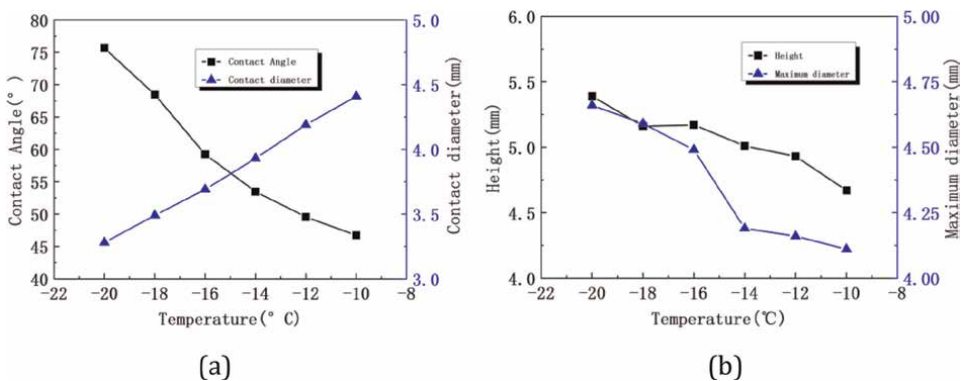


Figure 8. Variations of contact angle and contact diameter along with temperature.

contact angle decreased with the increase in the substrate temperature. The reason for these results is that the temperature difference between the water droplet and substrate increases as the substrate temperature decreases. In this instance, the heat quantity increases in unit time, and the icing time shortens. Additionally, the characteristic of water flowability degrades as the temperature decreases, which results in a decrease in the contact diameter and an increase in the contact angle. For this reason, the adhesive strength of iced water droplets decreases. The research finding indicates that impacting ice generated by water droplets impinging on the cold surface, such as wind turbine icing and aircraft icing, has low adhesive strength in comparison with glaze ice frozen by liquid water.

As shown in **Figure 8b**, the height of iced water droplets increases, and the maximum diameter of it decreases along with the substrate temperature. The reason for this result is the same as the above one. When the substrate temperature decreases, the icing time of water droplets shortens and the flowability of water degrades. However, the volume of water droplets is constant, which results in an increase in the height and a decrease in the maximum diameter of iced water droplets.

#### 4.3 Effect of water volume on the shape of iced water droplets

Similarly, the profiles of iced water droplets with volumes of 30, 40, and 50  $\mu\text{L}$  were also fitted by the Canny algorithm under the substrate of temperature of  $-16^\circ\text{C}$ . The fitting results are shown in **Figure 9**.

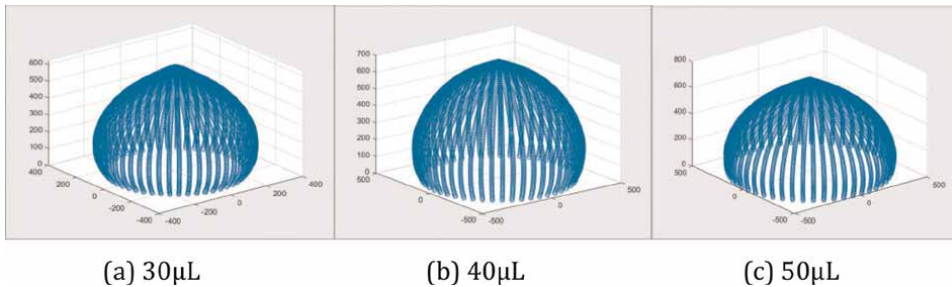


**Figure 9.**  
 Fitting profile of iced water droplets with volumes of 30, 40, and 50  $\mu\text{L}$ .

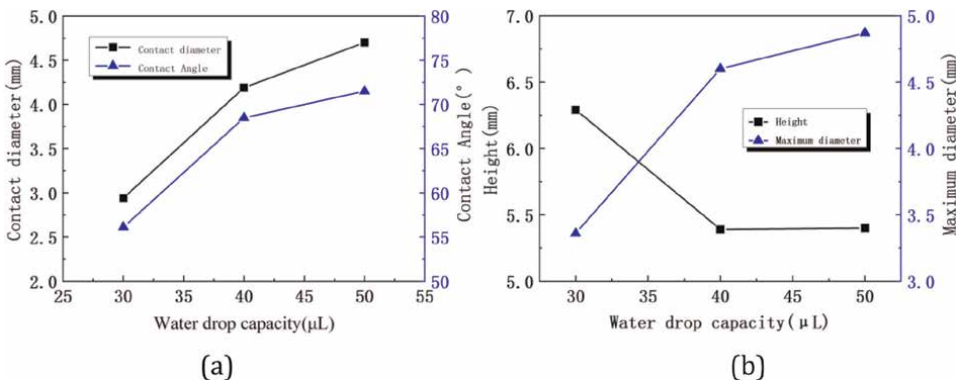


**Figure 10.**  
 Variation of profile parameter with water droplet volume.

As shown in **Figure 9**, when the substrate temperature was constant, the profiles of iced water droplets with different volumes were significantly different. Based on the results of image identification, the profile parameters of iced water droplets were analyzed comparatively with variations of water droplet volume, which are shown in **Figure 10**.

As shown in **Figure 10a**, when the substrate temperature is constant, the contact angle and the contact diameter of iced water droplets increase along with the water droplet volume. In **Figure 10b**, the maximum diameter of iced water droplets increases along with the water droplet volume, but the height decreases a little.

## **5. Conclusions**

In exploring the problem of wind turbine icing under a microscope, the icing process of water droplet on the cold aluminum plate surface was explored, and some conclusions are listed as follows:

1. An experimental system for icing tests was designed and built. The ambient temperature scope in the system is in the range of 0 to  $-20^{\circ}\text{C}$ . The icing process of water droplets was acquired by an industrial camera with a high magnification factor of 100. In enhancing the effectiveness and accuracy of image processing, automatic edge detection technology was used in this present study. Based on the MATLAB software, the profile of iced water droplets was identified and acquired using the Canny algorithm. In this way, the contact angle of water droplets was obtained, and the profile function was fitted using the polynomial equation.
2. The effects of water droplet's volume and substrate temperature on the profile and contact angle of iced water droplets were analyzed based on the image processing. When the substrate temperature was constant, both contact angle and contact diameter between the iced water droplet and substrate surface increased along with the water droplet volume. In contrast, when the water droplet volume was constant, the contact angle increased with the decrease in the substrate temperature, but the contact diameter decreased.

## **Acknowledgements**

This work was supported by the National Natural Science Foundation of China (NSFC) [grant number 51976029].


## **Author details**

Yingwei Zhang\*, Yuxin Xu and Wenfeng Guo  
Northeast Agricultural University, College of Engineering, Harbin, China

\*Address all correspondence to: [zhangyingweineau@163.com](mailto:zhangyingweineau@163.com)

## **IntechOpen**

---

© 2023 The Author(s). Licensee IntechOpen. This chapter is distributed under the terms of the Creative Commons Attribution License (<http://creativecommons.org/licenses/by/3.0>), which permits unrestricted use, distribution, and reproduction in any medium, provided the original work is properly cited. 

## References

- [1] Zhongqiu M, Wenfeng G, Yan L, Kotaro T. Wind tunnel test of ice accretion on blade airfoil for wind turbine under offshore atmospheric condition. *Renewable Energy*. 2023;**209**: 42-52. DOI: 10.1016/j.renene.2023.03.126
- [2] Xiangyu Y, Bai X, Huiqing C. Influence analysis of rime icing on aerodynamic performance and output power of offshore floating wind turbine. *Ocean Engineering*. 2022;**258**:111725. DOI: 10.1016/j.oceaneng.2022.111725
- [3] Li Y, Wang S, Sun C, et al. Icing distribution of rotating blade of horizontal axis wind turbine based on quasi-3D numerical simulation. *Thermal Science*. 2018;**22**(2):1191-1201. DOI: 10.2298/TSCI170821053L
- [4] Ibrahim GM, Pope K, Muzychka YS. Effects of blade design on ice accretion for horizontal axis wind turbines. *Journal of Wind Engineering & Industrial Aerodynamics*. 2018;**173**:39-52. DOI: 10.1016/j.jweia.2017.11.024
- [5] Liangquan H, Xiaocheng Z, Jing C, Shen Xin D, Zhaohui. Numerical simulation of rime ice on NREL phase VI blade. *Journal of Wind Engineering and Industrial Aerodynamics*. 2018;**178**: 57-68. DOI: 10.1016/j.jweia.2018.05.007
- [6] Yan L, Shaolong W, Qindong L, Fang F, Kotaro T. Characteristics of ice accretions on blade of the straight-bladed vertical axis wind turbine rotating at low tip speed ratio. *Cold Regions Science and Technology*. 2018; **145**:1-13. DOI: 10.1016/j.coldregions.2017.09.001
- [7] Guo W, Shen H, Li Y, Fang F, Kotaro T. Wind tunnel tests of the rime icing characteristics of a straight-bladed vertical axis wind turbine. *Renewable Energy*. 2021;**179**:116-132. DOI: 10.1016/j.renene.2021.07.033
- [8] Linyue G, Tao LY, Hui H. A field study of ice accretion and its effects on the power production of utility-scale wind turbines. *Renewable Energy*. 2021; **167**:917-928. DOI: 10.1016/j.renene.2020.12.014
- [9] Gao Linyue H, Hui. Wind turbine icing characteristics and icing-induced power losses to utility-scale wind turbines. *Proceedings of the National Academy of Sciences of the United States of America*. 2021;**118**(42): e2111461118. DOI: 10.1073/pnas.2111461118
- [10] Shurong G, Jiabin J, Bojian W, Xiaodong W. Research progress and future prospects of anti-/de-icing technology for droplets impact on hydrophobic/superhydrophobic surfaces. *CIESC Journal*. 2021;**72**(8): 3946-3957. (In Chinese)
- [11] Zhang X, Liu X, Min J, Xiaomin W. Shape variation and unique tip formation of a sessile water droplet during freezing. *Applied Thermal Engineering*. 2019;**147**:927-934. DOI: 10.1016/j.applthermaleng.2018.09.040
- [12] Yao X, Jiajun J, Yang Z, Yi X, Jin Z. Impingement and freezing of a supercooled large droplet on an ice surface. *Physics of Fluids*. 2022;**33**(10): 103304. DOI: 10.1063/5.0069596
- [13] Sangeetha D, Deepa P. FPGA implementation of cost-effective robust canny edge detection algorithm. *Journal of Real-Time Image Processing*. 2019; **16**(4):957-ss970. DOI: 10.1007/s11554-016-0582-2



[14] Haralick RM, Shapiro LG. Computer and Robot Vision. Vol. 1. Upper Saddle River, New Jersey: Addison-Wesley; 1992

[15] Kong TY, Rosenfeld A. Topological Algorithms for Digital Image Processing. Amsterdam: Elsevier Science; 1996

[16] Lam L, Lee S-W, Suen CY. Thinning methodologies—a comprehensive survey. IEEE Transactions on Pattern Analysis and Machine Intelligence. 1992;**14**: 869-885. DOI: 10.1109/34.161346

[17] Lijuan R, Xionghui W, Nina W, Guangpeng Z, Yongchang L, Zhijian Y. An edge thinning algorithm based on newly defined single-pixel edge patterns. IET Image Processing. 2023;**17**(4): 1161-1169. DOI: 10.1049/ipr2.12703

[18] Satoh I, Fushinobu K, Hashimoto Y. Freezing of a water droplet due to evaporation—Heat transfer dominating the evaporation freezing phenomena and the effect of Boilingon freezing characteristics. International Journal of Refrigeration. 2002;**25**(2):226-234



# A Brief Review of Blade Surface Icing Adhesive Theories for Wind Turbines

*He Shen and Yan Li*

## Abstract

In cold and humid areas, ice easily accumulates on the blade surface of the wind turbine. The icing on the blade surface causes the power efficiency of wind turbines to decline, even leading to safety accidents. In order to research and develop efficient anti-icing and de-icing technologies, exploring the adhesive properties between ice and the blade surface is necessary. Therefore, in this paper, the main theories of the icing adhesive mechanism have been briefly summarized, including mechanical, electronic, and wetting theories, from the aspects of theory and experimental research, which can provide a reference for researching icing mechanisms and the development of anti-icing and de-icing technologies for wind turbines.

**Keywords:** wind energy, wind turbine, blade airfoil, icing, adhesive theory

## 1. Introduction

Wind energy is one of the renewable energies of the best successful commercial operation. However, ice easily accumulates on the blade surface in cold and humid areas. An icing example of the wind turbine operating in Northeast China is shown in **Figure 1**. Icing affects the output power and the safe operation of wind turbines, causing severe economic loss and security risks to the power grid [1, 2]. Therefore, to research and develop efficient anti-icing and de-icing systems, the icing mechanism must be explored [3, 4].

The icing research of wind turbine mainly draws lessons from that of aircraft, including aerodynamics and heat transfer theory, etc. As is shown in **Figure 2**, the supercooled droplets impact the blade's surface following air movement [5]. The energy exchange occurs among droplets, blades, and flow field. The droplets freeze into ice in the phase transition and accumulate on the blade surface. This process can be obtained by numerical simulation or icing test [6]. However, there is a problem in the icing process needing to go a step further to explore, which is the icing mechanism. Therefore, in this chapter, some literature has been consulted, the significant theories of the icing mechanism have been briefly summarized, which can provide a reference for researching icing mechanisms and the development of anti-icing and de-icing technologies for wind turbines.



**Figure 1.**  
*An example of icing on wind turbines.*

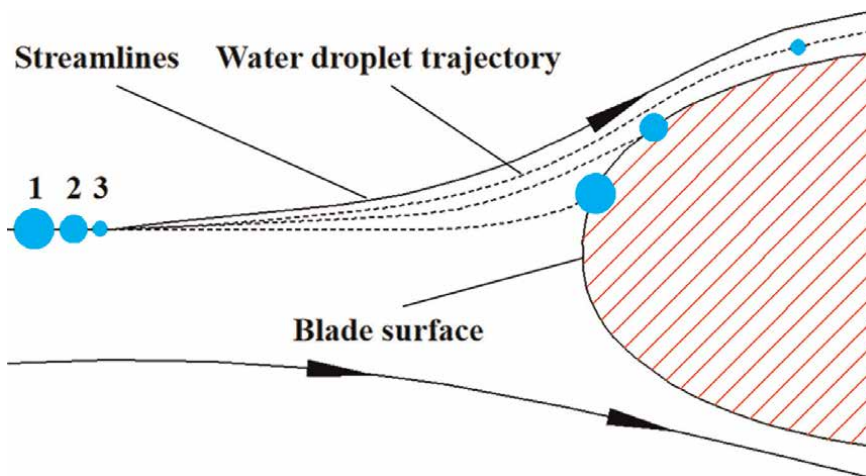


**Figure 2.**  
*Schematic diagram of water droplets impacting a blade [5].*

## 2. Overview of adhesion theories

Adhesion is a complex phenomenon related to the interaction of physics and chemistry from microscale to macroscale [7]. According to the research of Schultz and Nardin, the main adhesion theories are listed as follows: mechanical interlocking, electronic or electrostatic theory, adsorption (thermodynamic) or wetting theory, diffusion theory, chemical (covalent) bonding theory, and theory of weak boundary layers and interphases [8]. In contrast, Fourche [9] separated mechanical adhesion from specific adhesion, the latter including the subcategories of the electronic model, diffusion model, thermodynamic adsorption or wetting model, rheological model, chemical adhesion model, and the model of weak boundary layers. Although the classification and naming of Schultz and Fourche differ, their depiction of the main theories is similar. This chapter considered that mechanical theory and other adhesion theories explain the adhesive properties from different angles. The decision to separate mechanical theory from other adhesion theories is arbitrary. Therefore, this chapter uses the classification method of Schultz and Nardin to discuss adhesion theories.

At present, adhesion theories are applied to the research of icing mechanisms, mainly including mechanical, electronic, and wetting theories. The following part of this chapter will focus on mechanical, electronic, and wetting theories. The mechanical theory holds that adhesion results from mechanical interlocking between ice and the microscopic feature of the substrate surface. According to electronic theory, adhesion is generated by the double electron layer on the interface between ice and substrate surface. The wetting theory argues that the adhesion between the ice and the substrate surface depends on the wettability of the substrate surface [7, 8]. The above theories are not mutually exclusive. In the icing process, those mechanisms may occur simultaneously, depending on the specific conditions.

## 3. Mechanical theory

The mechanical theory is one of the oldest theories. In 1925, McBain and Hopkins first proposed the concept of “mechanical adhesive” in “On adhesive and adhesive action.” [8]. The mechanical theory holds that the substrate surface is uneven. On the microscale, the surface topography of substrate is similar to that of terrain. Many peaks and valleys of different shapes are randomly distributed on the substrate surface. When water freezes on the substrate surface, the peaks and valleys are like tiny dowels to bond the ice with the substrate. The schematic diagram of the mechanical adhesive mechanism is shown in **Figure 3** [9].

According to mechanical theory, the substrate surface is rougher, the ice adhesion strength is stronger. However, the mechanical theory does not consider the wettability of the substrate surface. The above assumption is valid under the premise of complete wetting of the substrate surface, as shown in **Figure 3a**. Conversely, there will exist many defects on the interface between ice and substrate, as shown in **Figure 3b**.

For mechanical theory, scholars such as Fortin, Knuth, and Shen explored the icing mechanism. In addition, some scholars, such as Chaudhury and Kim [10], have studied the elastic modulus, which is an important parameter affecting ice adhesive strength. The model of Fortin and Perron [11] is established based on the behavior of water before and after freezing, substrate roughness, and the type of ice. The model assumes that the ice near the freezing point is affected by internal and external strain, and its cohesive strength corresponds to the failure stress. The failure stress is related

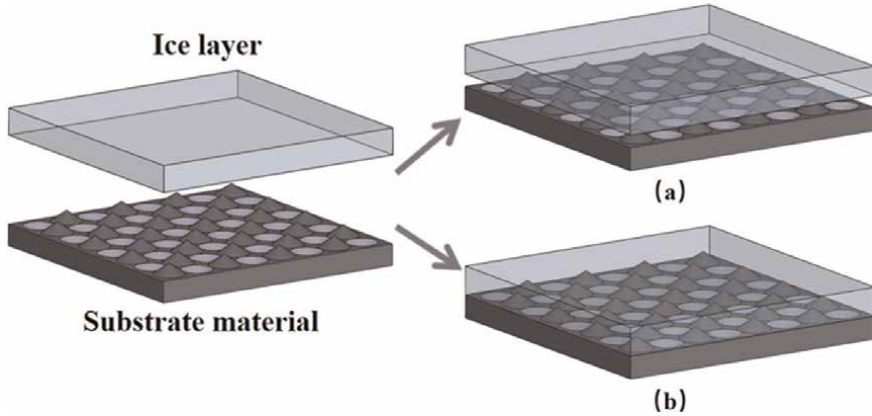


**Figure 3.** The schematic diagram of the mechanical adhesive mechanism. (a) Complete wetting state. (b) Incomplete wetting state [9].

to the grain size and creep of grain boundary sliding in polycrystalline substrates at elevated temperatures. The ice adhesion shear stress on the substrate with only a single level of roughness is expressed as Eq. (1) [11].

$$\tau_{adh} = \left\{ \alpha_{ice} \left( \frac{\chi_{oxygen} - \chi_{coating}}{\chi_{oxygen} - \chi_{substrate}} \right)^2 \frac{T_f - T}{T_f - T_{ref}} \frac{4\gamma_{LV}}{\delta_0} \right\} f_{por} \quad (1)$$

$$\times \left[ f_{RMS} + \frac{\delta_0}{\kappa} (1 - f_{RMS}) (1 - f_{cramp}) \right] + (1 - f_{RMS}) f_{cramp} \tau_f$$

Where  $\alpha_{ice}$  is the proportionality constant due to phase change;  $\chi$  is electronegativity;  $T$  is temperature;  $T_f$  is solidification temperature;  $T_{ref}$  is reference temperature;  $\gamma$  is surface tension;  $L$  is liquid;  $V$  is vapor;  $\delta_0$  is a molecular distance;  $f_{RMS}$  is the fraction of ice in contact with the substrate;  $\kappa$  is root mean square roughness height;  $f_{cramp}$  is fraction of mechanical locking;  $\tau_f$  is Ice shear strength;  $f_{por}$  is porosity fraction.

Knuth's model [12] is established based on Young's modulus, thermal expansion, and static friction. The model assumes that when the water droplets freeze on the substrate surface, the water droplets expand and freeze in the surface topography, creating a "clamping" mechanism. In order to separate ice from the substrate, the clamping mechanism must be overcome. Assuming there are two methods to separate the ice. The first method assumes that the shear force is perpendicular to the valley on the substrate surface at the microscale. The perpendicular shear force of ice covering the substrate surface is expressed as Eq. (2). The second method assumes that the shear force is parallel to the valley on the substrate surface at the microscale. The parallel shear force of ice covering the substrate surface is expressed as Eq. (3) [12].

$$S_0 = EA_0 \alpha \Delta T (\mu_0 \cos \theta_0 + \sin \theta_0) \quad (2)$$

$$S_0 = 2\mu_0 EA_0 \alpha \Delta T \quad (3)$$

Where  $S_0$  is the shear force required to shed ice;  $E$  is Young's modulus of ice;  $A_0$  is the Initial area of surface and ice contact;  $\alpha$  is the thermal coefficient of expansion;  $\Delta T$  is the change in ambient temperature;  $\mu_0$  is the coefficient of static friction;  $\theta_0$  is the slope of surface topography, defined as negative with respect to the horizontal plane.

Shen [13] proposed and established an analytical model for expressing the icing adhesion strength based on the mechanical theory, the principles of substrate thermal deformation theory, and the tribology theory. Under a series of assumptions, the relationship between adhesion strength and some parameters, including thermal expansion, bulk modulus, and surface temperature difference of substrates, was established. The model characterizes the surface morphology of the substrate by surface roughness parameters. The adhesion strength of ice covering the surface of substrate material is expressed as Eq. (4) [13].

$$\tau = \frac{\mu K_i K_m \Delta T_2 A (\gamma_i V_{i1} - \gamma_m V_{m0})}{S(\cos \theta_1 - \mu \sin \theta_1)(K_i V_{m2} + K_m V_{i2})} \quad (4)$$

Where  $\mu$  is the static friction coefficient between the ice and the peak;  $K_i$  is the bulk modulus of ice;  $K_m$  is the bulk modulus of the substrate material;  $\Delta T_2$  is the difference in temperature between the beginning of ice contraction and the full ice contraction;  $A$  is the contact area between the ice and the peak;  $\gamma_i$  is the volume expansion coefficient of ice;  $V_{i1}$  is the volume of ice before contraction when liquid water completely freezes;  $\gamma_m$  is the volume expansion coefficient of substrate material;  $V_{m0}$  is the volume of the naked peak before the liquid water contacts the substrate material at the ambient temperature;  $S$  is the bottom area of a model unit;  $\theta_1$  is the included angle between the conical busbar and the diameter of the bottom;  $V_{m2}$  is the volume of the peak after free contraction at the ambient temperature if there is no squeeze of the ice due to contraction;  $V_{i2}$  is the volume of ice after free contraction at the ambient temperature if there is no obstacle of the peak.

Although scholars have carried out a lot of exploration, the calculation results of these models can not well predict the ice adhesion strength. The relationship between the ice adhesion strength, surface topography, and material parameters still needs in-depth exploration. Compared to theoretical research, the experimental method is also important for exploring the icing mechanism. Some scholars have researched the relationship between surface roughness and ice adhesion strength in experimental research but have not yet reached a consistent conclusion. In this chapter, according to the existing research results, the relationship between surface roughness and ice adhesion strength can be roughly classified into two categories.

1. There is a correlation between ice adhesion strength and surface roughness. The research of Druez et al. shows a correlation between ice adhesion strength and surface roughness in the range of surface roughness of industries. The ice adhesion strength increases with the increase of surface roughness. When the surface roughness is greater than 20  $\mu\text{m}$ , the adhesion strength tends to extremum [14]. Zhu et al. [15]. found that the adhesion strength increases with surface roughness when surface roughness changes continuously from 3 to 33  $\mu\text{m}$ . The study of Chu and Scavuzzo [16] shows that the ice adhesion strength depends on surface roughness to a great extent. The research of Ding et al. showed that the ice adhesion strength increases with the increase of surface roughness for the hydrophilic surface. In contrast, the changing trend of adhesion strength is the opposite for the hydrophobic surface. There is a significant linear relationship between ice adhesion strength and surface roughness [17]. The research of Guo et al. found that surface roughness greatly affects the ice adhesion strength. Generally speaking, with the increase of surface roughness, the ice adhesion strength of the substrate surface also increases [18].

Zou et al. [19]. found that the ice adhesion strength on the rough surface is much higher than that on the smooth surface.

2. There is no correlation between ice adhesion strength and surface roughness. The study of Sait Alansatan et al. showed that the ice adhesion strength varies with the surface roughness change, but there is no clear trend between them [20].

#### 4. Electronic theory

The electronic theory was mainly proposed by Deryaguin [21]. The electronic theory holds that adhesion is the electrostatic force generated by the electron transfer forming the double-layer charges on the ice-substrate interface. The schematic diagram of the adhesion mechanism of electronic theory is shown in **Figure 4** [9]. This theory is the most controversial of all adhesion theories since it is difficult to prove the existence of double-layer charges without destroying the ice.

In 1997, Ryzhkin and Petrenko [22] first applied the electronic theory to explore the adhesion mechanism between ice and substrates. They proposed and established an electrostatic model based on the existence of the surface states of protonic charge carriers on the surface of ice. The model reveals the relationship between the electrical and adhesive properties of the ice surface, calculating the order of magnitude of adhesive energy at distances greater than one intermolecular distance. The model calculates the order of magnitude of adhesive energy significantly greater than chemical bonding energy and van der Waals forces.

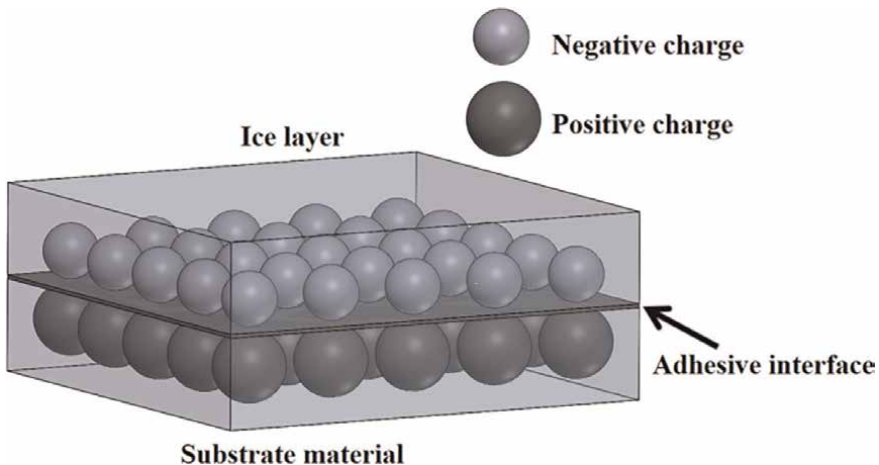


**Figure 4.**  
The schematic diagram of the electronic adhesive mechanism [9].

#### 5. Wetting theory

Wetting theory, also known as adsorption (thermodynamic) theory, is currently a popular adhesion theory. The theory was proposed by Sharpe and Schonhorn in 1963. The wetting theory holds that adhesion is caused by the interaction between the molecules on the interface when the water droplets are in close contact with the



substrate. Therefore, the standard of adhesive performance is essentially the standard of wettability. The contact angle is an important index for evaluating wettability. The schematic diagram of the adhesion of water droplets on the substrate surface is shown in **Figure 5** [9].

As shown in **Figure 5**, when the droplet is on the substrate surface, the droplet adopts a balanced structure that minimizes the system's energy. Young's Equation first described this equilibrium condition, as shown in Eq. (5) [23].

$$\gamma_{w,s} + \gamma_w \cos \theta = \gamma_s \quad (5)$$

Where  $\gamma_w$  is the surface energy of the liquid–vapor interface;  $\gamma_{w,s}$  is the surface energy of the solid–liquid interface;  $\gamma_s$  is the surface energy of the solid–vapor interface;  $\theta$  is the contact angle formed by the liquid drop and solid.

As shown in **Figure 5**, if the droplet on the substrate surface (S) is frozen into ice (i), the work required to remove the ice from the substrate surface is called the thermodynamic work of adhesion  $W_a$ . The definition of  $W_a$  is shown in Eq. (6) [23].

$$W_a = \gamma_s + \gamma_{ice} - \gamma_{i,s} \quad (6)$$

Where  $\gamma_{ice}$  is the surface energy of the ice–vapor interface;  $\gamma_{i,s}$  is the surface energy of the solid–ice interface.

According to Eqs. (5) and (6),  $W_a$  can be expressed as Eq. (7) [23].

$$W_a = \gamma_{ice} + \gamma_w \cos \theta + (\gamma_{w,s} - \gamma_{i,s}) \quad (7)$$

The surface energy of the solid–liquid interface of water is roughly same as that of ice, so  $\gamma_{w,s} \approx \gamma_{i,s}$  [24]. Now assuming that the surface energy of the liquid–vapor interface of ice and water is also approximately the same,  $W_a$  can be expressed as Eq. (8) [23].

$$W_a \approx \gamma_w (1 + \cos \theta) \quad (8)$$

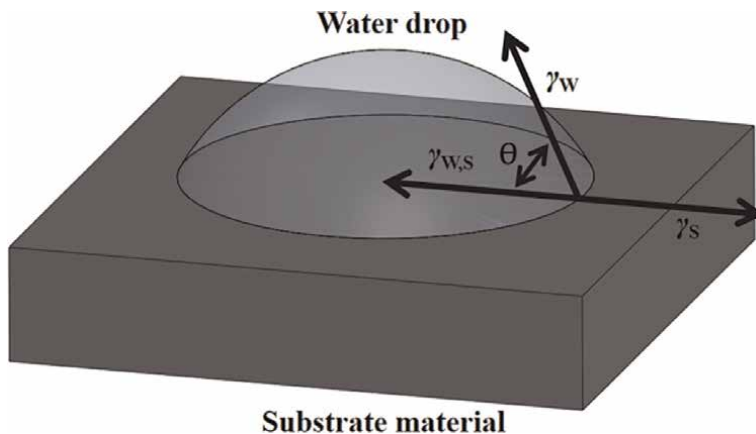


**Figure 5.**  
 Schematic diagram of the interaction among solid, liquid, and gas interface [9].

According to Eq. (4), the thermodynamic work of ice adhesion can be approximately calculated by the surface energy of the solid–liquid interface and the contact angle of water on the substrate surface. The relationship among the thermodynamic work of adhesion, the surface energy of the liquid–vapor interface, and the contact angle is shown in **Figure 6** [23].

In experimental research, scholars have done much research on the relationship between water wettability and ice adhesive properties but have not formed a uniform conclusion. According to the existing research results, this chapter roughly classifies the relationship between water wettability and ice adhesive properties into three categories.

1. There is a correlation between ice adhesive properties and contact angle. Dotan et al [25]. found that the larger the contact angle, the lower the ice adhesion strength. Andersson et al. found that, for rubber substrates, when the contact angle is less than 90 degrees, the adhesion strength of ice decreases linearly with the increase of contact angle. When the contact angle is greater than 90 degrees, the adhesion strength of ice remains almost unchanged [26].
2. There is a correlation between ice adhesive properties and contact angle only if the surface roughness is similar. Zou et al. reported that the adhesion strength of ice is only related to the contact angle when the surface roughness is similar. The adhesion strength of ice decreases with the increase of the contact angle [19]. Pang et al. found that higher contact angles lead to lower ice adhesion strength for coatings with the same surface roughness. For the coatings with different surface roughness, the adhesion strength of ice depends on the surface roughness rather than the contact angle [27].
3. There is a correlation between the ice adhesive properties and the contact angle hysteresis. Kulinich and Farzaneh [28, 29] found that the adhesion strength of ice has a good correlation with the contact angle hysteresis on the super-hydrophobic surface. When the contact angle hysteresis is low, the adhesion strength of ice is lower.

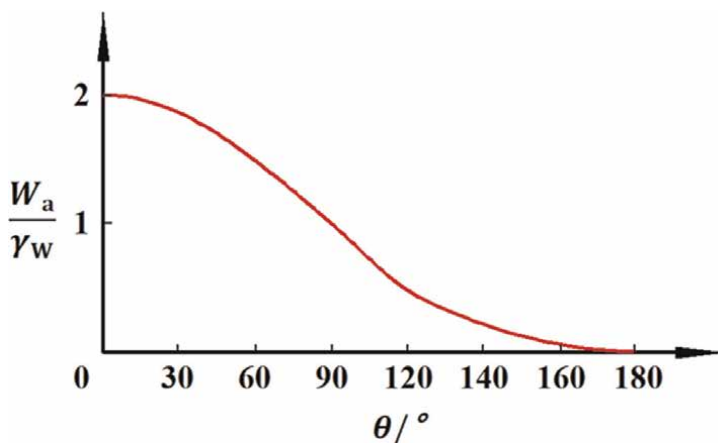


**Figure 6.** Thermodynamic work of ice adhesion scaled by the surface tension of water as a function of water contact angle  $\theta$  [23].

## 6. Summary

For the research on the icing mechanism of wind turbines, this chapter briefly summarizes the significant icing theories. The conclusions are as follows:

The icing adhesive theory mainly includes mechanical, electrostatic, and wetting theories. The three theories explain the icing adhesive properties from different viewpoints. However, each theory has its limitations and needs further improvement. Under actual conditions, the icing adhesive properties are also affected by environmental conditions, such as ambient temperature, wind speed, liquid water content, medium volumetric diameter, and liquid water composition, etc. In future research, the influence of environmental factors on adhesive properties should be considered. In addition, research on the icing adhesive theory of wind turbines has not been reported. The research on the icing adhesive theory of wind turbines should be based on the existing theories, introduce relevant theories, and carry out in-depth fusion research. This chapter can provide a reference for studying ice adhesive properties and anti-icing and de-icing technologies of wind turbines.

## Acknowledgements

This research was funded by “National Natural Science Foundation of China (NSFC), grant number 51976029”.

## Conflict of interest

The authors declare no conflict of interest.

## Appendices and nomenclature

$A$	Contact area between the ice and the peak ( $\text{m}^2$ )
$A_0$	The initial area of surface and ice contact
$E$	Young's modulus of ice
$f_{\text{cramp}}$	Fraction of mechanical locking
$f_{\text{por}}$	Porosity fraction
$f_{\text{RMS}}$	The fraction of ice in contact with the substrate
$K_m$	Bulk modulus of the substrate substrate (Pa)
$L$	Liquid
$S$	The bottom area of a model unit ( $\text{m}^2$ )
$S_0$	The shear force required to shed ice
$T$	Temperature (K)
$T_f$	Solidification temperature (K)
$T_{\text{ref}}$	Reference temperature (K)
$\Delta T$	The change in ambient temperature (K)
$\Delta T_2$	The difference in temperature between the beginning of ice contraction and the full ice contraction (K)
$V$	Vapor

$V_{i1}$	The volume of ice before contraction when liquid water completely freezes ( $m^3$ )
$V_{i2}$	The volume of ice after free contraction at the ambient temperature if there is no obstacle of the peak ( $m^3$ )
$V_{m0}$	The volume of the naked peak before the liquid water contacts the substrate at the ambient temperature ( $m^3$ )
$V_{m2}$	The volume of the peak after free contraction at the ambient temperature if there is no squeeze of the ice due to contraction ( $m^3$ )
$W_a$	Thermodynamic work of adhesion
$\alpha$	The thermal coefficient of expansion
$\alpha_{ice}$	The proportionality constant due to phase change
$\gamma$	Surface tension
$\gamma_i$	Volume expansion coefficient of ice ( $K^{-1}$ )
$\gamma_{i,S}$	The surface energy of the solid-ice interface.
$\gamma_{ice}$	The surface energy of the ice-vapor interface
$\gamma_m$	Volume expansion coefficient of substrate ( $K^{-1}$ )
$\gamma_S$	The surface energy of the solid-vapor interface
$\gamma_W$	The surface energy of the liquid-vapor interface
$\gamma_{W,S}$	The surface energy of the solid-liquid interface
$\delta_0$	Molecular distance
$\theta$	The contact angle formed by the liquid drop and solid (degrees)
$\theta_0$	The slope of surface topography, defined as negative with respect to horizontal plane (degrees)
$\theta_1$	Included angle between the conical busbar and the diameter of the bottom (degrees)
$\kappa$	Root mean square roughness height
$\mu$	Static friction coefficient between the ice and the peak
$\mu_0$	The coefficient of static friction
$\tau$	Adhesion strength of ice (Pa)
$\tau_f$	Ice shear strength (Pa)
$\chi$	Electronegativity

## **Author details**

He Shen<sup>1</sup> and Yan Li<sup>1,2\*</sup>


1 Department of Agricultural Biological Environmental and Energy Engineering,  
College of Engineering, Northeast Agricultural University, Ha'erbin, China

2 Heilongjiang Provincial Key Laboratory of Technology and Equipment for the  
Utilization of Agricultural Renewable Resources in Cold Region, Ha'erbin, China

\*Address all correspondence to: [liyanneau@163.com](mailto:liyanneau@163.com)

## **IntechOpen**

---

© 2023 The Author(s). Licensee IntechOpen. This chapter is distributed under the terms of the Creative Commons Attribution License (<http://creativecommons.org/licenses/by/3.0>), which permits unrestricted use, distribution, and reproduction in any medium, provided the original work is properly cited. 

## References

- [1] Gao L, Tao T, Liu Y, et al. A field study of ice accretion and its effects on the power production of utility-scale wind turbines. *Renewable Energy*. 2021; **167**:917-928. DOI: 10.1016/j.renene.2020.12.014
- [2] Guo W, Shen H, Li Y, et al. Wind tunnel experiments of the rime icing characteristics of a straight-bladed vertical axis wind turbine. *Renewable Energy*. 2021; **179**:116-132. DOI: 10.1016/j.renene.2021.07.033
- [3] Zeng J, Song B. Research on experiment and numerical simulation of ultrasonic de-icing for wind turbine blades. *Renewable Energy*. 2017; **113**: 706-712. DOI: 10.1016/j.renene.2017.06.045
- [4] Li Y, Shen H, Guo W. Effect of ultrasonic vibration on the surface adhesive characteristic of iced aluminum alloy plate. *Applied Sciences*. 2022; **12**: 2357. DOI: 10.3390/app12052357
- [5] Wang SL. Numerical simulation and icing wind tunnel test study on icing distribution on blade of horizontal axis wind turbine [thesis]. Harbin: Northeast Agricultural University; 2017
- [6] Li Y, Sun C, Jiang Y, et al. Scaling method of the rotating blade of a wind turbine for a rime ice wind tunnel test. *Energies*. 2019; **12**:627. DOI: 10.3390/en12040627
- [7] Stokke DD, Wu Q, Han G. Fundamentals of adhesion. In: Stokke DD, Wu Q, Han G, editors. *Introduction to Wood and Natural Fiber Composites*. 1st ed. Hoboken: John Wiley & Sons Ltd; 2013. pp. 129-168. DOI: 10.1002/9780470711804.ch5
- [8] Kumar RN, Pizzi A. Fundamentals of adhesion. In: Kumar RN, Pizzi A, editors. *Adhesives for Wood and Lignocellulosic Substrates*. 1st ed. Beverly: Scrivener Publishing LLC; 2019. pp. 31-59. DOI: 10.1002/9781119605584.ch2
- [9] Fourche G. An overview of the basic aspects of polymer adhesion Part I: Fundamentals. *Polymer Science and Engineering*. 1995; **35**:957-966. DOI: 10.1002/pen.760351202
- [10] Chaudhury MK, Kim KH. Shear-induced adhesive failure of a rigid slab in contact with a thin confined film. *The European Physical Journal E*. 2007; **23**: 175-183. DOI: 10.1140/epje/i2007-10171-x
- [11] Fortin G, Perron J. Ice adhesion models to predict shear stress at shedding. *Journal of Adhesion Science and Technology*. 2012; **26**:523-553. DOI: 10.1163/016942411X574835
- [12] Knuth TD. Ice Adhesion Strength Modeling Based on Surface Morphology Variations [thesis]. Pennsylvania: The Pennsylvania State University; 2015
- [13] Shen H. Analytical and experimental researches on the airfoil surface adhesion strength of ice for wind turbine blade [thesis]. Harbin: Northeast Agricultural University; 2022
- [14] Druetz J, Phan CL, Laforte JL, et al. The adhesion of glaze and rime on aluminium electrical conductors. *Transactions-Canadian Society for Mechanical Engineering*. 1978; **5**:215-220. DOI: 10.1139/tcsme-1978-0033
- [15] Zhu CX, Zhu CL, Zhao WW, et al. Experimental study on the shear adhesion strength between the ice and substrate in icing wind tunnel. *Journal of Mechanics*. 2017; **34**:209-216. DOI: 10.1017/jmech.2017.83

- [16] Chu MC, Scavuzzo RJ. Adhesive shear strength of impact ice. *AiAA Journal*. 1991;**29**:1921-1926. DOI: 10.2514/3.10819
- [17] Yunfei D, Shan T, Huijun W. Study on influence of surface microstructure on ice adhesion strength. *Surface Technology*. 2015;**44**:74-78. DOI: 10.16490/j.cnki.issn.1001-3660.2015.04.013
- [18] Guo Q, Shen XB, Lin GP, et al. Experimental analysis on adhesion force between ice and substrate. *Aircraft Design*. 2019;**39**:33-37. DOI: 10.19555/j.cnki.1673-4599.2019.04.008
- [19] Zou M, Beckford S, Wei R, et al. Effects of surface roughness and energy on ice adhesion strength. *Applied Surface Science*. 2011;**257**:3786-3792. DOI: 10.1016/j.apsusc.2010.11.149
- [20] Alansatan S, Papadakis M. Experimental investigation of ice adhesion. *SAE Technical Papers*. 1999; **01**(1584):01-12. DOI: 10.4271/1999-01-1584
- [21] Deryaguin BV. Problems of Adhesion. *Vestnik Akademii*. 1955;**8**:70. DOI: 10.1016/0079-6816(94)90053-1
- [22] Ryzhkin IA, Petrenko VF. Physical mechanisms responsible for ice adhesion. *The Journal of Physical Chemistry B*. 1997;**101**:6267-6270. DOI: 10.1021/jp9632145
- [23] Makkonen L. Ice adhesion-theory, measurements and countermeasures. *Journal of Adhesion Science and Technology*. 2012;**26**:413-445. DOI: 10.1163/016942411X574583
- [24] Makkonen L. Surface melting of ice. *The Journal of Physical Chemistry B*. 1997;**101**(32):6196-6200. DOI: 10.1021/jp963248c
- [25] Dotan A, Dodiuk H, Laforte C, et al. The relationship between water wetting and ice adhesion. *Journal of Adhesion Science and Technology*. 2009;**23**(15): 1907-1915. DOI: 10.1163/016942409x12510925843078
- [26] Andersson LO, Golander CG, Persson S. Ice adhesion to rubber substrates. *Journal of Adhesion Science and Technology*. 1994;**8**:117-132. DOI: 10.1163/156856194X00104
- [27] Pang H, Zhou S, Gu G, et al. Long-term hydrophobicity and ice adhesion strength of latex paints containing silicone oil microcapsules. *Journal of Adhesion Science and Technology*. 2013;**27**:46-57. DOI: 10.1080/01694243.2012.701503
- [28] Kulinich SA, Farzaneh M. Ice adhesion on super-hydrophobic surfaces. *Applied Surface Science*. 2009;**255**: 8153-8157. DOI: 10.1016/j.apsusc.2009.05.033
- [29] Kulinich SA, Farzaneh M. How wetting hysteresis influences ice adhesion strength on super-hydrophobic surfaces. *Langmuir*. 2009;**25**:8854-8856. DOI: 10.1021/la901439c





## Chapter 6

# Experimental Study on the Ultrasonic De-Icing Method of Wind Turbine Blades

*Jianlong Ma, He Shen and Wenfeng Guo*

### Abstract

Ice accretion on the wind turbine blade degrades the aerodynamic performance and power efficiency of wind turbines. Therefore, developing a high-efficiency de-icing method with low energy consumption is necessary to stabilize their operation in winter. Now, there are several types of de-icing methods being developed. Among these methods, ultrasonic de-icing method is suitable for wind turbines because of its low energy consumption, simple structure, and easy installation. In this chapter, the theoretical and experimental studies on ultrasonic de-icing of wind turbines are introduced. The de-icing vibration modes of plate element and airfoil blade with NACA0018 were analyzed and determined. The anti-icing and de-icing effects of ultrasonic vibration on the iced plate and blade segment were tested by the experimental methods. An icing wind tunnel system and two kinds of de-icing measurement devices were designed and built. The adhesive strengths of ice on the plate and airfoil blade surface were measured with variation in frequency. The experimental results show that ultrasonic vibration could decrease the amount and the adhesive strength of ice dramatically and had de-icing capability at the frequency of de-icing vibration mode. The research findings are useful and helpful to the development of ultrasonic de-icing technology in future works.

**Keywords:** wind turbine, anti-icing, de-icing, ultrasonic, experimental method

### 1. Introduction

With the rapid development of technology, air pollution and global warming have become serious problems for each country. Therefore, clean and renewable energies are important to us. Wind energy, as one of the most successful and widely used renewable energies, is mainly applied to wind power generation. However, for wind turbines working in humid and cold environments, ice accretion sometimes occurs on the blade surface. It changes the profile and degrades the aerodynamic performance of the airfoil blade. Then the power efficiency of wind turbines decreases. Moreover, icing on the blade increases the weight and destroys the dynamic balance of the rotor, which shortens the lifespan of wind turbine. Occasionally, ice-shedding events

threaten the surrounding buildings or people [1–3]. Thus, it's necessary to develop anti- and de-icing technologies for wind turbines.

At present, there are several kinds of de-icing methods in development, such as electro-thermal de-icing, fluid thermal de-icing, pneumatic de-icing, electric-pulse de-icing, microwave de-icing, surface coating de-icing, and ultrasonic vibration de-icing [4–7]. Among these de-icing methods, electro-thermal de-icing method is widely used because of its simple structure, but it costs a great amount of electric energy in the process of de-icing. It's not available for wind turbines, which are a kind of power generation equipment that decreases power efficiency. Similarly, the microwave de-icing method also costs a large amount of energy. Moreover, fluid thermal de-icing and pneumatic de-icing methods have large volumes and complex structures. For the electric-pulse de-icing method, it's complicated due to the high distribution density of the coil. Additionally, it's only available on metal surfaces. When it works, the metal surface will generate large deformation. The surface coating method uses the hydrophobic material to decrease the amount of ice. It's a kind of active de-icing method. However, the coating is fragile and prone to falling off. After that, it's failure to protect the surface. In contrast, the ultrasonic de-icing method has the features of low energy cost, small vibration amplitude, long lifespan, lightweight, no noise, simple structure, easy installation, and so on [8]. A wind turbine is a power generation device that transforms wind energy into electricity. Therefore, conversion efficiency is an important parameter for it. If the de-icing method consumes a lot of energy in operation, the power generation efficiency will decrease overall. Therefore, it's necessary to find a low-energy-cost de-icing method for wind turbines. In this case, the ultrasonic de-icing method is considered one of the available de-icing methods, especially for wind turbines. Nevertheless, the de-icing mechanism of it has not been explored clearly, and the technology of it is in development. Now, scholars have carried out some research on ultrasonic de-icing by theoretical and experimental methods [9, 10]. Simulation is the most widely used method. In this way, the stress distributions at the interface between substrate and ice were analyzed. Experimental method is commonly used to validate the effect of theoretical findings. In these tests, the parameter of de-icing time was always used to assess the de-icing effect. However, the effect of ultrasonic vibration on the adhesive strength of ice was seldom tested by experiment.

In this paper, an aluminum plate and airfoil blade segment were selected as research objects, and the de-icing effects of ultrasonic vibration on the adhesive strength of ice on the plate and blade segment were explored. First, the de-icing vibration mode and the distribution of shear stress at the adhesive interface between ice and substrate were analyzed by simulation. Based on the simulation results, two types of devices measuring the adhesive force of ice were designed and manufactured. Then the effects of ultrasonic vibration on the adhesive strength of ice covering on the plate and airfoil blade were examined by experiments.

## **2. Ultrasonic de-icing effect on plate element**

In this part, the effect of ultrasonic vibration on the iced plate is introduced. For the large-scale wind turbine, the surface profile of the blade can be simplified into two kinds of shapes, which are the plane and the volume, as shown in **Figure 1**.

As shown in **Figure 1**, at the leading edge, the curvature at this position is highest all over the blade surface. In contrast, the curvature of the blade body surface is the lowest, which is approximately a plane surface. Therefore, it can be considered a plane

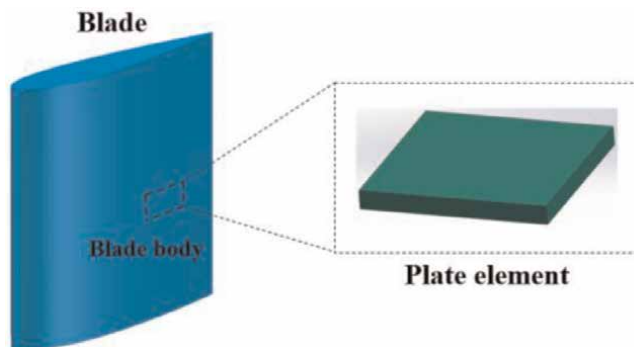


**Figure 1.**  
*Sketch map of large-scale blade segment.*

surface. That's why the de-icing effect of ultrasonic vibration on the adhesive strength of the iced blade was explored in the present study. Therefore, an aluminum plate was selected as a research object to carry out the relevant research. The reason for the selection of aluminum material is that the thermal conductivity of metal is isotropic. It's helpful to carry out essential research. For real wind turbine blades, most of them are mainly made of composite material, such as carbon fiber or glass fiber-reinforced plastics. These materials are anisotropic in physical and thermal characteristics, which brings out difficulties in the initial test. Moreover, some small-scale wind turbines, such as vertical-axis wind turbines, are made of aluminum material, and many scholars conducted research on the icing characteristics of wind turbines using the aluminum airfoil blade segment. In these cases, aluminum material was used in the present study.

## 2.1 Simulation on the iced plate

The principle of the ultrasonic de-icing method is shown in **Figure 2**. As shown in **Figure 2**, the piezoelectric ceramic patch (PZT patch) is adhered to opposite surface without icing. When the PZT patch is excited by alternating current (AC) voltage, it stretches and contracts alternatively, resulting in high-frequency vibration. In this case, the iced plate vibrates and deforms along with the PZT patch. Then there is shear stress at the adhesive interface between ice and plate. When the shear stress is higher than the adhesive shear strength of ice, the adhesive strength of ice is weakened, or the ice is removed even more.

For exploring the mechanism of ultrasonic de-icing, an aluminum plate was selected as the simulation object. The configuration parameters are listed in **Table 1**.

Based on the iced plate model, the model analyzes were conducted by ANSYS. The simulation parameters are listed in **Tables 2** and **3**, and the vibration modes of the plate, the first vibration mode and the fourth one, are shown in **Figure 3**.

As shown in **Figure 3**, the four sides of plate were constrained in the process of the simulation, which were the boundary conditions in the simulation. For each vibration mode, the deformation distributes symmetrically. The symmetry axes of them are along horizontal and vertical directions. In the present study, the first vibration mode was selected as a research object. According to the vibration mode, the position of the PZT patch was decided to be located at the center of the plate, which is similar to the one in **Figure 2**.

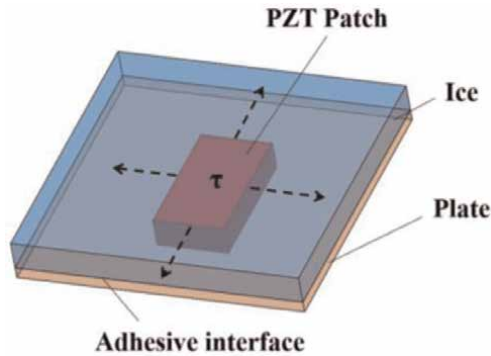


**Figure 2.**  
Model of iced plate element for ultrasonic de-icing.

Side length of plate	Thickness of plate	Thickness of ice
60mm × 60 mm	1 mm	2 mm

**Table 1.**  
Configuration parameters of iced plate.

Objects	Element types
Ice	SOLID186
Aluminum plate	SOLID186
PZT patch	SOLID226

**Table 2.**  
Element type in simulation.

Materials	Items	Values
Ice	Density	$0.9 \times 10^3 \text{ kg/m}^3$
	Elastic modulus	$8.7 \times 10^9 \text{ Pa}$
	Poisson ratio	0.33
Aluminum	Density	$2.7 \times 10^3 \text{ kg/m}^3$
	Elastic modulus	$7 \times 10^{10} \text{ Pa}$
	Poisson ratio	0.3
Piezoelectric ceramic	Density	$7.5 \times 10^3 \text{ kg/m}^3$

**Table 3.**  
Material parameters.

As shown in **Figure 2**, the position and size of the PZT patch are decided according to the first vibration mode. From the cloud picture of the first vibration mode, the highest bending amplitude is located in this position. Therefore, when there is an excitation load impacting this position, the largest bending deformation of plate can be realized. In this case, the higher shear stress can be generated at the adhesive interface between ice and plate.

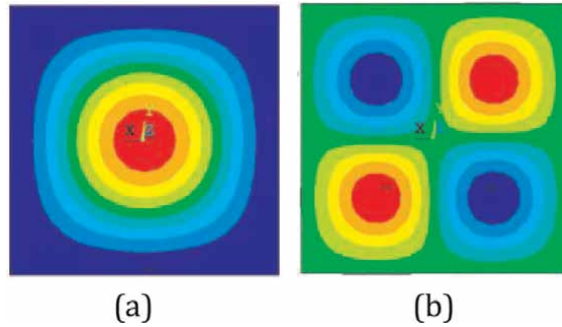


**Figure 3.**  
*Vibration modes.*

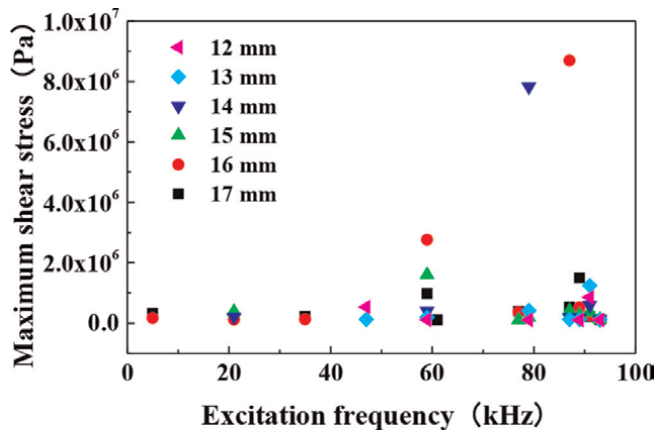


**Figure 4.**  
*Variations of the maximum shear stresses at the adhesive interface.*

Based on the model analysis, harmonic analysis was carried out, and the maximum shear stress at the adhesive interface between ice and aluminum plate was calculated. Some results with higher shear stress are shown in **Figure 4**.

As shown in **Figure 4**, it shows the variations of maximum stresses at the adhesive interface with excitation frequency under different side lengths of PZT patches. The side length of PZT patch varies from 12 to 17 mm. From the figure, it is found that the size of PZT patch has an effect on the maximum stress, and there are some conditions where the maximum shear stresses are far higher than the other conditions. In the previous works, it was concluded that the shear adhesive strength of ice was the lowest in comparison with the ones along other directions. That's why the shear stress at the adhesive interface was selected as the de-icing parameter.

## 2.2 Experimental scheme

According to the previous experiments, the adhesive shear stress is about 0.3 ~ 1.8 MPa. Combining the simulation results with the previous experimental result, the effect of ultrasonic vibration on the adhesive strength of ice was determined by experiment. The experimental scheme is listed in **Table 4**.

Thickness of ice (mm)	Thickness of the PZT patch (mm)	Experimental temperature (°C)	Excitation voltage $V_{p-p}$ (V)	Side length of PZT patch (mm)	Excitation frequency (kHz)
2	2	-18	400	16	0
					85
					87
					89
				14	0
					77
					79
					81

**Table 4.**  
*De-icing experimental scheme for iced plate.*

In the present study, an alloy aluminum plate with material model 7075 was used as a test coupon, and the size of it was 60 mm × 60 mm × 2 mm. The PZT patch with the material model PZT4 was selected, and two kinds of side lengths, 16 mm × 16 mm × 2 mm and 14 mm × 14 mm × 2 mm, were selected as listed in **Table 4**. For the ice sample, the thickness was 2 mm, and the ambient temperature was -18°C. Additionally, the sinusoidal voltage was used as excitation voltage, and the peak-to-peak voltage  $V_{p-p}$  is 400 V. According to the harmonic analysis results for the maximum shear stress, several frequencies were selected in the present experiment as listed in **Table 4**.

### 2.3 Experimental system

The experimental system in the present study is shown in **Figure 5**.

As shown in **Figure 5**, the experimental system is comprised of a signal generator, an ultrasonic power amplifier, a device for measuring the adhesive torque of ice, and so on. The signal generator, whose model is RIGOL DG1022Z, is used to generate low sinusoidal signal voltage. The ultrasonic power amplifier, whose model is LONG YI DGR-3001, is used to amplify the power of the sinusoidal signal from the signal generator and drive the PZT patch to vibrate at high frequency. The device for measuring the adhesive strength of ice is used to measure the adhesive torque of ice. In this way, the adhesive shear strength of ice can be measured.

### 2.4 Experimental results

Based on the above experimental system, the adhesive torques of ice were measured under different conditions. However, for analyzing the de-icing effect of ultrasonic vibration in comparison, the adhesive torque in the unit area, which is the adhesive shear stress, is calculated. The analytical formula is expressed by Eq. (1).

$$\tau_a = \frac{12M}{[2\sqrt{2} + \ln(3 + 2\sqrt{2})]L^3} \quad (1)$$

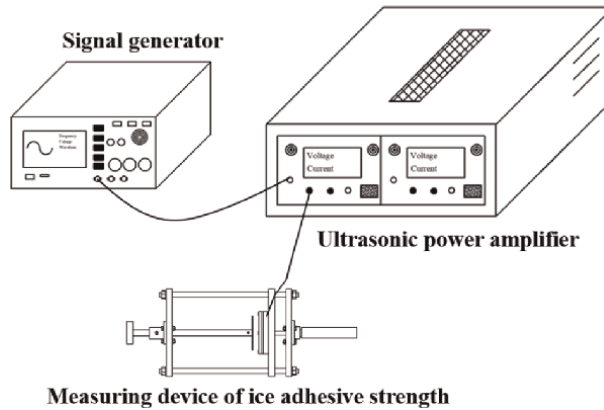


**Figure 5.**  
 Sketch map of experimental system.

where,  $M$  is the adhesive torque of ice covering on the whole aluminum alloy plate surface;  $L$  is the side length of an iced aluminum alloy plate.

Then the adhesive shear stresses under different experimental conditions are calculated according to the experimental results. The variation in frequency is shown in **Figure 6**.

As shown in **Figure 6**, when the iced plate was not excited by ultrasonic vibration, the adhesive shear stress was higher than that under ultrasonic vibration. The adhesive shear stress was about 0.21 MPa. In comparison, when the PZT patch is  $14\text{ mm} \times 14\text{ mm} \times 2\text{ mm}$ , the adhesive shear stress is only 0.014 MPa under the vibration frequency of 79 kHz. It's just 7% of that without ultrasonic vibration. However, when the vibration is 81 kHz the adhesive shear stress is similar to that without ultrasonic vibration. Ultrasonic vibration did not have de-icing effect. It validates that high shear stresses only exist at special frequencies, such as 79 kHz. Under these conditions, ultrasonic vibration can increase the shear stress at the interface between ice and substrate, which decreases the adhesive strength of ice. On the contrary, at the other frequency, such as 81 kHz, the shear stress is low at the interface, and the

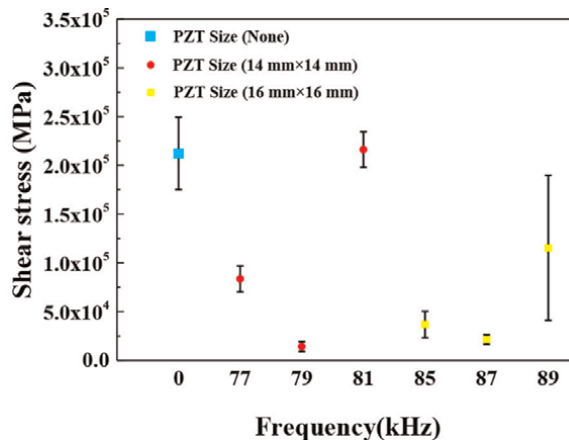


**Figure 6.**  
 Variation of shear stress with frequency.

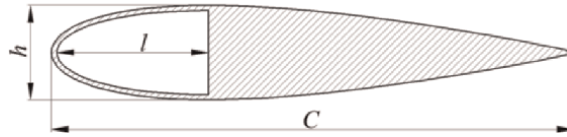


**Figure 7.**  
*Sketch map of an airfoil blade.*

adhesive shear strength of ice did not change at all. The experimental results agreed with the simulation results as listed in **Figure 4** and **Table 2**. **Figure 6** also validates the ultrasonic de-icing effect, as the size of the PZT patch was  $16 \text{ mm} \times 16 \text{ mm} \times 2 \text{ mm}$ . Under the excitation frequencies of 85 and 87 kHz, the adhesive shear stresses were just 0.037 and 0.021 MPa, respectively, which were far lower than that without ultrasonic vibration.

### 3. Ultrasonic de-icing effect on airfoil blade

Based on the ultrasonic de-icing effect on the iced plate element, the de-icing effect on the airfoil blade was also explored in the present study.

#### 3.1 Simulation

In this paper, an airfoil blade segment was selected as research object. The sketch map of it is shown in **Figure 7**.

As shown in **Figure 7**, the blade segment with airfoil of NACA0018 has a hollow structure. The reason for the selection of this airfoil is that NACA0018 has a symmetric profile, which is widely used to carry out basic research such as aircraft icing and wind turbine icing. For this airfoil, there is a hollow structure at the leading edge that is used to lay out the PZT patches. In the previous work, it was found that ice accretion often occurred on the leading edge, such as on aircraft wings and wind turbine blades. Icing destroys the profile of airfoil and results in the degradation of aerodynamic performance. Therefore, it's necessary to explore the de-icing technology of airfoil blades. In the previous work, it was found that the ice accretion position along the chord length was less than 30%. Therefore, in the present design, the ratio of chord length  $l$  at the hollow position to the whole chord length  $C$  is 30%. Moreover, aluminum alloy is selected as the material of airfoil blade. The reason for the selection is that the aluminum alloy has isotropic and high heat transfer coefficient, which was widely used by many scholars to carry out airfoil blade icing.

Based on the structure of airfoil blade with a hollow structure, the model analysis of it was carried out by ANSYS, and the de-icing vibration mode was decided. The vibration mode is shown in **Figure 8**.

As shown in **Figure 8**, the natural frequency of this vibration mode is 22,779 Hz. There exist two reasons for its selection. First, the natural frequency of de-icing vibration mode must be higher than 20,000 Hz. In this range, the vibration belongs to ultrasonic range. Second, under this vibration mode, the leading edge of airfoil blade bends alternatively, and the bending deformation alters positively and negatively. In this case, the bending deformation distributes along the whole leading edge surface, which can generate shear stress at the adhesive interface between the ice and airfoil





**Figure 8.**  
*De-icing vibration mode of airfoil blade.*



**Figure 9.**  
*Test coupon of airfoil blade segment with PZT patches.*

substrate. Additionally, the amplitude of the bending deformation is the same along the direction of the wing span.

Based on the modal analysis, for exciting the bending deformation of airfoil blade, the PZT patches were laid out at the vibration amplitude in the present study. A test coupon of airfoil blade segment with PZT patches is shown in **Figure 9**.

### 3.2 Experimental scheme

After manufacturing the test coupon of airfoil blade, the impedance analysis of it was carried out by an impedance analyzer, whose model is ZX70A. The measuring scope of frequency is from 20 to 30 kHz. After that, three frequencies were selected as experimental parameters, which were 21,228, 25,604, and 27,254 Hz. Under these three frequencies, the impedances were higher than those under other natural frequencies. Based on them, the experimental scheme was designed and listed in **Table 5**.

### 3.3 Experimental system

In the present study, a de-icing system with ultrasonic excitation device for airfoil blade segment was designed and built. There are two parts in this system: the icing sub-system and the ultrasonic de-icing sub-system.

The icing sub-system is shown in **Figure 10**, which is used to simulate the icing environment of airfoil blade. As shown in **Figure 10**, it's a return-flow icing wind tunnel, and the working parameters are listed in **Table 6**. As listed in **Table 6**, the working parameters can meet the icing demand of airfoil blade segment.

The ultrasonic de-icing sub-system is comprised of two parts, which are the ultrasonic excitation devices and a self-developed device for measuring the adhesive strength of ice covered on the airfoil blade surface. The ultrasonic excitation devices have been given in **Figure 5**, which are used to apply an excitation voltage to the PZT patches in order to generate ultrasonic vibration. The adhesive strength measurement device was developed specially for testing airfoil blades, as shown in **Figure 11**.

As shown in **Figure 11**, the shear method is used in the present study to measure the adhesive strength of ice. After icing on the blade segment in the icing wind tunnel, the iced blade segment is mounted on the slider of the device, as shown in **Figure 12**. Then it moves along the parallel rails. The slider is driven by a screw-driving

Experimental conditions	Values
Experimental temperature	-12°C
Wind speed	4 m/s
Excitation frequency	21,228 Hz, 25,604 Hz, 27,254 Hz
Excitation voltage $V_{p-p}$	400 V
Angle of attack	0°

**Table 5.**  
*De-icing experimental scheme for iced blade.*



**Figure 10.**  
*Return flow icing wind tunnel.*

Working parameters	Values
Cross-section of the test section	250 × 250 mm <sup>2</sup>
Temperature	0°C ~ -20°C
Wind speed	0 ~ 20 m/s
Diameter of the water droplet	50 μm

**Table 6.**  
*Working parameters of the icing wind tunnel.*

mechanism where two pressure sensors are mounted on it. Under the driving of the pressure sensors, the iced airfoil blade goes through a de-icing hole, which has the same shape and size profile as the clean airfoil blade. In this case, the ice is removed by shear force, and the value is acquired by pressure sensors. In this way, the adhesive shear stress of ice covering the airfoil blade was measured. In the present study, the maximum value of measurement is determined as adhesive strength of ice.

### 3.4 Results and discussion

In the present study, the anti-icing and de-icing tests were conducted. The anti-icing test explored the effect of ultrasonic vibration on the amount of icing on the blade surface. The experimental scheme is listed in **Table 5**. The frequencies in the tests were 21,228z, 25,604, and 27,254 Hz. The excitation voltage was 400 V. The tests

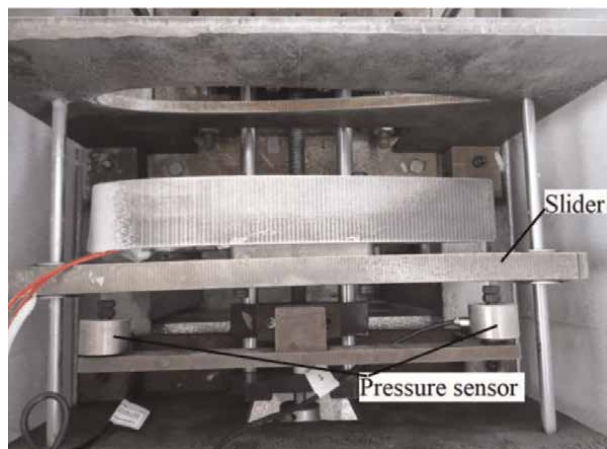


**Figure 11.**  
*Measurement device of adhesive strength of ice.*

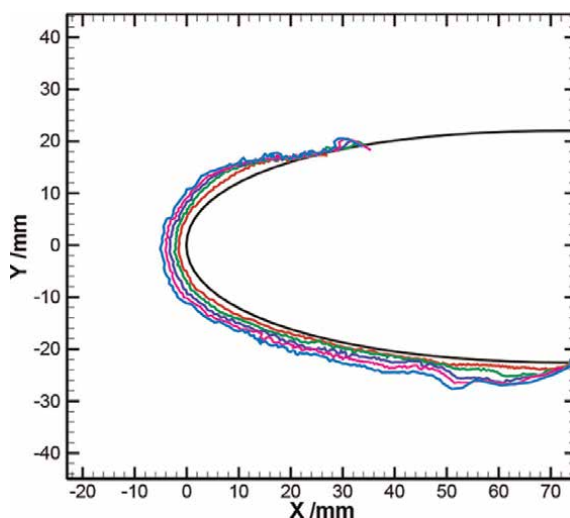


**Figure 12.**  
*Ice distribution on the blade surface under (21.228 kHz,  $-4^{\circ}\text{C}$ , 10 m/s).*

were conducted in the icing wind tunnel, and the icing process was recorded by a high-resolution camera. In this study, the ultrasonic vibration operated during the process of icing. And the ice distribution under different frequencies was obtained. For example, the one under the frequency of 21.228 kHz is shown in **Figure 12**.

In the present study, the type of ice is glaze ice. As shown in **Figure 12**, the ice grew layer by layer. The amount and covering area of ice on the lower blade surface were higher than those on the upper blade surface. When the water droplets impacted the blade surface, they did not freeze immediately. In this case, the water droplets converged and flew under the actions of wind and gravity. That's why the amount of ice on the lower blade surface was higher than the one on the upper blade surface. For quantitatively analyzing the amount of ice, one parameter was used in the present study, which is dimensionless icing area. The sketch map of it is shown in **Figure 13**.

As shown in **Figure 13**, the dimensionless icing area is expressed as Eq. (2).

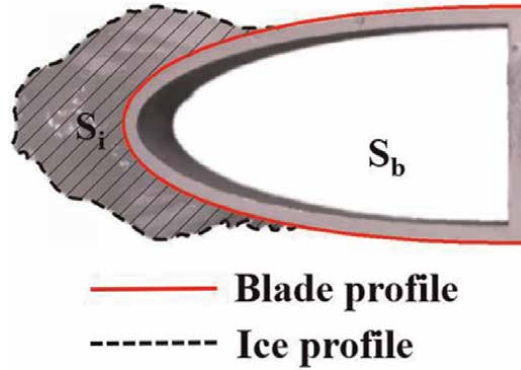


**Figure 13.**  
Sketch map of dimensionless icing area.

$$\eta_s = \frac{S_i}{S_b} \quad (2)$$

where  $\eta_s$  is the dimensionless icing area,  $S_i$  is the cross-section area of ice and  $S_b$  is the cross-section area of the blade.

Based on the definition, the effect of ultrasonic vibration on the amount of ice was analyzed, which is shown in **Figure 14**.

As shown in **Figure 14**, under non-vibration conditions, the amount of ice was highest, which validated that ultrasonic vibration had anti-icing effect on wind turbines. Moreover, it also shows that frequency has an effect on the amount of ice. From **Figure 14**, when the frequency is 25.604 kHz, the amount of ice was lowest. It indicates that the ultrasonic vibration has an obvious effect on anti-icing at this frequency. Additionally, at the initial stage of icing, the amounts of ice were approximate under different frequency conditions. With the increase in icing time, the discrepancy in the amount of ice emerges gradually. For this result, the water droplets could impact the cold blade surface at the initial icing time, and the water droplets freeze in a short time because of high heat transfer of blade material, such as aluminum in the present study. After that, as the blade surface was covered by ice layer, the subsequent water droplets did not impact the blade surface directly. The water droplets could not freeze instantly. In this case, the ultrasonic had an obvious effect on anti-icing, which resulted in a decrease in the amount of ice. It was beneficial to the operation and aerodynamic performance of wind turbines.

Based on the anti-icing tests, the ultrasonic de-icing tests were also conducted in the present study. The icing process was carried out in the above icing wind tunnel. After icing, the effect of ultrasonic vibration on the adhesive strength of ice was carried in the refrigerator by the self-developed device shown in **Figure 11**. Based on the experimental system, the adhesive strength of ice on the airfoil blade was measured by the self-developed device in **Figure 11**. For analyzing the results under different icing conditions comparatively, the adhesive shear stress of ice was calculated by Eq. (3).

$$\tau = \frac{F}{S} \quad (3)$$

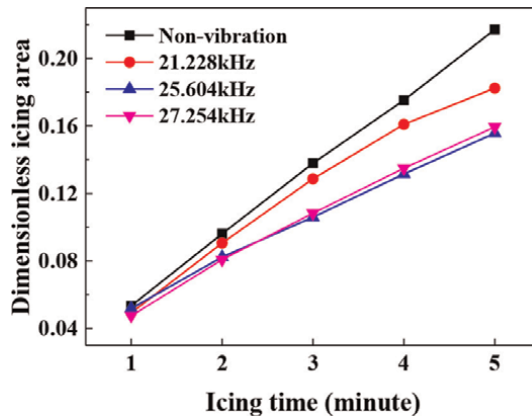


**Figure 14.**  
 Variations of dimensionless icing areas under different frequencies.

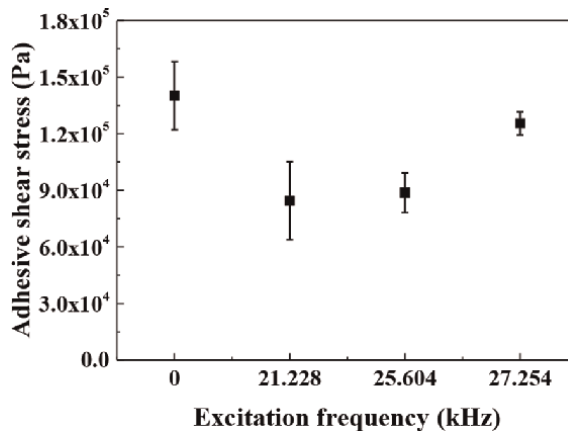


**Figure 15.**  
 Variation of adhesive shear stress of ice with frequency ( $-12^{\circ}\text{C}$ ,  $5\text{ m/s}$ ).

where  $\tau$  is the adhesive shear stress of ice;  $F$  is the shear force of the ice adhering to the blade surface;  $S$  is the area of ice covering the blade surface.

According to Eq. (3), the variation of adhesive shear stress of ice with ultrasonic vibration is shown in **Figure 15**.

As shown in **Figure 15**, without ultrasonic vibration, the adhesive shear stress of ice is about 0.14 MPa. The adhesive strength is lower than that shown in **Figure 6**. The difference was caused by the type of ice. For the test of iced plate in Section 2, the type of ice was glaze ice which was frozen by liquid water. However, in this test, the ice was generated by water droplets impinging on the blade surface. Additionally, the icing temperature was  $-12^{\circ}\text{C}$ . Under this condition, the type of ice was rime ice. For rime ice, there are spaces among iced water droplets. It leads to a decrease in the adhesive area of ice. For this reason, the adhesive strength of ice decreased. In contrast, the glaze ice was generated from liquid water. There is no space in the body of ice, and the adhesive area with the substrate was large, which resulted in a high adhesive strength of ice.

**Figure 15** also validates that ultrasonic vibration has a de-icing effect on the iced airfoil blade. The adhesive strength of ice decreased under the ultrasonic vibration.

When the vibration frequency was 21.228 kHz, the adhesive strength of ice was at its lowest, which was approximately 0.084 MPa. The frequency was approximated by the theoretical one calculated in modal analysis. It validated that the leading edge bending alternately along the blade surface and symmetrically along the chord had a better de-icing effect. Additionally, under the other excitation conditions, such as 25.604 and 27.254 kHz, the adhesive strength of ice also decreased, but the values were higher than the one in the condition of 21.228 kHz. Especially for the one under the frequency of 27.254 kHz, the adhesive strength of the ice decreased a little. It also validates that the shear stress at the interface under this excitation condition was small, which has little effect on de-icing. Conclusively, for an airfoil blade, there exists a de-icing vibration mode, which is the best one for the ultrasonic de-icing method.

#### **4. Conclusions**

In the present study, the de-icing effect of ultrasonic vibration on the plate element and airfoil blade was explored through simulations and experiments. Some conclusions are presented as follows:

1. An aluminum plate element was selected as research object. The modal analysis and harmonic analysis of it were carried out. Based on the first vibration mode, the location of PZT patch was decided, and the maximum shear stresses at the adhesive interface between ice and substrate were calculated under different frequencies. The theoretical result shows that ultrasonic vibration has a de-icing effect. Based on the theoretical analysis, the experimental scheme was decided.
2. An experimental system was designed and built for testing the de-icing effect of ultrasonic vibration on iced plate elements. A self-developed device was used to measure the adhesive strength of ice on the plate surface. Based on the system, the adhesive strengths of ice under different excitation frequencies were measured and calculated. The experimental results validate that ultrasonic vibration has a significant de-icing effect. The adhesive strength of ice has decreased by 93%.
3. A blade segment with airfoil of NACA0018 was designed and manufactured. It has a hollow space at the leading edge, which is used to lay out PZT patches. The de-icing vibration mode and locations of PZT patches were decided by modal analysis. The vibration mode with alternative bending along the leading edge was selected as de-icing mode. The PZT patches were located at the locations with the highest deformation.
4. Based on the modal analysis of airfoil blade, a test coupon with PZT patches was manufactured, and the natural frequencies were obtained by an impedance analyzer. Then the experimental scheme and system were designed and built. In the anti-icing tests, it was validated that ultrasonic vibration has an anti-icing effect. With the increase in icing time, the anti-icing effect grew obviously. The frequency has an effect on the icing amount. In the present study, when the frequency was 25.604 kHz, the amount of ice was lowest.
5. Based on the anti-icing tests, a test of de-icing effect of ultrasonic vibration was conducted. A special, self-developed device was designed and manufactured to

measure the adhesive strength of ice for airfoil blade. The experimental research findings validated the de-icing effect of ultrasonic vibration. The best de-icing frequency scanned by the impedance analyzer was approximated to the one obtained from the modal analysis. It also validates that the selected de-icing vibration mode is suitable for airfoil blade.

## **Acknowledgements**

This work was supported by the Open Fund of the Key Laboratory of Wind Energy and Solar Energy Technology [grant number 2020ZD03]; National Natural Science Foundation of China (NSFC) [grant number 51976029].

## **Author details**

Jianlong Ma<sup>1</sup>, He Shen<sup>2</sup> and Wenfeng Guo<sup>1,2\*</sup>


1 Key Laboratory of Wind Energy and Solar Energy Technology (Inner Mongolia University of Technology), Ministry of Education, Hohhot, China

2 Northeast Agricultural University, College of Engineering, Harbin, China

\*Address all correspondence to: [guowenfengmailneu@163.com](mailto:guowenfengmailneu@163.com)

## **IntechOpen**

---

© 2023 The Author(s). Licensee IntechOpen. This chapter is distributed under the terms of the Creative Commons Attribution License (<http://creativecommons.org/licenses/by/3.0>), which permits unrestricted use, distribution, and reproduction in any medium, provided the original work is properly cited. 

## References

- [1] Dalili N, Edrissy A, Carriveau R. A review of surface engineering issues critical to wind turbine performance. *Renewable Energy*. 2009;13:428-438. DOI: 10.1016/j.rser.2007.11.009
- [2] Bose N. Icing on a small horizontal axis wind turbine part 1: Glaze ice profile. *Journal of Wind Engineering & Industrial Aerodynamics*. 1992;45:75-85. DOI: 10.1016/0167-6105(92)90006-V
- [3] Malhotra S. Design considerations for offshore wind turbine foundations in the United States. In: *Proceedings of the International Offshore and Polar Engineering Conference*; Osaka, Japan. California: International Society of Offshore and Polar Engineers (ISOPE); 2009
- [4] Thomas SK, Cassoni RP, Macarthur CD. Aircraft anti-icing and de-icing techniques and modeling. *Journal of Aircraft*. 1996;33:841-854. DOI: 10.2514/3.47027
- [5] Martin CA, Putt JC. Advanced pneumatic impulse ice protection system (PIIP) for aircraft. *Journal of Aircraft*. 1992;29:714-716. DOI: 10.2514/3.46227
- [6] Palacios JL, Smith EC, Gao H. Ultrasonic shear wave anti-icing system for helicopter rotor blades. In: *American Helicopter Society 62nd Annual Forum*; Phoenix, USA. Washington: American Helicopter Society International, Inc; 2006
- [7] Kulinich SA, Farzaneh M. Ice adhesion on super-hydrophobic surfaces. *Applied Surface Science*. 2009;255: 8153-8157. DOI: 10.1016/j.apsusc. 2009.05.033
- [8] Jose LP, Edward CS, Joseph LR. Investigation of an ultrasonic ice protection system for helicopter rotor blades. In: *The American Helicopter Society 64th Annual Forum*; Montreal, Canada. Washington: American Helicopter Society International, Inc; 2008
- [9] Palacios JL, Yun Z, Smith EC. Ultrasonic shear and lamb wave interface stress for helicopter rotor de-icing purposes. In: *47th AIAA/ASME/ASCE/AHS/ASC Structures, Structural Dynamics, and Materials Conference*; Rhode Island, USA. Washington: American Institute of Aeronautics and Astronautics; 2006
- [10] Palacios J, Smith E, Rose J. Instantaneous de-icing of freezer ice via ultrasonic actuation. *AIAA Journal*. 2011; 49:1158-1167. DOI: 10.2514/1.J050143





*Edited by Yan Li*

This book includes six chapters on wind turbine icing. For wind turbines operating in cold regions, icing often occurs on blade surfaces in winter. This ice accretion can change the aerodynamic shape of the blade airfoil, causing performance degradation and loss of power generation, even leading to operational accidents. This book focuses on the recent research progress on wind turbine icing. Chapters address such topics as the effect of icing conditions on the icing distribution characteristics of a blade airfoil for vertical-axis wind turbines, power loss estimation in wind turbines due to icing, wind turbine icing prediction methods, especially those using machine learning, the icing process of a single water droplet on a cold aluminum plate surface, the main theories of the icing adhesive mechanism, and theoretical and experimental studies on the ultrasonic de-icing method for wind turbine blades. This book is a valuable reference for researchers and engineers engaged in wind turbine icing and anti-icing research.

Published in London, UK  
© 2023 IntechOpen  
© tamara\_kulikova / iStock

**IntechOpen**

